FINITE ELEMENT ANALYSIS OF MIXED MODE FRACTURE

AND FAILURE IN IOSIPESCU SPECIMENS

Natarajan Sukumar
B. Tech., Metallurgical Engineering
Indian Institute of Technology
Bombay, India, 1989

A thesis submitted to the faculty of the
Oregon Graduate Institute of Science & Technology
in partial fulfillment of the
requirements for the degree
Master of Science
in
Materials Science and Engineering

October, 1992

The thesis "Finite Element Analysis of Mixed Mode Fracture and Failure in Iosipescu Specimens" by Natarajan Sukumar has been examined and approved by the following Examination Committee:

Maciej S. Kumosa, Thesis Research Advisor
Associate Professor
Dept. of Materials Science and Engineering

António M. Baptista
Assistant Professor
Dept. of Environmental Science and Engineering

Roshdy S. Barsoum
Solid Mechanics Program
Office of the Chief of Naval Research
Arlington, Virginia 22217

Lemmy L. Meekisho
Assistant Professor
Dept. of Materials Science and Engineering

ACKNOWLEDGEMENTS

Table of Contents

List of Figures

xi

List of Tables

ABSTRACT

FINITE ELEMENT ANALYSIS OF MIXED MODE FRACTURE AND FAILURE IN IOSIPESCU SPECIMENS

Natarajan Sukumar, M.S.

Oregon Graduate Institute of Science & Technology, 1992

Supervising Professor: Maciej S. Kumosa

The absence of an established mixed mode test method for the characterization of unidirectional composites has proven to be a stumbling block in the understanding of intralaminar failure mechanisms in these materials. In this thesis, a numerical study of the In-Plane Biaxial Iosipescu Test is carried out. The stress state in Iosipescu specimens is numerically investigated for notch angles from $60°$ to $150°$ under various mixed mode loading conditions. The materials modeled in the analysis are polyester resin (isotropic material), glass/polyester and carbon/epoxy unidirectional composites respectively. The singular stress fields at sharp notches in isotropic as well as orthotropic media are analyzed by the application of the Finite Element Iterative Method. In addition, the case of skew-symmetric splits in 0-deg unidirectional composite Iosipescu specimens is also studied, wherein fracture parameters like the mixed mode energy release rates and stress intensity factors are computed as a function of the crack length, loading angle, and orthotropy ratio.

A finite element analysis of the biaxial Iosipescu test method is performed, in which, Iosipescu specimens in either shear or a combination of shear, transverse tension

and compressive loadings are considered. Force-couple boundary conditions are used to analyze the stress state in the mid-section of the specimen. A complex stress distribution exists in isotropic as well as orthotropic Iosipescu specimens. The stresses at the notch root are singular in nature, and the stress distribution in the immediate vicinity of the notch root consists of a combination of normal and shear stresses.

The stress singularities at angular sharp notches in isotropic as well as orthotropic media are computed by the Finite Element Iterative Method. Three different loading conditions are considered in the numerical analysis: tension, shear, and a combination of tension and shear. In tension, the strong singularity λ_a is obtained, while under shear, convergence is to the weak singularity λ_b. When the loading is a combination of tension and shear, convergence is always to λ_a. The stress singularities λ_a and λ_b are found to be strongly dependent on the notch angle α, as well as on the elastic properties of the material. There exists a critical angle α_{cr} above which λ_b vanishes under shear loading conditions. For all notch angles $\alpha \geq \alpha_{cr}$, the stress field at the notch root is non-singular in nature. The values obtained for α_{cr} are of particular significance to practitioners involved in the analysis of the Iosipescu shear test for composite materials.

In 0-deg unidirectional composite Iosipescu specimens, a particular mode of fracture is the propagation of skew-symmetric splits along the fiber direction. The energy release rates G_I, G_{II}, and G_{total} are evaluated by three different numerical schemes: displacement extrapolation, J-integral, and the modified crack closure integral. Using beam theory analysis, an analytical solution for the energy release rates is also proposed. Axial splits in Iosipescu specimen propagate under mixed mode conditions, with G_I and G_{II} varying with the crack length a. For short cracks ($a \leq 4\text{mm}$), $G_I > G_{II}$, while for long cracks ($a \geq 10\text{mm}$), G_{II} is dominant. The merits and limitations of the numerical schemes

in the mixed mode fracture analysis of orthotropic composites are evaluated and discussed in detail.

CHAPTER 1

INTRODUCTION

The use of composite materials has increased significantly in the past two decades. The high specific modulus and high specific strengths of composites make them an attractive prospect for structural applications, both, in terms of weight reduction as well as greater load carrying capacity. With the increasing difficulty of improving the weight-efficiency of metal alloys and the development of high modulus, high strength fibers (i.e. carbon, aramid and boron) since the 1960's, there has been a dramatic increase in the application of fiber/polymer composites within the aerospace industry.

Fiber/polymer composites consist of continuous or short fibers embedded in either a thermoset (i.e. epoxy, polyester or phenolic resins), or thermoplastic (i.e. nylon, polysulphone and polyether-ether-ketone (PEEK)) matrix material. Continuous carbon fiber filaments have been commercially available since 1961, and are currently the predominant reinforcing material in fiber composites used for high stiffness/strength applications.

Carbon fiber composite structures are generally in the form of unidirectional plies laminated together at various orientations, or filament-wound configurations. These laminated fiber composites are highly susceptible to the presence of geometric discontinuities. The discontinuities may be deliberately introduced, such as design-cuts, or there may be inevitable defects produced during manufacturing or service. In particular, crack-like defects can be critical, as they can greatly reduce the stiffness and strength of composites, and can thus lead to catastrophic failure.

In laminated composites there are three principal failure modes (i.e. delaminations, intralaminar transverse cracking and fiber-breakage) which adversely affect the mechanical properties. Delaminations may be single or multiple planar cracks parallel to the laminate plies, and are often the result of some combination of mode I (tensile mode), mode II (in-plane shear mode) and mode III (anti-plane shear mode) fracture processes (Figure 1.1).

The ability to predict the mechanical properties and to understand the failure mechanisms in fiber-reinforced composites under mixed mode (shear dominated) loading conditions is important for the further development of fiber/polymer composite materials. Some of the important requirements for adequate predictions are reliable material data (elastic moduli, Poisson's ratios, and failure strengths), a suitable failure criterion, and an accurate component model. In most engineering applications, unidirectional composite laminae are subjected to biaxial or even triaxial type of loading. Hence, from an engineering design and application perspective, it is critical to characterize the mechanical behavior and response of these materials under mixed mode loading conditions.

In this thesis, a preliminary numerical investigation of the In-Plane Biaxial Iosipescu Test is conducted. Chapter 2 is a literature survey on the Iosipescu shear test as well as on the biaxial Iosipescu test method, along with details of mixed mode fracture phenomena in unidirectional composite Iosipescu specimens. In addition, relevant background about the Finite Element Iterative Method (FEIM), a numerical scheme for analyzing singular stress fields at points of discontinuities (cracks, sharp notches, interfaces etc.), is also presented. In Chapter 3, the numerical results are outlined: finite element analysis of uncracked as well as cracked isotropic and composite Iosipescu specimens, and stress singularity computations at sharp notches by the Finite Element Iterative

Method. The important results are discussed in Chapter 4, and the main conclusions obtained from this study are listed in Chapter 5. Chapter 6 looks at possible future research-work in regard to the biaxial Iosipescu test method. In Appendix A, the derivation of the load components used in the finite element analysis are outlined. In Appendix B, some of the most representative von Mises stress contours are presented, while in Appendix C, the expressions for the energy release rates in the Iosipescu specimen using beam theory analysis are listed. The test problem of an orthotropic strip with an edge crack under uniaxial tension is considered in Appendix D; the numerical results obtained for the stress intensity factors are presented. The energy release rate computations for coplanar cracks along the fiber direction in Iosipescu specimens are listed in Appendix E. In Appendix F, the hardware configuration along with the execution times involved in the numerical analyses are presented.
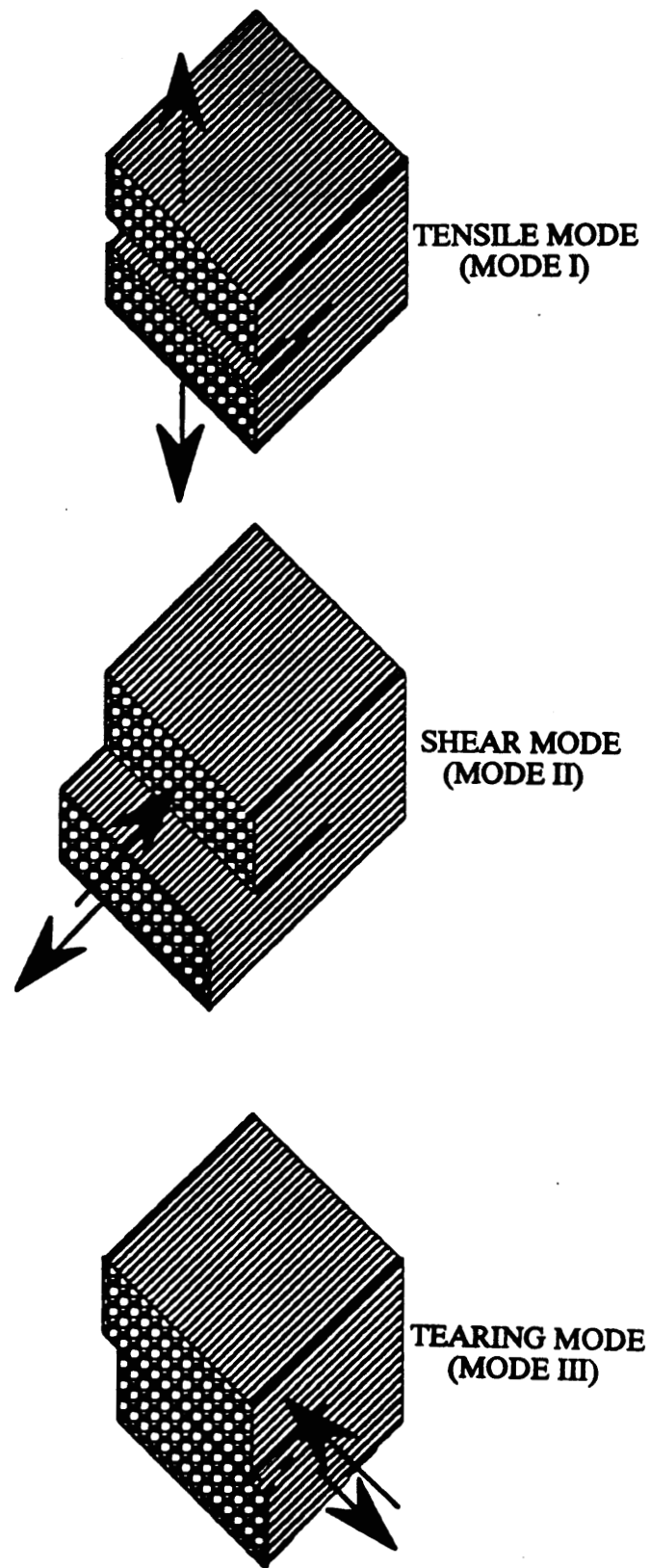
Figure 1.1 Independent modes of crack propagation in aligned fiber composites.[2]

CHAPTER 2

BACKGROUND

2.1. Intralaminar Shear Test Methods

To fully exploit the potential of composite materials in structural applications, it is necessary to have a complete and accurate description of their mechanical properties. The accurate determination of the in-plane shear properties (elastic modulus, ultimate shear strength and failure strain) and overall shear stress-strain behavior for advanced composite materials is much more difficult than for tensile or compressive properties. The problem stems from a difficulty in obtaining a pure shear stress state for a defined specimen geometry and loading condition. In highly anisotropic materials, coupling between the normal and shear deformation modes is common and a state of pure shear stress rarely occurs in composites. There have been numerous attempts to develop reliable test methods to determine the in-plane shear stress-strain response for advanced composite materials. The most commonly applied testing methods are: (1) two rail, (2) three rail, (3) cross-beam sandwich, (4) picture-frame panel, (5) thin-walled tube torsion, (6) 10 degree off-axis tensile, (7) ±45 degree off-axis tensile, (8) Iosipescu and (9) slotted-tensile. An evaluation of the above nine shear test methods by the decision analysis technique, [1] rated the Iosipescu and ±45° off-axis tensile shear tests as the best available for measuring in-plane shear properties. In an in-depth study on shear-dominated properties of unidirectional carbon fiber composites, Broughton[2] has presented a comprehensive review of the most important intralaminar testing methods.

2.1.1. Iosipescu's Method

The ideal test method is one that is relatively simple to conduct, employs small, easily fabricated specimens, and is capable of measuring both shear strength and shear modulus. Iosipescu[3] in 1967 proposed a method to determine the shear properties of metals. In this procedure, a state of pure shear stress is "achieved" at the mid-length of an isotropic double V-notched planar specimen, by the application of two counteracting force couples (Figure 2.1). A state of constant shear exists in the mid-section of the test specimen, with the induced moments canceling exactly at the mid-length, and thereby producing a pure shear stress state at this location. Figure 2.1 shows the force, shear and moment diagrams.

Originally, cylindrical test specimens were used, with a $90°$ circumferential V-notch cut completely around the mid-section. This specimen geometry transforms the parabolic shear stress distribution (associated with beams of constant cross-section) to a uniform shear distribution in the regions between the notches. The reduced area also promotes shear failure in this region. The two sides of the angular notches, which are the isostatics of the stress-free surfaces, must be inclined at an angle of $45°$. Hence, the included angle of the V-notch is $90°$. The applied force P divided by the net cross-sectional area A between the notch roots gives the nominal shear stress:

$$\bar{\tau} = P/A \tag{2.1}$$

Adams and Walrath[4,5] showed that the Iosipescu shear test method was suitable for determining in-plane and through-the-thickness shear properties of fiber composite materials (i.e. unidirectional carbon/fiber and sheet moulding compounds). Fiber composite shear tests use flat rectangular specimens with notches machined at the top and bot-

tom edges (Figure 2.2). Shear strain is measured at the center of the notch axis using two strain gauges oriented at $\pm 45°$ to the longitudinal axis of the test specimen.

Iosipescu[3] postulated that a uniform stress state resulted from the coincidence of the principal stress directions at $\pm 45°$ to the longitudinal axis with the $90°$ notch angle in the region of zero bending stress. It was argued that, since the sides of the notch are aligned with the plane of principal stress, the principal stresses would be zero at the notch root. Hence, there should be no shear stress concentrations or normal stresses present at the notch roots. However, numerous numerical and experimental studies have demonstrated this argument to be incorrect.

Finite element analysis shows that there is a complex stress distribution in the specimen, particularly in the vicinity of each notch root. Stress distributions (i.e. normal and shear) have been found to be dependent on the notch geometry (i.e. depth, angle and radius), orthotropy ratio, fiber orientation and loading boundary conditions. [2,5-18]

For specimens with fibers oriented parallel to the longitudinal axis (0-deg fiber orientation), the shear stress concentration factor K_t at the notch roots, defined as the ratio of the shear stress at the notch root to the shear stress at the specimen center, increases with increasing orthotropy ratio E_{11}/E_{22} (i.e. $K_t > 1$). [5-8] The shear stress increases rapidly in the vicinity of the notch roots to a maxima. In the case of specimens with fibers oriented transverse to the longitudinal axis (90-deg fiber orientation), K_t decreases with an increase in E_{11}/E_{22} (i.e. $K_t < 1$). The shear stress decreases rapidly to a minimum at the notch root. [5-8]

Walrath and Adams[5,9-12] have attempted to optimize the Iosipescu specimen geometry and Iosipescu shear test fixture. In a comprehensive investigation, the authors analyzed the stress distribution in the Iosipescu specimen as a function of the notch

geometry and orthotropy ratio. This work resulted in a re-designed University of Wyoming Iosipescu test specimen and fixture. [12] For orthotropic materials, it was demonstrated that an increase in notch angle or notch radius definitely reduces the shear stress concentration around the notch roots. The effect of notch depth on the stress concentration was minimal compared to the effects of notch angle and radius. [5] Barnes *et al.* [6] considered the effect of fiber orientation and orthotropy ratio on the measured shear properties of unidirectional glass/polyester. The apparent measured shear modulus was almost the same for 0-deg and 90-deg Iosipescu specimens, though the apparent intralaminar shear strength was strongly dependent on fiber orientation.

In an isotropic material, the influence of longitudinal stresses is minimal, but the transverse normal compressive stresses induced by the inner loading points intrude into the test section. It has been recommended that the inner loading points be moved away from the test region in order to reduce these compressive stresses. [5, 9-12, 14]

Kumosa and Hull[7] showed that there is a simple relationship between the shear stress concentration factor K_t at the notch roots, and the orthotropy ratio and fiber orientation:

$$K_t = A(E_{11}/E_{22})^{1/4} \tag{2.2}$$

where A is a numerical factor related to the stress concentration in an isotropic specimen.

Kumosa *et al.* [7,8] employed finite element analysis in order to determine the influence of elastic properties and boundary loading conditions on the stress distribution in the Iosipescu specimen. The loading of the finite element models was chosen to simulate the boundary conditions representative of:

(a) the loading originally proposed by Iosipescu with two force couples as illustrated in

Figure 2.3a (force-couple condition); and

(b) the displacement boundary conditions used by Adams and Walrath, [5,9] which assumes no rotations of the ends of the specimen in the loading fixture, as illustrated in Figure 2.3b (displacement condition).

A comparative study on isotropic and orthotropic Iosipescu specimens was performed to show that the force-couple conditions were representative of the actual experimental configurations. This involved comparing the isochromatic fringe patterns observed for the test specimens with numerically generated normalized von Mises contours[7,8] for both force-couple and displacement boundary conditions.

2.2. In-Plane Biaxial Iosipescu Test Method

In most engineering applications, unidirectional fiber composite laminae are subjected to biaxial and triaxial loads. Therefore, it is important to obtain the mechanical properties and failure criteria under multi-stress conditions. Currently, there are only a few tests available for the biaxial characterization of these materials. The tests which have been most frequently used for the intralaminar mixed mode failure (uncracked specimens) and fracture (specimens with pre-cracks) investigations are: the unidirectional off-axis tensile test, [19] filament wound thin-walled hoop wound tubes (with or without circumferential pre-cracks) under either torsion or combined tension and torsion loadings, [2,20,21] and the Arcan method. [22,23] In all of these tests, however, end-constraint effects, buckling, and bending moments introduce errors in the measured elastic properties.

As a result of the study conducted by Broughton, [2] a new In-Plane Biaxial Test Fixture, based on the Iosipescu shear test (Figure 2.1) and the Arcan in-plane stress method (Figure 2.4) was designed. [8] The biaxial fixture (marketed by Instron Corporation) is

shown in Figure 2.5. The fixture is capable of measuring mixed mode failure and fracture properties of isotropic and composite materials. In this study, it will be referred to as the biaxial Iosipescu test method. For biaxial in-plane stress tests, the compressive load P is applied at various angles ϕ to the normal, where ϕ is the angle between P_o and P (Figure 2.6).

2.3. Mixed Mode Fracture in Unidirectional Composites

Continuous fiber composites are heterogeneous materials with inherent micro-flaws (i.e. voids, matrix cracks, and fiber-interface debonds). The formation and propagation mechanisms of a crack are governed by the material microstructure and the stress state in the immediate vicinity of the crack front. In contrast to isotropic and homogeneous materials which often exhibit self-similar crack growth, fiber composites will often have cracks that do not propagate along the original crack orientation because of the local heterogeneity in front of the crack. In isotropic materials, the direction of crack growth is determined by the loading conditions: for example, in uniaxial tension, crack growth by mode I occurs on the plane normal to the maximum tensile stress. For a unidirectional composite material, the plane of fracture is determined both by the loading conditions, and the fiber orientation, and hence many different paths can be envisaged. Each crack growth direction has its own characteristic toughness and the lowest toughness is observed when the crack plane is parallel to the fiber direction. A crack lying on such a plane as a result of one type of loading conditions is likely to continue to grow in the plane even when the loading conditions are changed.

Since fiber composites exhibit multiple modes of fracture with no certainty of self-similar crack propagation, the principles of linear elastic fracture mechanics (LEFM)

may not necessarily apply to composite fracture. However, for unidirectional fiber composites in which cracks propagate along the fiber direction, the principles of LEFM are applicable. [24] In the case of cracks oriented along the fiber direction, the crack tip displacements can be separated into mode I, mode II, and mode III[25] (refer to Figure 1.1) where the stress intensity factors K_I, K_{II} and K_{III} govern the stress state at the crack tip.

There are few published results [7,13,15,26,27] concerned with the fracture mechanics aspects of the Iosipescu test. According to Swanson *et al.*, [15] failure of 0-deg specimens was initiated at the notch roots when two axial splits occurred parallel to the fiber direction. Walrath and Adams[5,11] assume that the actual failure is a result of longitudinal crack formation throughout the mid-section. This interpretation is based on the observation that specimens first crack at the notch roots, but then sustain load until the specimen fails catastrophically. Finite element analysis by Kumosa and co-workers[6-8] demonstrated that the nucleation and propagation of cracks in 0-deg and 90-deg specimens were controlled by different combinations of normal and shear stresses at the notch roots.

2.3.1. Basic Failure Modes in Composite Iosipescu Specimens

The modes of failure in the Iosipescu test are strongly dependent on the material anisotropy. Three basic failure modes are illustrated in Figure 2.7[7]. Failure mode T is characteristic of brittle isotropic materials and has been reported[14] for a vinyl-ester material. The cracks start at the roots of the notches and propagate on the plane of the principal tensile stress. Failure is catastrophic and results in complete fragmentation of the test specimen. Failure mode S occurs in unidirectional composite materials with fibers in B-type orientation. [6] Fracture is controlled primarily by shear; cracks start at the notch roots and propagate in an unstable mode parallel to the fibers. When unidirectional composite

material is tested with A-type orientation, failure mode M is observed. Cracks form parallel to the fibers and extend on one side of the notch tip, away from the loading points. Failure nucleation is caused by the shear stress concentration at the notch tip and crack growth in the plane of the principal tensile stress is prevented by the aligned fibers. The actual stresses associated with the initiation and propagation of cracks in mode M are complex although the shear stresses are dominant at the notch root. Similar mode of failure was observed by Kumosa and Hull[7] for a glass fiber-polyester resin unidirectional composite material.

2.4. Fracture Mechanics in Composite Materials

2.4.1. Constitutive Material Relations

The stress-strain relations in the principal material directions 1, 2 for an elastic anisotropic medium are given by[28]

$$
\begin{bmatrix} \varepsilon_{11} \\ \varepsilon_{22} \\ \gamma_{12} \end{bmatrix} = \begin{bmatrix} a_{11} & a_{12} & a_{16} \\ a_{12} & a_{22} & a_{26} \\ a_{16} & a_{26} & a_{66} \end{bmatrix} \begin{bmatrix} \sigma_{11} \\ \sigma_{12} \\ \tau_{12} \end{bmatrix} \tag{2.3}
$$

involving 6 independent material constants due to the symmetry of the compliance matrix. For plane anisotropy, this number reduces to four (E_{11}, E_{22}, v_{12}, G_{12}) with

$$
a_{11} = 1/E_{11}, \ a_{22} = 1/E_{22}, \ a_{12} = -v_{12}/E_{11} = -v_{21}/E_{22} \tag{2.4}
$$

$$
a_{66} = 1/G_{12}, \ a_{16} = a_{26} = 0
$$

and in the case of isotropic material only two independent constants are left (E and v or

G) with

$$a_{11} = a_{22} = 1/E, \ a_{12} = -v/E \hspace{3cm} (2.5)$$

$$a_{66} = 2(a_{11} - a_{12}) = 1/G, \ a_{16} = a_{26} = 0$$

for plane stress. [28]

2.4.2. Numerical Schemes for Extraction of Fracture Parameters

The testing as well as design of composites requires the ability to calculate fracture parameters such as the energy release rates and the stress intensity factors. There is considerable literature on numerical analysis aimed at this problem. Most use finite elements and then compute the energy release rate by various schemes based on nodal forces or displacements. The methods which are most frequently used in the numerical fracture investigation of isotropic as well as composite materials are: stiffness derivative, [29] virtual crack extension, [30,31] J-integral, [32] the displacement extrapolation method[33] (the stress intensities and then the energy release rates are calculated from the numerical displacements along the crack face), and the virtual crack closure technique. [34-38] Most of the above schemes are well established in linear elastic fracture mechanics of homogeneous isotropic materials; however, they may not be strictly applicable or extendible to typical fracture processes in composite materials. One of the exceptions is the very straight-forward and numerically highly effective crack closure integral technique or the virtual crack closure method. In the following sections, the principles and important equations in the displacement extrapolation method, J-integral formulation and virtual crack closure technique are outlined.

2.4.2.1. Displacement Extrapolation Method

The theory of linear elastic fracture mechanics provides two basic concepts which are the stress intensity factor (SIF) and the energy release rate G. The concept of the stress intensity factor is based on the analytical solutions for the stress or displacement field in the near vicinity of the crack tip. For a plane problem, the general form for these relations are given by:

$$\sigma_{ij} = \left[\frac{1}{2\pi r}\right]^{\frac{1}{2}} \left[K_I f_{ij}^I(\theta) + K_{II} f_{ij}^{II}(\theta) \right] \tag{2.6}$$

$$u_i = \frac{1}{2E} \left[\frac{r}{2\pi}\right]^{\frac{1}{2}} \left[K_I g_i^I(\theta) + K_{II} g_i^{II}(\theta) \right] \tag{2.7}$$

with $K_I = \sigma_y (\pi a)^{\frac{1}{2}}$ and $K_{II} = \tau_{xy} (\pi a)^{\frac{1}{2}}$; r and θ are polar coordinates at the crack tip. The SIFs K_I and K_{II}, associated with the basic fracture modes (refer to Figure 1.1), describe the intensities of the crack tip field in relation to the crack length a and the applied far field stresses σ_y^0 and τ_{xy}^0. In the displacement extrapolation scheme, the stress intensity factors K_I and K_{II} are evaluated by extrapolating (linear regression analysis) a displacement parameter, associated with the crack opening or sliding profile to the crack tip. [33] At the crack tip, quarter-point elements, [39,40] with the assumed square-root singularity, are used in the analysis. Quadratic isoparametric elements with the mid-side nodes placed at the quarter position (quarter-point elements) have been employed[39-44] for obtaining the stress intensity factors for elastic problems. The SIF extraction procedure was chosen by Kumosa and Hull[7] and Buchholz et al. [26] in their fracture analyses of the Iosipescu specimen. The relevant plane stress relations for isotropic materials are

given by

$$u_x = \frac{K_I}{2E}\left[\frac{r}{2\pi}\right]^{\frac{1}{2}}\left[(1+\nu)\left\{(2\kappa-1)\cos(\theta/2) - \cos(3\theta/2)\right\}\right] \qquad (2.8)$$

$$+ \frac{K_{II}}{2E}\left[\frac{r}{2\pi}\right]^{\frac{1}{2}}\left[(1+\nu)\left\{(2\kappa+3)\sin(\theta/2) + \sin(3\theta/2)\right\}\right]$$

$$u_y = \frac{K_I}{2E}\left[\frac{r}{2\pi}\right]^{\frac{1}{2}}\left[(1+\nu)\left\{(2\kappa+1)\sin(\theta/2) - \sin(3\theta/2)\right\}\right] \qquad (2.9)$$

$$+ \frac{K_{II}}{2E}\left[\frac{r}{2\pi}\right]^{\frac{1}{2}}\left[-(1+\nu)\left\{(2\kappa-3)\cos(\theta/2) + \cos(3\theta/2)\right\}\right]$$

where $\kappa = (3-\nu)/(1+\nu)$, and

$$u_x = K_I\left[\frac{2r}{\pi}\right]^{\frac{1}{2}} Re\left[\frac{1}{\mu_1 - \mu_2}\left\{\mu_1 p_2 (m_2)^{\frac{1}{2}} - \mu_2 p_1 (m_1)^{\frac{1}{2}}\right\}\right] \qquad (2.10a)$$

$$+ K_{II}\left[\frac{2r}{\pi}\right]^{\frac{1}{2}} Re\left[\frac{1}{\mu_1 - \mu_2}\left\{p_2 (m_2)^{\frac{1}{2}} - p_1 (m_1)^{\frac{1}{2}}\right\}\right]$$

$$u_y = K_I\left[\frac{2r}{\pi}\right]^{\frac{1}{2}} Re\left[\frac{1}{\mu_1 - \mu_2}\left\{\mu_1 q_2 (m_2)^{\frac{1}{2}} - \mu_2 q_1 (m_1)^{\frac{1}{2}}\right\}\right] \qquad (2.10b)$$

$$+ K_{II}\left[\frac{2r}{\pi}\right]^{\frac{1}{2}} Re\left[\frac{1}{\mu_1 - \mu_2}\left\{q_2 (m_2)^{\frac{1}{2}} - q_1 (m_1)^{\frac{1}{2}}\right\}\right]$$

with $m_1 = \cos(\theta) + \mu_1 \sin(\theta)$ and $m_2 = \cos(\theta) + \mu_2 \sin(\theta)$ for orthotropic material

behavior. Taking into account the presence of the quarter-point node in the displacement variation along the crack-tip element, Shih et al. [42] proposed the following formula:

$$u = 4u_B - u_C \qquad (2.11)$$

where u is evaluated from the points B and C (Figure 2.8). The displacement method - equation (2.11) is applicable to isotropic as well as orthotropic fracture analyses. The displacements u_x and u_y, as estimated from the above formula have to be substituted into (2.10) in which p_i and q_i are defined as $p_i = a_{11} \mu_i^2 + a_{12} - a_{16} \mu_i$, $q_i = a_{12} \mu_i + a_{22}/\mu_i - a_{26}$, i = 1, 2. μ_1 and μ_2 are the roots of the following equation, and they always occur in conjugate pairs as $\mu_1, \bar{\mu}_1, \mu_2, \bar{\mu}_2$: [25]

$$a_{11} \mu^4 - 2a_{16} \mu^3 + (2a_{12} + a_{66}) \mu^2 - 2a_{26} \mu + a_{22} = 0 \qquad (2.12)$$

where a_{ij} are anisotropic compliances which can be calculated from the elastic properties of the orthotropic material (refer Section 2.4.1).

Equations (2.10a) and (2.10b) express the relationship between the crack tip displacements and the stress intensity factors. The values of K_I and K_{II} obtained by the above method are considered to be good estimates of their true values in the case when the distance from the node to the crack tip is taken to be 1 or 2 percent of the total crack length. [45]

2.4.2.2. The J Contour Integral

The J contour integral has had great success as a fracture characterizing parameter for linear elastic as well as nonlinear elastic materials. By idealizing elastic-plastic deformation as nonlinear elastic, Rice[32] provided the basis for extending fracture mechanics

methodology well beyond the validity limits of LEFM.

Rice[32] presented a path-independent contour integral for the analysis of cracks. Consider an arbitrary counter-clockwise path (Γ) around the tip of a crack, as illustrated in Figure 2.9. The J-integral is given by:

$$J = \int_{\Gamma} \left[w\,dy - T_i \frac{\partial u_i}{\partial x}\,ds \right] \tag{2.13}$$

where w is the strain energy density, T_i are components of the traction vector, u_i are the displacement vector components, and ds is a length increment along a contour Γ. The strain energy density is defined as

$$w = \int_{0}^{\varepsilon_{ij}} \sigma_{ij}\,d\varepsilon_{ij} \tag{2.14}$$

where σ_{ij} and ε_{ij} are the stress and strain tensors, respectively. The components of the traction vector are given by

$$T_i = \sigma_{ij}\,n_j \tag{2.15}$$

where n_j are the components of the unit vector normal to Γ.

Rice [32] showed that the value of the J-integral is independent of the path of integral around the crack. Thus J is called a *path-independent* integral.

The numerical evaluation of the J-integral in 2-D linear elastic as well as nonlinear elastic problems is fairly straight-forward. The computation of the J-integral for 2-D problems is readily available in most general-purpose finite element programs; however, the J-integral in three-dimensions is much more complex, and has yet to reach the general-purpose program stage.

2.4.2.3. Virtual Crack Closure Method

Figure 2.10a shows a crack tip in an infinite isotropic plate subjected to remote mode I type loading. If the crack extends from a to $a + \delta a$, then, for infinitesimal values of δa, the crack opening displacements behind the new crack tip will be approximately the same as those behind the original crack tip. Hence, the work necessary to extend the crack from a to $a + \delta a$ is the same as that necessary to close the crack tip from $a + \delta a$ to a. Irwin[46] computed this, and thereafter the energy release rate associated with the crack extension from a to $a + \delta a$. Referring to Figure 2.10a and its notation for a pure mode I condition, Irwin's crack closure integrals are given by[46]

$$G_I(a) = \lim_{\delta a \to 0} \frac{1}{2\delta a} \int_{x=0}^{x=\delta a} \sigma_y(r=x, \theta=0, a) \, u_y(r=\delta a - x, \theta=\pi, a+\delta a) \, dx \qquad (2.16)$$

and

$$G_{II}(a) = \lim_{\delta a \to 0} \frac{1}{2\delta a} \int_{x=0}^{x=\delta a} \tau_{xy}(r=x, \theta=0, a) \, u_x(r=\delta a - x, \theta=\pi, a+\delta a) \, dx \qquad (2.17)$$

where (2.17) covers a superimposed or pure mode II crack tip condition. Substituting the analytical stress and displacement fields ((2.6) and (2.7)) into (2.16) and (2.17), the following relations have been obtained by Irwin[46]

$$G_I = \frac{K_I^2(a)}{\kappa E} \qquad (2.18)$$

$$G_{II} = \frac{K_{II}^2(a)}{\kappa E} \qquad (2.19)$$

where $\kappa = 1$ for plane stress and $\kappa = 1/(1 - v^2)$ for plane strain problems. Corresponding relations have been given by Sih, Paris and Irwin[25] for orthotropic materials with cracks in the principal material directions

$$G_I = K_I^2 \left[\frac{a_{11}a_{22}}{2} \right]^{\frac{1}{2}} \left[\left(\frac{a_{22}}{a_{11}} \right)^{\frac{1}{2}} + \frac{2a_{12} + a_{66}}{2a_{11}} \right]^{\frac{1}{2}} \qquad (2.20)$$

$$G_{II} = K_{II}^2 \left[\frac{a_{11}}{\sqrt{2}} \right] \left[\left(\frac{a_{22}}{a_{11}} \right)^{\frac{1}{2}} + \frac{2a_{12} + a_{66}}{2a_{11}} \right]^{\frac{1}{2}} \qquad (2.21)$$

Equations (2.16) and (2.17) represent the energy release rates $G_j(a)$, $j = I$, II on the basis of the work to be done in order to close the crack of length $a + \delta a$ by an amount δa. According to O'Brien, [35] equations (2.16) and (2.17) can be transformed into the following finite element representation

$$G_I(a) = \frac{1}{2\Delta a} \left[F_{y, i}(a) \Delta u_{y, j-2}(a + \Delta a) + F_{y, i+1}(a) \Delta u_{y, j-1}(a + \Delta a) \right] \qquad (2.22a)$$

$$G_{II}(a) = \frac{1}{2\Delta a} \left[F_{x, i}(a) \Delta u_{x, j-2}(a + \Delta a) + F_{x, i+1}(a) \Delta u_{x, j-1}(a + \Delta a) \right] \qquad (2.22b)$$

which holds for the discretization shown in Figure 2.10b. In the above equations, $F_{x/y, i}(a)$ and $F_{x/y, i+1}(a)$ denote the nodal point forces, while $\Delta u_{x/y, j-2}(a + \Delta a)$ and $\Delta u_{x/y, j-1}(a + \Delta a)$ are the relative nodal displacements. From (2.22a) and (2.22b), it can be seen that before obtaining one value of $G_j(a)$, $j = I$, II two finite element analyses have to be performed, with crack lengths a and $a + \Delta a$. Therefore, this scheme is also referred to as the 2C-method (two calculations). As opposed to (2.16) and (2.17), the 2C-method has been found to be applicable for finite crack extensions $\Delta a \gg 0$.

In order to avoid the disadvantage of the 2C-method, wherein two finite element calculations need to be carried out, Buchholz, [36] Krishnamurthy *et al.,* [37] and Raju, [38] have established the following formulae

$$G_I(a) = \frac{1}{t} \frac{1}{2\Delta a} \left[F_{y,\,i}(a)\Delta u_{y,\,i-2}(a) + F_{y,\,i+1}(a)\Delta u_{y,\,i-1}(a) \right] \qquad (2.23a)$$

$$G_{II}(a) = \frac{1}{t} \frac{1}{2\Delta a} \left[F_{x,\,i}(a)\Delta u_{x,\,i-2}(a) + F_{x,\,i+1}(a)\Delta u_{x,\,i-1}(a) \right] \qquad (2.23b)$$

in combination with the linear strain element discretization of Figure 2.10b. This is referred to as the improved modified crack closure integral method or 1C-method (one calculation). In contrast to the 2C-method given by (2.22), only one finite element analysis for the crack length *a* is required by the 1C-method. This decisive difference reduces the computational effort to one half. In case of mixed mode problems, the separated energy release rates $G_j(a)$, j = I, II are simultaneously obtained from (2.22a) and (2.22b) or (2.23a) and (2.23b).

As mentioned earlier, the virtual crack closure method is well-suited for numerical implementation. Since it is an energy-based method, the accuracy of the numerical values of the crack tip displacement and stress fields aren't critical, and hence neither mesh refinement nor the usage of singular elements (e.g., quarter-point elements, [39,40] with square-root singularity) at the crack-tip are essential in order to obtain accurate results. The modified crack closure integral schemes can be applied to 2-D and 3-D fracture analyses in isotropic as well as orthotropic materials. The added advantage of this method is that the total energy release rate G can be partitioned into its components: G_I for the opening mode I, and G_{II} for the sliding mode II.

2.4.3. Beam Theory Solutions

An important failure mode of composite laminates is the propagation of interlaminar and intralaminar defects. When the laminate is loaded, these defects can propagate to give a significant deterioration in performance. The energy release rate G has been widely used as a fracture parameter for the analysis of crack-like flaws in composite materials. The finite element method has been used to compute the G values from the nodal forces or displacements. The results, however, are rather complex to interpret, and hence there is a need for analytical solutions. Williams[47] has proposed a beam theory solution for the evaluation of the energy release rate G in cracked beams. The approach was applied to many popular mode I, mode II and mixed mode testing methods, wherein the mode partitions G_I and G_{II} were also estimated by the analysis. [47-49]

2.4.3.1. Total Energy Release Rate G

A delamination, such as one shown in Figure 2.11 is under consideration. This is a thin sheet of thickness 2h and width B containing a crack, a distance h_1 from one surface. The crack tip contour along with the rotations is shown in Figure 2.12. M_1 and M_2 are bending moments applied to the upper and lower sections respectively at the section AB. The crack is taken to be originally at O on AB and moves to O' on CD. The initial and final rotations on the upper and lower arms are shown in Figure 2.12. G may be defined for the contour as

$$G = \frac{1}{B}\left[\frac{dU_e}{da} - \frac{dU_s}{da}\right] \tag{2.24}$$

where U_e is the external work performed and U_s is the strain energy.

The total energy release rate G can be expressed as [47]

$$G = \frac{3(1+\nu)}{5\,B\,E\,A} \left[\frac{1}{\xi} \left[\frac{dM_1}{da} \right]^2 + \frac{1}{(1-\xi)} \left[\frac{dM_2}{da} \right]^2 - \left[\frac{dM_1}{da} + \frac{dM_2}{da} \right]^2 \right] \quad (2.25)$$

where ν is Poisson's ratio, E is Young's modulus parallel to the crack, A is the crack area, B is the thickness of the specimen, and ξ is a dimensionless quantity ($\xi = h_1/2h$).

2.4.3.2. Mode Partitioning

The critical values for G are different for the opening mode I and the sliding mode II. It is therefore necessary to separate, or partition, the total G mentioned in the previous section into the opening component G_I and the sliding, or shear component G_{II}. The mode partitions can be written as[47]

$$G_I = \frac{M_I^2}{B\,E\,I} \frac{(1+\beta)}{16(1-\xi)^3} \quad (2.26)$$

and

$$G_{II} = \frac{M_{II}^2}{B\,E\,I} \frac{3}{16} \frac{(1-\xi)}{\xi^2} (1+\beta) \quad (2.27)$$

where

$$\beta = \left[\frac{1-\xi}{\xi} \right]^3, \quad M_I = \frac{M_2 - \beta M_1}{1+\beta} \quad \text{and} \quad M_{II} = \frac{M_2 + M_1}{1+\beta}$$

2.5. Singular Stress Fields at Sharp Notches

Sharp notches or re-entrant corners are introduced in isotropic as well as composite structures, usually to facilitate fabrication. Within the limits of linear elastic analysis, the

stress field is unbounded at the tip of a sharp notch, with the strength of the *singularity* varying with the angle included in the notch. This was reported as early as 1952 by Williams.[50] The term *singularity* is used to denote cases where the elastic stresses become unbounded. If r is the distance from the notch tip, and λ is the stress singularity (or singular power), the stress field is of the order $r^{-\lambda}$ which becomes singular as r tends to zero. From a physical viewpoint, unbounded elastic fields are meaningless. Nevertheless, stress singularities cannot be ignored, as their presence indicates that new phenomenon (e.g. plasticity, fracture etc.) may occur, leading to localized damage in practical situations. The high stress concentration at these "singularity-dominated" regions make them likely sites for crack initiation, and therefore the potential source of ultimate failure. The ability to accurately evaluate the singularities and angular distributions around sharp notches is of great importance in design and failure analysis.

Williams[50] studied the stress singularities at the tip of a sharp notch in an isotropic plate under extension. The first eigenvalues for the entire range of notch angles were calculated. The boundary conditions on the radial edge were free-free, clamped-free, and clamped-clamped. Gross and Mendelson,[51] Lin and Tong,[52] and Portela *et al.*[53] have also investigated the stress singularity at V-notches. Gross and Mendelson[51] obtained numerical solutions for V-notched plates using the boundary collocation method, while Lin and Tong[52] applied hybrid finite elements to solve a similar problem. Portela *et al.*[53] evaluated the singularities in V-notched plates by coupling boundary element method to a singularity subtraction technique. The bimaterial wedge problem has been studied by analytical methods of solution.[54-56] In case of a homogeneous wedge, the eigen equation for a sharp notch with free-free edges reduces to that proposed by Williams.[50] Carpenter[57,58] has studied the eigenvector solutions and Rösel[59] has evaluated the eigen-

values corresponding to the eigen solution at a sharp notch. Fracture parameters like the stress intensity factor and stress concentration factors at sharp notches have been the subject of study by some researchers. [60,61]

The initial studies conducted on the Iosipescu specimen reveal that, in orthotropic materials, the stress field in the gage section is significantly non-uniform, and that there exists a high stress concentration at the notch root (refer Section 2.1.1). However, in spite of these observations, there have been very few studies so far to determine the exact nature of the stress field at the notch, due to the complex nature of the problem. The complexities involve, for example, the strong material anisotropy, complex specimen geometry, and unusual loading configuration. In the absence of critical information about the basic nature of the stresses at the notch root, researchers have resorted to various approximate methods, such as incorporating a radius at the notch root, so as to alleviate these difficulties. On the basis of anisotropic elasticity considerations (eigenfunction-expansion technique), Wang and Dasgupta[62] showed that above a critical angle, the stress field at the notch root is no longer singular and the shear stress, τ_{xy}, goes to zero there. In case of isotropic-Iosipescu specimens, they determined the critical notch angle to be 102.6°.

2.5.1. Stress Singularity at Sharp Notches

There are no analytical solutions for the singular power at sharp notches subjected to biaxial stress conditions in composite materials. Therefore, one has to seek solutions by numerical schemes. Within the framework of numerical methods, the finite element method has been widely applied to singularity problems. Of late, the Finite Element Iterative Method (FEIM)[63-71] has proven to be a powerful tool in the evaluation of

asymptotic singular fields for complex problems in fracture mechanics.

2.5.2. Analytical Solution for Homogeneous Isotropic Materials

The analytical solution for the stress singularity in a homogeneous isotropic plate under extension was proposed by Williams. [50] The analysis using the Airy stress function approach is summarized below.

Consider an isotropic material with a sharp V-notch of notch angle α (Figure 2.13). A polar coordinate system with $\theta = 0°$ along the -Y direction is assumed. The biharmonic equation in polar coordinates is

$$\nabla^4 \psi = 0 \qquad (2.28)$$

where

$$\nabla^2 = \frac{\partial^2}{\partial r^2} + \frac{1}{r}\frac{\partial}{\partial r} + \frac{1}{r^2}\frac{\partial^2}{\partial \theta^2} \quad \text{and} \quad \psi = \text{Airy stress function}$$

The stresses can be written in terms of the Airy stress function by the following relations:

$$\sigma_r = \frac{1}{r^2}\frac{\partial^2 \psi}{\partial \theta^2} + \frac{1}{r}\frac{\partial \psi}{\partial r} \qquad (2.29)$$

$$\sigma_\theta = \frac{\partial^2 \psi}{\partial r^2} \qquad (2.30)$$

$$\tau_{r\theta} = -\frac{1}{r}\frac{\partial^2 \psi}{\partial r \partial \theta} + \frac{1}{r^2}\frac{\partial \psi}{\partial \theta} \qquad (2.31)$$

The solution for the stress function ψ, for a sharp notch, takes the form[50]

$$\psi = r^{\lambda+1}[b_1\cos(\lambda+1)\theta + b_2\sin(\lambda+1)\theta + b_3\cos(\lambda-1)\theta + b_4\sin(\lambda-1)\theta] \quad (2.32)$$

For the free-free edges, the boundary conditions are

$$\sigma_\theta(r, -\pi + \alpha/2) = \sigma_\theta(r, \pi - \alpha/2) = \tau_{r\theta}(r, -\pi + \alpha/2) = \tau_{r\theta}(r, \pi - \alpha/2) = 0 \quad (2.33)$$

which leads to four linear algebraic homogeneous equations in b_i $(i = 1,2,3,4)$, namely

$$b_1(\lambda + 1)\sin[(\lambda + 1)(\pi - \alpha/2)] + b_3(\lambda - 1)\sin[(\lambda - 1)(\pi - \alpha/2)] = 0 \quad (2.34a)$$

$$b_1(\lambda + 1)\cos[(\lambda + 1)(\pi - \alpha/2)] + b_3(\lambda + 1)\cos[(\lambda - 1)(\pi - \alpha/2)] = 0 \quad (2.34b)$$

$$b_2(\lambda + 1)\cos[(\lambda + 1)(\pi - \alpha/2)] + b_4(\lambda - 1)\cos[(\lambda - 1)(\pi - \alpha/2)] = 0 \quad (2.34c)$$

$$b_2(\lambda + 1)\sin[(\lambda + 1)(\pi - \alpha/2)] + b_4(\lambda + 1)\sin[(\lambda - 1)(\pi - \alpha/2)] = 0 \quad (2.34d)$$

For a non-trivial solution, the determinant of (2.34) must vanish. Thus, the symmetric terms b_1, b_3 have a non-trivial solution[50]

$$\lambda \sin(\alpha) - \sin[\lambda(2\pi - \alpha)] = 0, \quad (2.35a)$$

while the anti-symmetric terms have a non-trivial solution [50]

$$\lambda \sin(\alpha) + \sin[\lambda(2\pi - \alpha)] = 0. \quad (2.35b)$$

The stresses in (2.29)–(2.31) vary as the second derivative of ψ, while the displacements are dependent on the first derivative of ψ. From the stress and displacement variations, it can be inferred that a value of $\mathrm{Re}\,\lambda$ such that $0 < \mathrm{Re}\,\lambda < 1$ will give unbounded stresses at the notch root. From (2.35a) and (2.35b), two real values, λ_1 and λ_2 are obtained corresponding to the symmetrical and anti-symmetrical terms respectively. The above two singular powers can be related to the strong singularity λ_a (symmetric term) by $\lambda_a = 1 - \lambda_1$, and to the weak singularity λ_b (anti-symmetric term) by $\lambda_b = 1 - \lambda_2$, where $0 \leq \lambda_b \leq \lambda_a \leq 0.5$. Williams [50] has only considered the strong singularity λ_a. This is well justified at points very close to the notch tip. Nevertheless, the relative

importance of the singular terms at moderate distances from the singular point depends on the value of the absolute intensities of the respective singular fields. [56]

2.5.3. The Finite Element Method

The finite element method has been used to analyze the stress distributions around points of discontinuities. [72-74] The stress distribution along a radial line from the singular point can be expressed as

$$\sigma_{ij} = A_1 \, r^{-\lambda} + O(r^{-\lambda+1}) \tag{2.36}$$

where r is the distance from the singularity, A_1 and λ are the strength and power of the singular field, and $O(r^{-\lambda+1})$ represents terms of the order $r^{-\lambda+1}$ and higher. For small distances r, the singular term dominates and (2.36) can be approximated by

$$\sigma_{ij} = A_1 \, r^{-\lambda} \tag{2.37}$$

Hence a $\log \sigma_{ij}$ versus $\log r$ plot would be a line with a slope of $-\lambda$ and a σ_{ij} intercept of A_1.

There are many drawbacks in evaluating the stress singularity by the above method. In a finite element analysis, the displacements around a crack or corner will comprise of the contribution of the structure as well as that of the discontinuity. Therefore, the true stress field in the vicinity of the crack-tip or corner is not realized. In cases where λ is not known *a priori*, ordinary eight-noded isoparametric elements at the crack- or notch-tip disturb the singular stress field, since the assumed linearity of stresses in the crack- or notch-tip element is erroneous. To obtain reasonable results, the region dominated by the singular field must be sufficiently large. Moreover, mesh refinement in the vicinity of the singular point is also required, which drastically increases the computation time and costs

involved in the analysis.

2.5.4. The Finite Element Iterative Method (FEIM)

The Finite Element Iterative Method (FEIM)[63-66] was originally developed for evaluating fields in elastic media. The method relies on the use of general purpose finite element programs in performing the iterations on the circular mesh shown in Figure 2.14b. The FEIM does not require the usage of quarter-point elements[39,40] at the crack-tip, for crack problems in homogeneous media (square-root singularity); nor are elements with embedded singularity[75] needed, in cases where the singularity is not known *a priori*. The method has been applied to many problems in fracture mechanics, which includes, bimaterial interface cracks of elastic and non-linear media, [64-68] and also to three-dimensional interface surface cracks. [70]

2.5.4.1. Basis of the FEIM Approach

The basis of the Finite Element Iterative Method has been discussed in detail by Barsoum. [63] The method is based on the use of a circular domain around the singularity for evaluating the eigenvalues of the transfer matrix of the inner and outer radii of the domain. [63,65] It is obtained from the overall stiffness matrix of the domain in Figure 2.14a. The equilibrium equations of the circular domain are

$$[K] \left\{ \begin{array}{c} u_0 \\ u_{Ri} \\ \overline{} \\ u_{Rs} \\ \overline{} \\ u_{Rb} \end{array} \right\} = \{ 0 \} \qquad (2.38)$$

where $[K]$ is the stiffness matrix of the circular domain, u_0 is the displacement of the origin of the singularity, and u_{Ri} is the displacement at any radius R_i except the inner radius R_s and the outer boundary radius R_b. By a process of elimination, the transfer matrix $[T]$ can be obtained. In FEIM, the imposed boundary displacements are obtained from the resulting displacements u_{Rs}.

Therefore, at the mth iteration we obtain[65]

$$\{ u_{Rs}^m \} = [T]\{ u_{Rb}^m \} \qquad (2.39a)$$

and

$$\{ u_{Rb}^{m+1} \} = \Lambda_m \{ u_{Rs}^m - u_0^m \} \qquad (2.39b)$$

where Λ_m is a scalar multiplier for normalizing the vector u_{Rs}. Using the Rayleigh quotient argument, [65] at convergence we obtain

$$\Lambda_m \to \Lambda \ \text{ as } m \to \infty \qquad (2.39c)$$

where Λ is the first dominant eigenvalue of the matrix $[T]$. It was shown[71] that Λ in general is given by

$$\Lambda = g(R_b / R_s) \qquad (2.40a)$$

where $g(r)/r$ is a general singular function. For the case of power singularity, then

$$\Lambda = (R_b / R_s)^{1-\lambda} \qquad (2.40b)$$

where $-\lambda$ is the power of the singular stress field. Therefore, for a self-adjoint case, the displacement u is given by

$$u = k r^{1-\lambda} f(\theta) \qquad (2.40c)$$

This form is referred to as a separable function.

For a non-symmetric matrix $[T]$, the system is non-self adjoint, and λ is complex. Therefore,

$$u = \text{Re}\,[\,(k_1 + ik_2)\,r^{(\{1-\lambda_{11}\}+i\lambda_{22})}\{\,f_1(\theta) + if_2(\theta)\,\}\,]\qquad(2.40d)$$

where $i = \sqrt{-1}$ and $\text{Re}\,[\,]$ designates the real part of the function. This form of the asymptotic field is termed a product form.

2.5.4.2 Evaluation of the Second Term of the Asymptotic Field

In order to describe the asymptotic field around a discontinuity, there may arise a need to evaluate the first as well as the second term of the asymptotic expansion. The transfer matrix $[T]$ has N eigenvalues $\Lambda_1, \ldots, \Lambda_N$. At any iteration m, the resulting solution can be expressed as a linear sum of the complete set of eigenfunctions $x_1, \ldots, x_N$:[70]

$$\{\,u_{Rb}^m\,\} = \Lambda_1^m\,\alpha_1\,x_1 + \overline{\Lambda}_1^m\,\overline{\alpha}_1\,\overline{x}_1 + \sum_3^N \Lambda_i^m\,\alpha_i\,x_i\,,\qquad(2.41a)$$

where x_1 and $\overline{x}_1$ are the dominant eigenvector and its conjugate. At convergence, as per the Rayleigh quotient, the whole field is dominated by the first term in the expansion, and hence (2.41a) reduces to

$$\{\,u_{Rb}^m\,\} = \Lambda_1^m\,\alpha_1\,x_1 + \overline{\Lambda}_1^m\,\overline{\alpha}_1\,\overline{x}_1\qquad(2.41b)$$

The FEIM will always converge to the first term of the expansion, which represents the dominant eigenvalue Λ_1 and eigenvector x_1 respectively. The second term in the expansion of the asymptotic field is of the same form as (2.40c) or (2.40d) depending on whether it is a real or complex singularity. For the case of real singularities (self adjoint case), the second term of the asymptotic field can be obtained by selecting the trial vectors to be orthogonal to x_1. Therefore, if the resulting vector from an iteration is V^m,

then the trial vector for the new iteration is given by[66]

$$U^{m+1} = V^m - (V^m \cdot x_1) x_1 \tag{2.42}$$

where U^{m+1} is to be used as the trial vector for the next iteration, which is always orthogonal to the first eigenvector x_1.

2.5.4.3 Convergence of the FEIM

The FEIM is similar to the power sweep method for finding the eigenvalues and eigen-functions. [76] The displacement field from the circular domain in Figure 2.14 can be written in the general form[68]

$$u = \sum_i g_i(r) f_i(\theta) + \sum_i h_i(r, \theta) , \tag{2.43a}$$

which contains regular as well as singular terms in r. When the asymptotic field dominates the domain surrounding the singularity, the leading singular term in the resulting singular displacements will either be

$$u \rightarrow g_1(r) f_1(\theta) , \tag{2.43b}$$

for which case the FEIM will converge, leading to a separable function or a product form ((2.40c) and (2.40d)), or, in the case of a non-separable field the second term will dominate, thus

$$u \rightarrow h_1(r, \theta) \tag{2.43c}$$

for a non-separable function. If the function in (2.43c) is a strong non-separable function, the FEIM will not converge, because of the circular domain of iteration. [68]
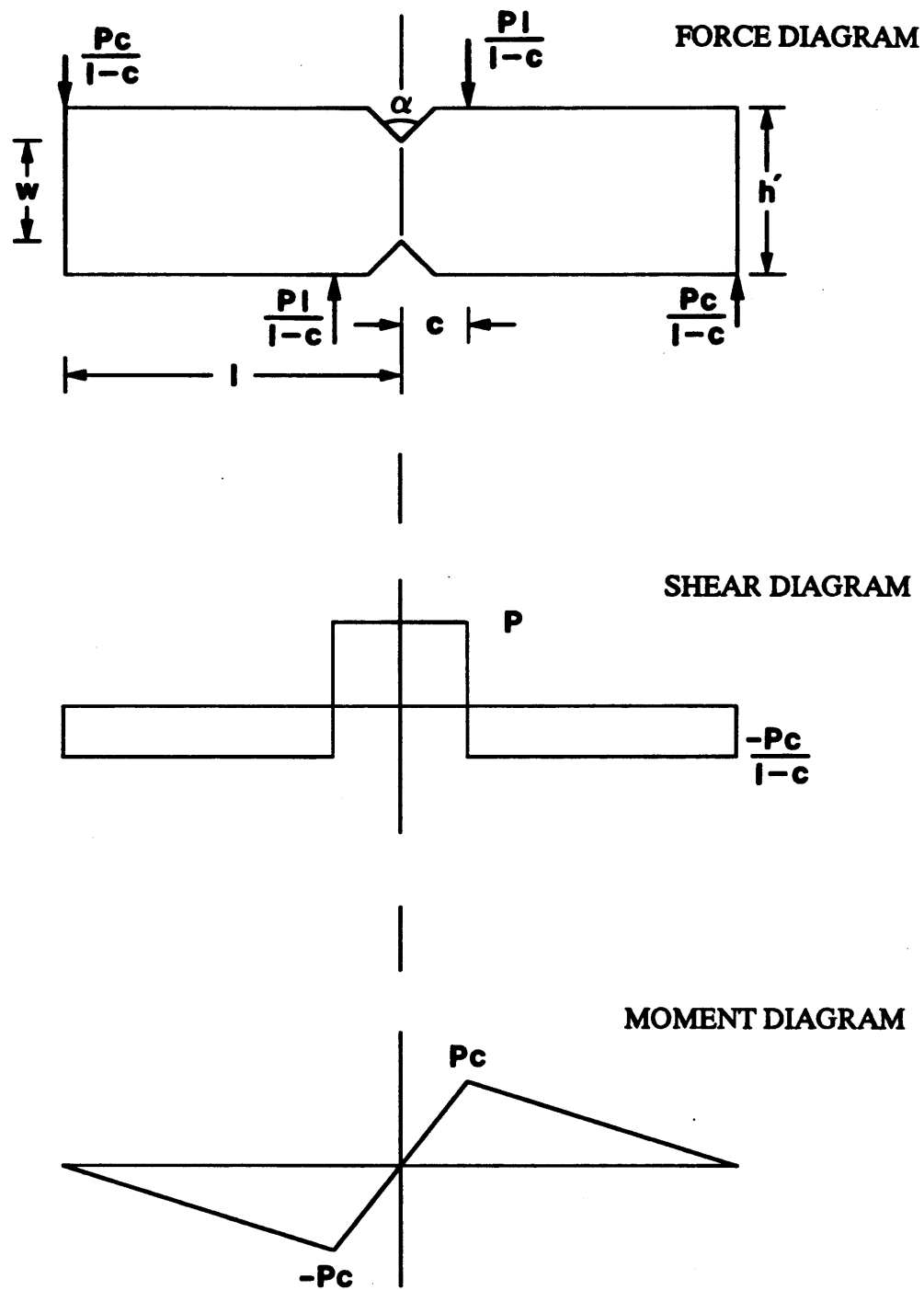
Figure 2.1 Force, shear and moment diagrams of the Iosipescu shear test.
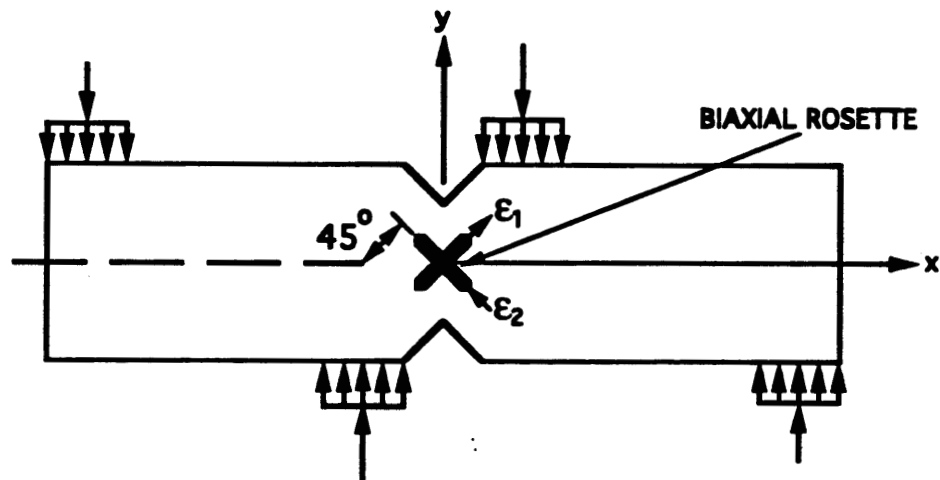
Figure 2.2 Iosipescu shear test loading configuration.

(a)

(b)
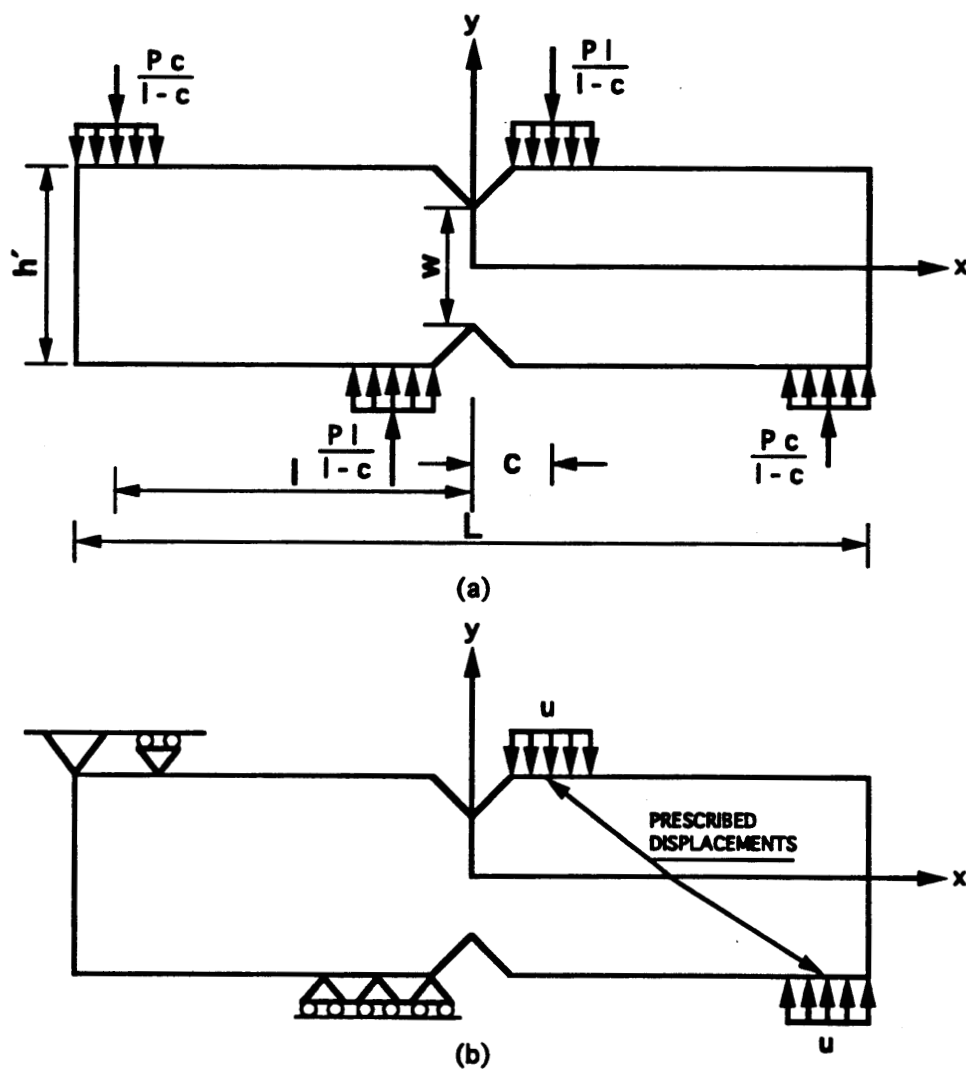
Figure 2.3 Boundary conditions for finite element calculations.[7]
(a) force-couple condition; and
(b) displacement condition.
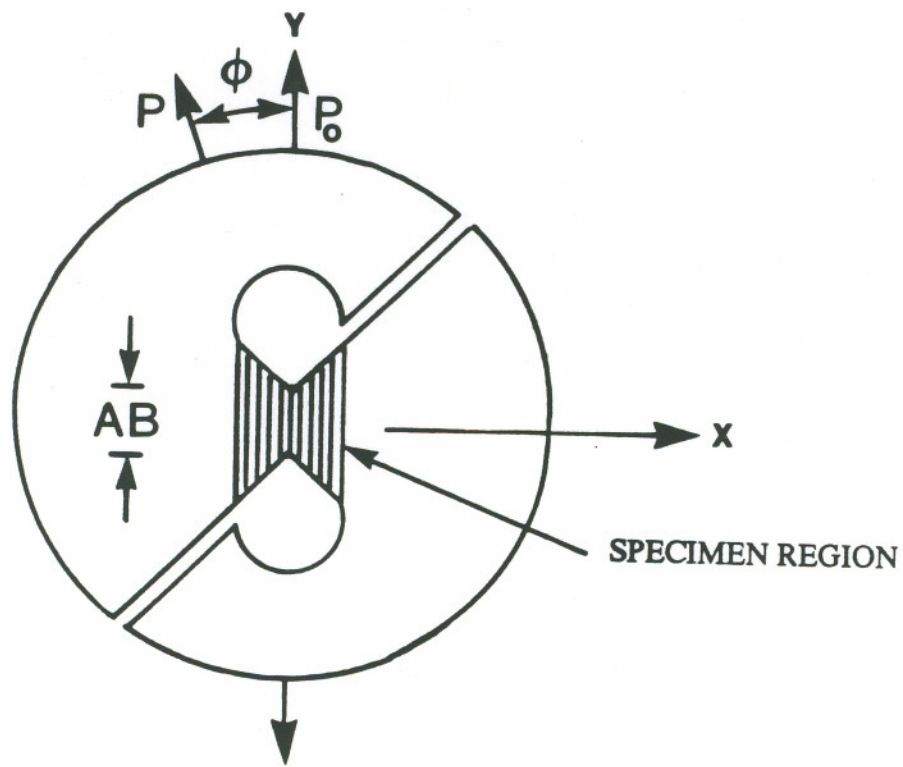
Figure 2.4 Arcan test method.[22]
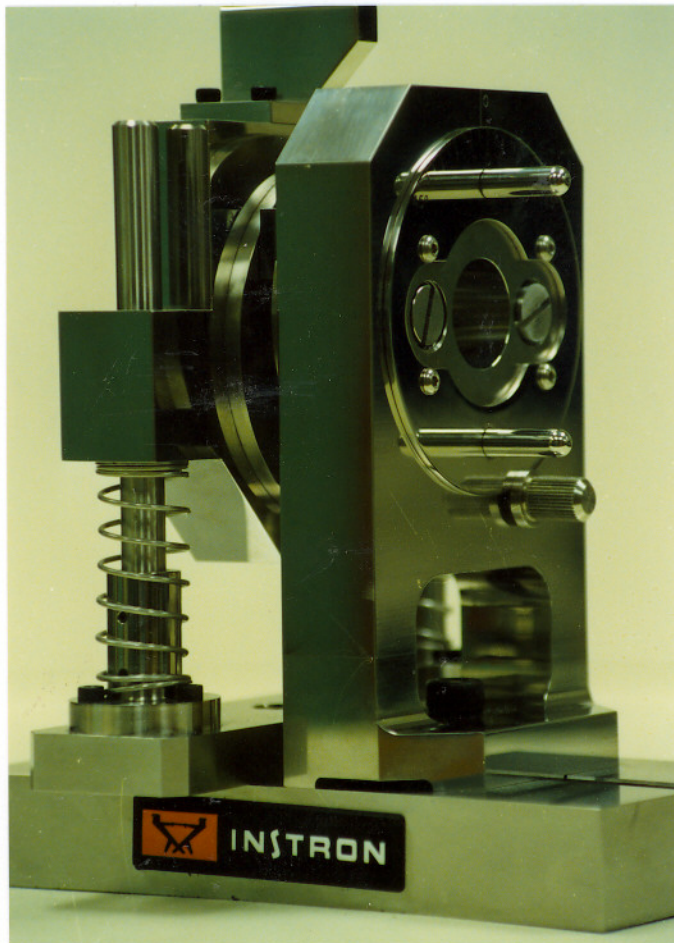
Figure 2.5 Biaxial Iosipescu fixture.
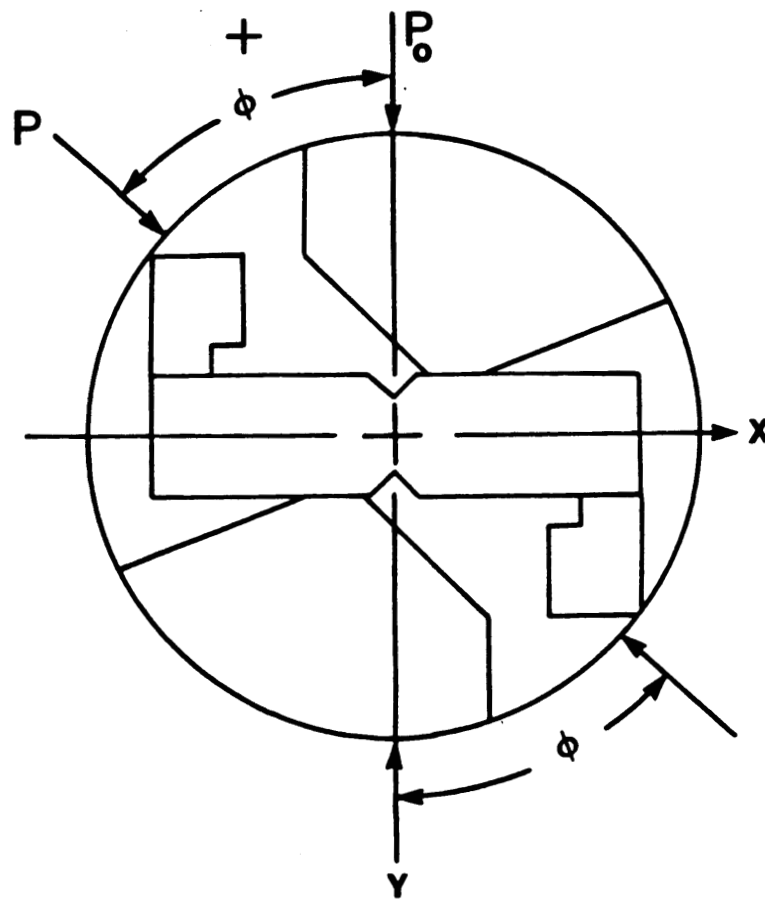
Figure 2.6 Load diagram for inducing an in-plane biaxial stress state.[2,8]

LOAD

MODE M

FIBERS (A)

MODE T

MODE S

FIBERS (B)

$\sigma_1 = -\sigma_2$

σ_2 τ σ_1
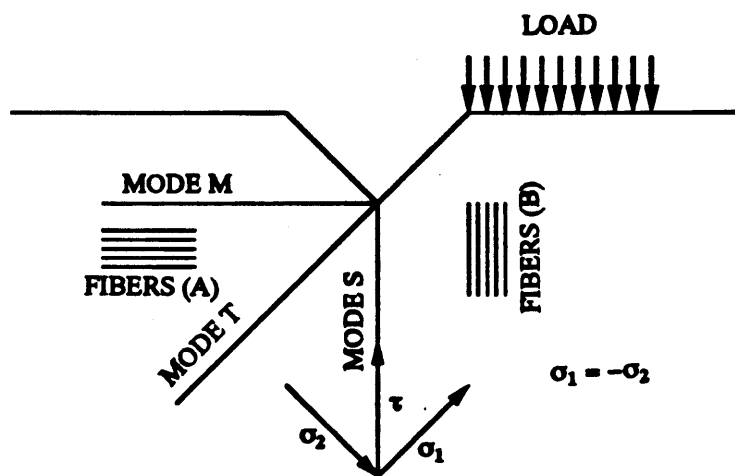
Figure 2.7 Schematic diagram of failure modes in the Iosipescu specimen.[7]

u_y
u_x
C B
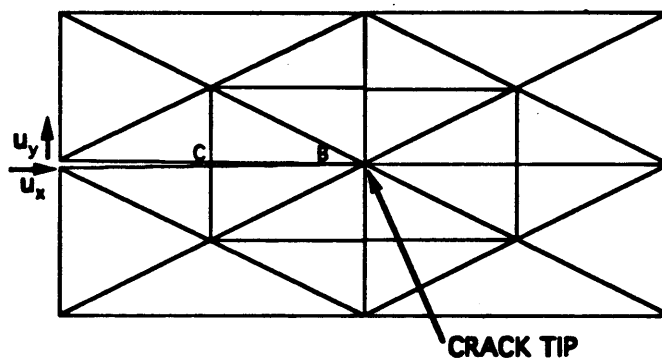
CRACK TIP

Figure 2.8 Details of crack tip (isoparametric quarter-point elements).

y

x

Γ

ds
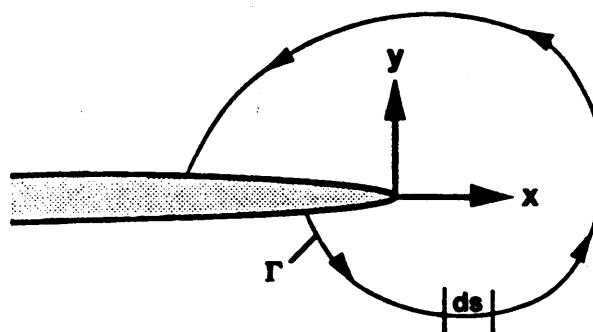
Figure 2.9 Arbitrary contour around the tip of a crack.
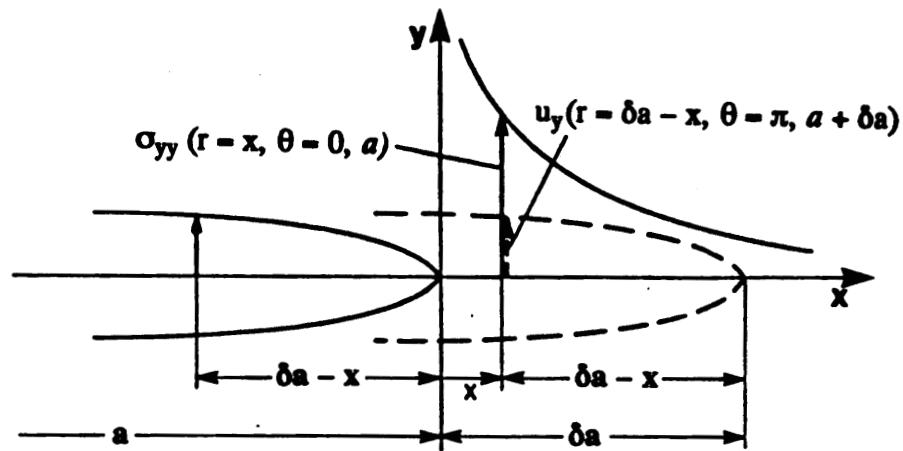
(a)
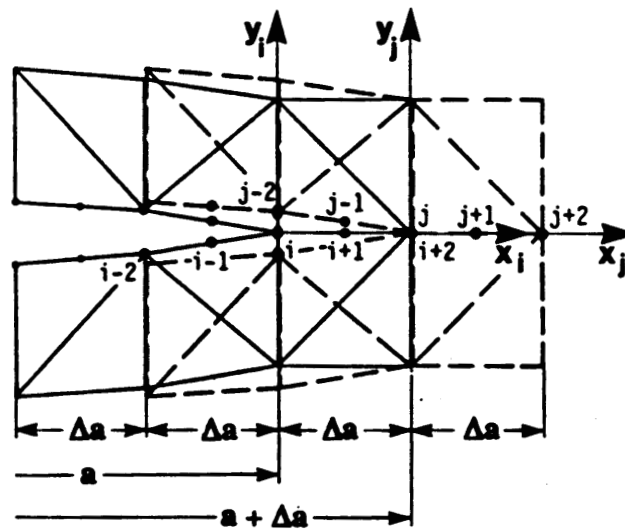
(b)

Figure 2.10 Crack closure integral method. (a) analytical; and (b) numerical (VCC).
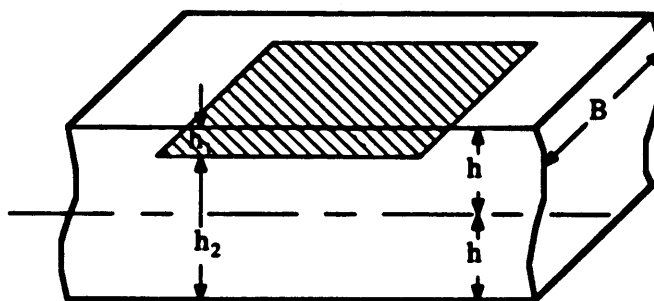
Figure 2.11 Delamination geometry.[47]
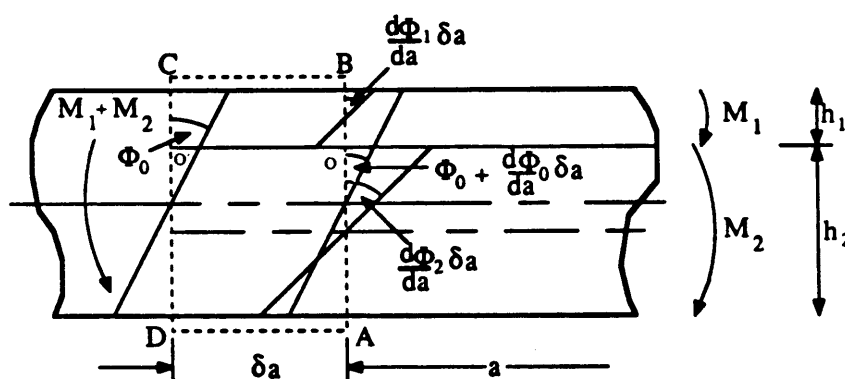
Figure 2.12 Crack tip contour with rotations.[47]
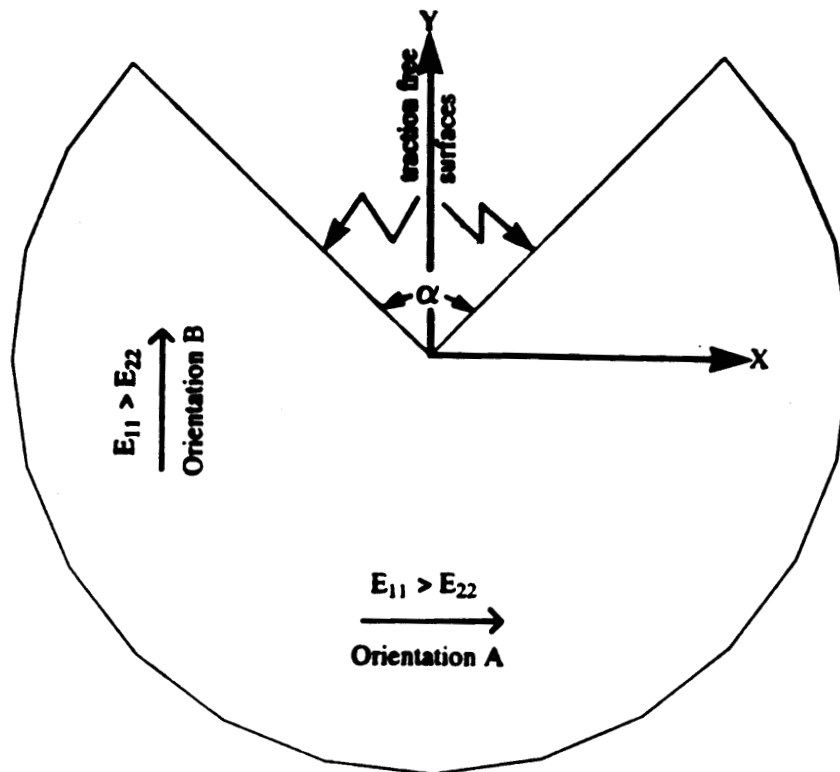
Figure 2.13 Notch geometry.

(a)
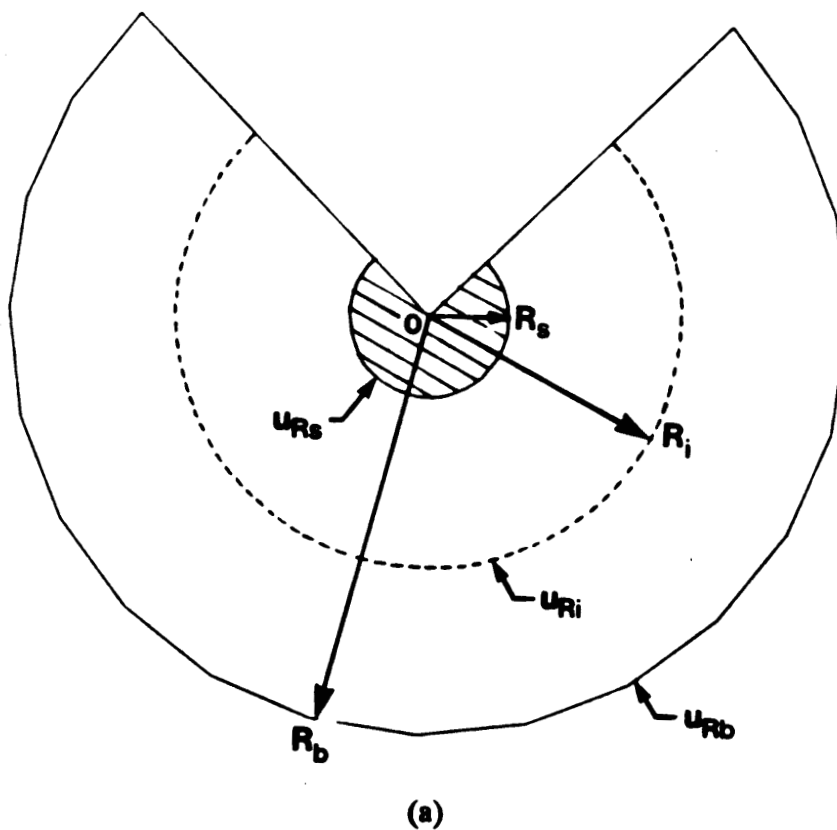
Figure 2.14 FEIM analysis for a sharp notch. (a) Domain of iteration; and (b) Mesh for
the Finite Element Iterative Method.

R_b

$\{u_i^o\}$ displacement distribution

R_s
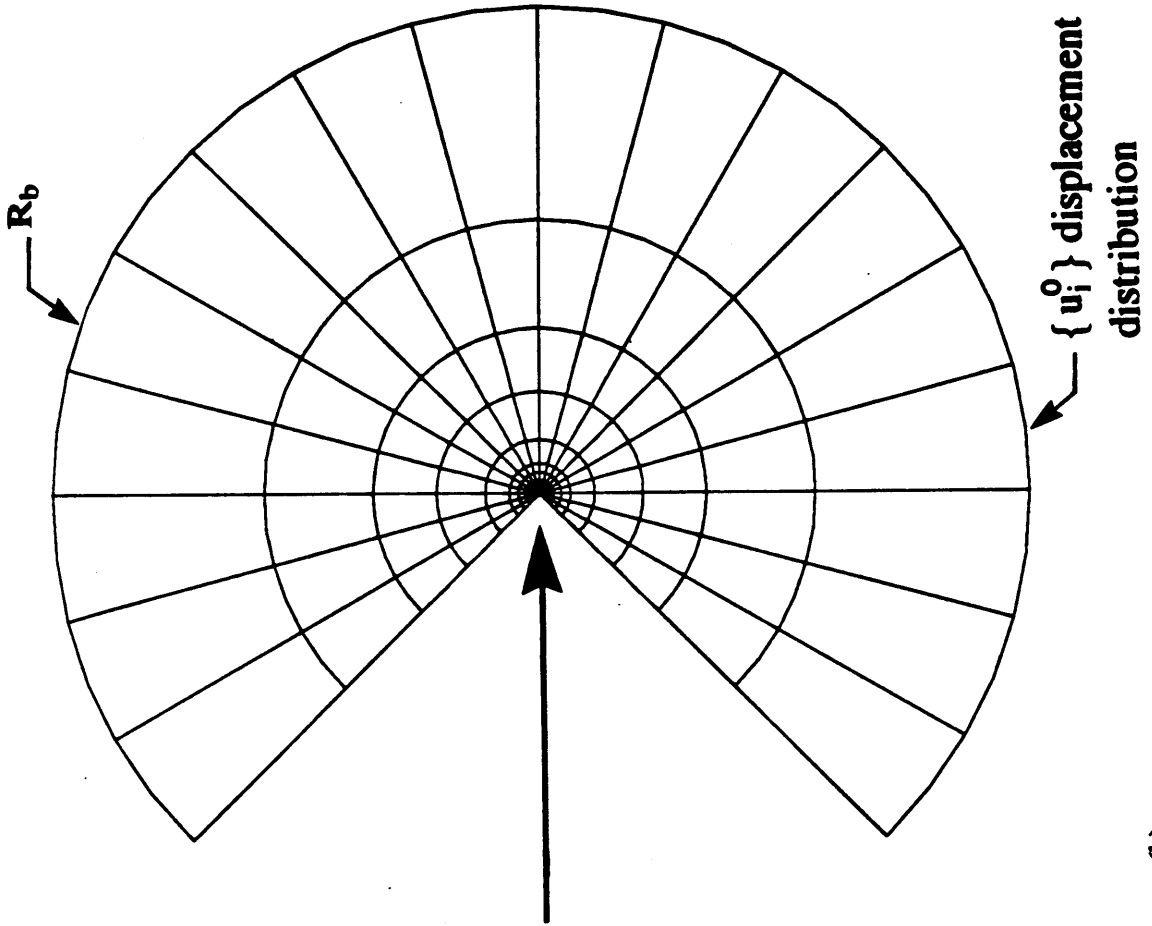
(b)
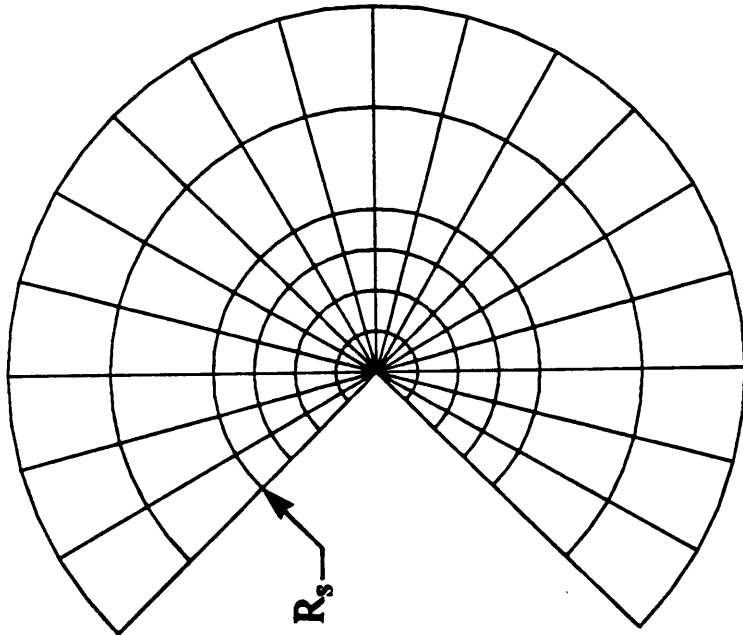
CHAPTER 3

NUMERICAL RESULTS

3.1. Finite Element Analysis of the Biaxial Iosipescu Test Method

3.1.1. Introduction

There is a strong need to accurately determine and thereafter analyze the stress state in the mid-section of the Iosipescu specimen. This is primarily due to two factors: firstly, the stress state at the center of the Iosipescu specimen is of importance in regard to the determination of the elastic properties of isotropic as well as composite materials; secondly, the stresses at the notch roots govern the initiation of the failure process. In this part of the study, a linear elastic finite element analysis under generalized plane stress was conducted to determine the macroscopic stress distribution in the Iosipescu specimen. The analysis was performed for notch angles α from $60°$ to $150°$, and for loading angles ϕ in the range $-45° \leq \phi \leq 38°$. The materials considered in the analysis were polyester resin (isotropic), glass/polyester and carbon/epoxy unidirectional composites respectively. Analytical solutions for the external load components as a function of the loading angle ϕ (see Appendix A) were firstly obtained. In order to verify the suitability of the model, von Mises stress contours from the finite element analysis were compared to isochromatic fringe patterns taken from the literature. [2,8] The stress state at the center of isotropic as well as composite specimens were evaluated under biaxial loading conditions. The nature of the stress concentration at the notch root was explored by studying the stress variation as a function of the notch-root element size. Finally, the

41

stress distribution in the notch-root region was analyzed for loading angles in the range $-45° \leq \phi \leq 30°$, in order to obtain an understanding of the failure mechanisms in the Iosipescu specimen for the specimen geometry, material orientation and loading conditions under consideration.

3.1.2. Finite Element Model

The finite element code ANSYS 4.4A[77] was used in the numerical computations, which were performed on an IBM RS/6000 workstation (see Appendix F for details). Eight-noded isoparametric quadrilateral and six-noded triangular elements with both isotropic and orthotropic elastic properties were used. The effect of orthotropy ratio was examined with E_{11}/E_{22} (ER) ranging from 1 to 14.2; the input elastic properties [8] are shown in Table 3.1. With reference to the material coordinates, the 1- and 2-axes will be defined as the in-plane coordinate axes. Material orientations A and B were used to model 0-deg and 90-deg unidirectional fiber composite materials respectively. In both orientations, the 1-direction corresponds to the fiber direction (Figure 3.1). From the photoelastic results of a study conducted by Broughton and co-workers, [2,8] it was concluded that the force-couple loading condition best approximates the actual experimental loading configuration. Therefore, in this study, the force-couple boundary conditions were used in the finite element model of the Iosipescu specimen.

The Iosipescu specimen dimensions are shown in Figure 3.2. The mesh for the Iosipescu specimen along with the force-couple boundary conditions are shown in Figure 3.3. The total compressive load P was arbitrarily taken as 115N. The entire specimen had to be modeled due to the asymmetric loading conditions. **The notch-root radius ρ was taken as zero in the finite element model.** The external load was applied to the

specimen with the force-couple condition in the form of a set of nodal forces which did the same amount of work on the structure as the two force couples. The finite element model shown in Figure 3.3 is for the particular case of $\alpha = 90°$ and $\phi = 0°$ (pure shear); it consists of 1964 isoparametric elements and 5281 nodes. The mesh was constructed in such a manner that the density of elements was highest around the notches and in the vicinity of the loading points.

3.1.3. Stress Distribution in Iosipescu Specimens

3.1.3.1. von Mises Stress Contours

In any modeling attempt, it is critical to firstly evaluate the suitability of the chosen boundary conditions. From a finite element analysis, the von Mises stress contours can be obtained, which when compared to isochromatic fringe patterns, give a good measure of the models predictions vis-à-vis the actual stress state realized in an experiment. In Figures 3.4 and 3.5, the von Mises stress contours are shown along with the isochromatic fringe patterns[2,8] for $\alpha = 90°$ and ER = 1, while in Figures 3.6 and 3.7 the same are presented for ER = 14.2 in orientations A and B respectively. The contour values indicated in Figures 3.4 − 3.7 correspond to those obtained for the von Mises stress contours. Some of the most representative stress contours for ER = 14.2 (orientations A and B) and $\alpha = 60°, 75°, 120°,$ and $150°$ are presented in Appendix B.

3.1.3.2. Stress Distribution at the Center

The stresses (σ_{ij}) at the center of the Iosipescu specimen were evaluated numerically as well as analytically, as a function of the loading angle ϕ, and orthotropy ratio ER. The

numerical values were obtained from the finite element calculations. The analytical formulae[2] are based on the assumption that there exists a one-to-one correspondence between the applied load and the stress state at the center; the stresses at the center are taken to be independent of the orthotropy ratio ER, and all notch-effects are neglected. As indicated by the above assumptions, the approach is very straight-forward. In other words, if the total compressive load P acts at an angle ϕ (see Figure A.1 in Appendix A), the stress state at the center can be written as:

$$\sigma_x^a = \sigma_y^a = \frac{P\sin\phi}{A} \tag{3.1a}$$

$$\tau_{xy}^a = \frac{P\cos\phi}{A} \tag{3.1b}$$

where A is the net cross-sectional area between the notches.

The analytical as well as numerically computed normal (σ_x and σ_y) and shear stresses (τ_{xy}) for ER = 1 are shown in Figure 3.8. In Figures 3.9 and 3.10, the same is presented for the highly orthotropic material (ER = 14.2) in orientations A and B respectively.

3.1.3.3. Stress Distribution at the Notch Roots

An in-depth study of the shear stress concentration at the notch roots was conducted. The shear stress distribution at the notch root was evaluated for isotropic and composite Iosipescu specimens with notch angles in the range $60° \leq \alpha \leq 150°$. In Figure 3.11, the variation of the normalized shear stress ($\tau_{xy}/\bar{\tau}$) between the center and the notch root is plotted as a function of α for ER = 1 and $\phi = 0°$. In Figures 3.12, the same is presented

for ER = 14.2 (orientation A) and $\phi = 0^\circ$.

Since the V-notches in the finite element model of the Iosipescu specimen were considered to be sharp ($\rho = 0$), one expects a stress singularity to exist at the notch root. In order to verify the above speculation, the shear stress distribution in the vicinity of the notch root was evaluated for different notch-root element sizes. In Figure 3.13, the shear stress plots are shown, while in Figure 3.14, the variation of K_t with notch-root element size is presented. K_t is defined as the ratio of the shear stress at the notch root (τ_{xy}^{nr}) to the shear stress at the specimen center (τ_{xy}^c). It can be seen from Figures 3.13 and 3.14 that the shear stress appears to be unbounded at the notch root, which indicates the presence of a singular stress field at the notch root. The stress singularity computations for angular sharp notches by the Finite Element Iterative Method will be presented in Section 3.3.

The shear stress concentration K_t at the notch root was evaluated for different orthotropy ratios ER, and varying notch-root element sizes. The data is presented in Table 3.2, and the variation of K_t versus ER on a logarithmic plot is shown in Figure 3.15 for three different notch-root element sizes. From Figure 3.15, it can be seen that the variation of $\log K_t$ versus $\log ER$ is linear, with increasing slopes for reducing notch-root element sizes.

The stress distribution (σ_{ij}) around the notches determines the initiation of the failure process at the notch root of Iosipescu specimens. The mode of failure is dependent on the material (isotropic or composites) as well as on the orientation of the fibers (0-deg or 90-deg) in case of unidirectional composites. A systematic finite element analysis of Iosipescu specimens with 90° notch angles was carried out. The analyses were done for isotropic (ER = 1) and composite specimens (ER = 14.2) under biaxial

loading conditions. In Figures 3.16 – 3.18, the results are shown for ER = 1. In Figures 3.19 – 3.21, the results are presented for ER = 14.2 (orientation A), while those in Figures 3.22 – 3.24 are for ER = 14.2 (orientation B). The results shown in Figures 3.16 – 3.24 were computed with a notch-root element size of 0.5mm.

3.2. Application of the Finite Element Iterative Method to Sharp Notches

The results obtained from Section 3.1.3.3 indicate the presence of a stress singularity at the notch root for angular sharp notches. In order to investigate the nature of the stress singularity (also known as the singular power), the Finite Element Iterative Method (FEIM) was applied to sharp notches in isotropic as well as orthotropic media. The method is formalized for it's application to sharp notches in the following section.

3.2.1. Iterative Approach for Plane Stress

The application of the Finite Element Iterative Method for a crack has been presented by Barsoum. [64] A similar approach is used in this analysis to evaluate singular stress fields at the tip of sharp notches. A generalized case of plane stress is assumed in the linear elastic numerical analysis.

(a) A fan-shaped mesh is constructed around the notch root (Figure 3.25). Only half-space is modeled for the notch in case of symmetry (mode I $\equiv$ tension) or anti-symmetry (mode II $\equiv$ shear) in the loading. Under mixed mode loading, full-space for the notch has to be modeled. The radii of the rings of elements which follow a (r^2) refinement are[63, 64]

$$(r_i/L) = 0, 0.25, 0.5, 0.75, 1.0, 1.625, (1.5)^2, (2)^2, (2.5)^2, (3)^2, (4)^2, (5.5)^2, (7)^2, (9)^2, (12)^2$$

where L is an arbitrary dimension.

(b) Since the singularity at the notch root is not known *a priori*, ordinary eight-noded isoparametric elements are used.

(c) The boundary conditions are: free along notch face, restrained from motion along X-direction (mode I loading) or Y-direction (mode II loading) along the line of symmetry.

(d) Using Figure 2.14a as a schematic, the iterative procedure is as follows.

   (i) Displacements $\{u_{Rb}^0\}$ are applied on the boundary at radius R_b. In this study, mode I, mode II, and mixed mode displacements are considered.

   (ii) Finite element analysis is performed and the displacements $\{u_{Rs}^0\}$ at radius R_s from the notch root are obtained.

   (iii) The notch root displacement $\{u_0^0\}$ is subtracted from $\{u_{Rs}^0\}$ and scaled by a factor Λ, to obtain the new boundary displacement $\{u_{Rb}^1\}$

$$\{u_{Rb}^1\} = \Lambda(\{u_{Rs}^0\} - \{u_0^0\}) \quad \text{where,} \quad \Lambda = (R_b/R_s)^{1-\lambda_0}$$

   (iv) The value of λ_0 as well as subsequent values (λ_i, i=1, 2, 3,..., n), where *i* refers to the *i*th iteration, are evaluated by a linearized least square curve-fit of displacements along a ray emanating from the notch root.

   (v) Steps (ii) to (iv) are repeated a number of times until convergence of λ is achieved.

   (vi) Convergence is said to have been attained when two consecutive values of λ are the same (i.e., $\lambda_i = \lambda_{i+1}$) up to the 4th significant digit after the decimal.

3.2.2 Stress Singularity Computations

The stress singularity at the notch root was evaluated for notch angles α in the range $0° \leq \alpha \leq 180°$, under three different loading conditions: mode I, mode II, and mixed mode. The effect of orthotropy ratio on the stress singularity at the notch root was examined with ER varying from 1 to 14.2 (Table 3.1): material orientations A and B were considered in the numerical analysis (see Figures 2.13 and 3.1).

In order to develop an FEIM program, the programming features of Ansys Parametric Design Language (APDL)[77] were utilized. A parametric model, comprising of a set of user-defined macros were developed for the implementation of the Finite Element Iterative Method at sharp notches.

3.2.2.1. Mode I Loading

A fan-shaped mesh was constructed around the notch tip (Figure 3.25a). Arbitrary initial mode I displacements were prescribed on the outer ring: $\{ u_x \} = 0.001\,mm$. All displacements are in the Cartesian coordinate system (Figure 2.13).

The FEIM approach was applied as outlined in Section 3.2.1. The numerical and analytical stress singularities are presented in Table 3.3, with precision up to the 4th significant digit after the decimal. It can be seen that the numerical and analytical results[50] for the isotropic case are in excellent agreement. The numerically evaluated stress singularities are within 0.5% of the analytical results. The stress singularities were evaluated by considering the u_x displacements along a particular ray emanating from the notch root to the outer ring. A linearized least square curve-fitting algorithm was used in the computations. The listed values of λ_a in Table 3.3 are the average values of λ_a

evaluated along three different rays emanating from the notch root. In addition, the variation of λ_s, as a function of notch angle α for different orthotropy ratios is shown in Figure 3.26a.

In all cases, convergence was attained in two or three iterations. Moreover, the converged values were the same along different rays. As an example, the convergence along three different rays, for the particular case of $\alpha = 90°$ and ER = 1 is shown in Figure 3.27a. In addition, a finite element representation of the deformed structure overlapped with the original structure at convergence is shown in Figure 3.28.

The stress singularity at the notch root was also studied under compression. The stress singularities in the above case were the same as those in tension (Table 3.3).

3.2.2.2. Mode II Loading

In this case, the fan-shaped mesh around the notch tip was identical to that used in tension (Figure 3.25a). Arbitrary initial mode II displacements were prescribed on the outer ring: $\{ u_y \} = -0.001$ mm. All displacements are in the Cartesian coordinate system (Figure 2.13). After imposing the initial boundary displacements, the FEIM approach was applied.

The stress singularities were evaluated by considering the u_y displacements along a particular ray emanating from the notch root to the outer ring. A linearized least square curve-fitting algorithm was used in the computations. The singularities under mode II loading are listed in Table 3.4, with precision up to the 4th significant digit after the decimal. Based on the results of individual iterations, convergence was not observed in three cases ($\alpha = 105°$, $120°$, $150°$) for ER = 14.2 (A). The listed values in Table 3.4, for the above cases, are intermediate values during the analysis, where convergence is

'expected'. But for the above three anomalies, convergence was observed for all the other cases. The listed values of the stress singularities in Table 3.4 are the average values evaluated along three different rays emanating from the notch root. The variation of the singularity under mode II loading, as a function of the notch angle α for different orthotropy ratios is shown in Figure 3.26b.

The number of iterations for convergence under mode II loading was much higher than in the case of mode I loading, and was dependent on the notch angle α and the orthotropy ratio ER. The converged values were the same along different rays. In Figure 3.27b, the convergence along three rays is shown, for the particular case of $\alpha = 90^\circ$ and ER = 1. In addition, a finite element representation of the deformed structure overlapped with the original structure at convergence is presented in Figure 3.29.

3.2.2.3. Mixed Mode Loading

A full fan-shaped mesh around the notch tip was considered, due to the non-symmetrical loading conditions (Figure 3.25b). The stress singularity at the notch root was studied as a function of the loading angle ϕ, for the notch angle $\alpha = 90^\circ$. The loading angle ϕ was used as a measure of the tension to shear ratio in the loading. The elastic properties considered in this part of the analysis were those for ER = 1 and 14.20. The loading angle ϕ was varied from 45° (tension $\equiv$ shear) to 89.9° (almost pure shear). The initial displacement distribution (in mm) prescribed on the right half of the outer ring was: $\{u_x\} = 0.01 \cos\phi$, $\{u_y\} = -0.01 \sin\phi$, while that on the left half of the outer ring was: $\{u_x\} = -0.01 \cos\phi$, $\{u_y\} = 0.01 \sin\phi$. All displacements are in the Cartesian coordinate system (Figure 2.13). The FEIM approach was subsequently applied to the fan-shaped mesh. The stress singularities were evaluated by considering the u_x displacements along

a particular ray emanating from the notch root to the outer ring. A linearized least square curve-fitting algorithm was used in the computations. The evaluated singularities under mixed mode loading are listed in Table 3.5, with precision up to the 4th significant digit after the decimal. The listed values of λ in Table 3.5 are the average values evaluated along three different rays emanating from the notch root.

The number of iterations for convergence was strongly dependent on the loading angle ϕ, but did not significantly vary with the orthotropy ratio ER. The number of iterations (along one particular ray) increases from 5 for $\phi = 45°$ to 8 for $\phi = 89.9°$ (Figure 3.30). The stress singularity values are listed in Table 3.6, and a finite element representation of the deformed structure overlapped with the original structure for $\phi = 89.9°$ is shown in Figure 3.31.

3.2.3. Interpolation Formulas

In Section 3.2.2, the stress singularities λ_a and λ_b were computed as a function of the notch angle α and orthotropy ratio ER. Simple interpolation formulas which could describe the variation of λ_a and λ_b with α and ER are of particular significance to a practicing engineer. By using them, one can estimate the singularities without having to rely on time-consuming and cost-intensive numerical analysis. It is with this in mind that an attempt was made to propose interpolation formulae for λ_a and λ_b.

The dependency of λ_a and λ_b on α and ER is complex in nature; hence, a straightforward polynomial interpolation will not yield accurate results. Considering the trends observed in the results obtained in Section 3.2.2, power products of $\log(ER)$ and $\cos(\alpha/2)$ were chosen as basis functions. A least square fitting algorithm in the sense of the norm was developed (code was written in Fortran 77) to estimate the coefficients in the

assumed expansion of λ_a and λ_b.

3.2.3.1. Strong Singularity λ_a

The data set for the interpolation of λ_a was taken from Table 3.3, wherein $0° \leq \alpha \leq 180°$ and ER = 1/14.2, 1/3.45, 1, 3.45, and 14.2. The orthotropy ratios 1/14.2 and 1/3.45 represent the values in orientation B (Figure 2.13). The interpolation formula obtained for λ_a can be written as:

$$
\begin{aligned}
\lambda_a = \; & 1.6580739 \cos(\alpha/2) + 0.11315084 \cos(\alpha/2) \log(ER) \\
& - 2.6567626 \cos^2(\alpha/2) - 0.1212517 \cos^2(\alpha/2) \log(ER) \quad\quad (3.2) \\
& + 2.2679832 \cos^3(\alpha/2) - 0.77275658 \cos^4(\alpha/2)
\end{aligned}
$$

where α is in **radians**.

The values obtained for λ_a from the above interpolation formula were found to match well with the numerical results presented for λ_a in Table 3.3. As an example, in Figures 3.32a and 3.32b, the predictions by the interpolated formula - equation (3.2) are shown along with the analytical[50] and numerically computed singularities for ER = 1 and ER = 14.2 (A). The values for λ_a obtained from the interpolation can be expected to have errors of 10% or less. For values of α in the vicinity of $0°$ or those in the neighborhood of $180°$, one may obtain $\lambda_a > 0.5$ or $\lambda_a < 0$ respectively. In the former case, $\lambda_a = 0.5$ must be assumed, while in the latter case, $\lambda_a = 0$ must be taken. Equation (3.2) may breakdown for very low or very high values of ER, which lie far away from the lower and upper bounds of ER considered in this study.

3.2.3.2. Weak Singularity λ_b

The data set for the interpolation of λ_b was taken from Table 3.4. As opposed to the case of λ_a, above a certain value of α, λ_b vanishes, which can be seen from Table 3.4. Hence, firstly a regression analysis of α_{icr} versus $\log ER$ was performed to determine an expression for the critical angle α_{icr} as a function of ER. An R square value of 0.99869 was considered to be acceptable for a cubic interpolation. Then, on the remaining data (non-zero values of λ_b), a similar analysis to that performed in tension was carried out. The interpolation formula obtained for λ_b can be written as:

$$
\lambda_b =
\begin{cases}
\begin{aligned}
& -1.6241827 \cos(\alpha/2) + 0.3206903 \cos(\alpha/2) \log(ER) \\
& +5.0457487 \cos^2(\alpha/2) - 0.3120525 \cos^2(\alpha/2) \log(ER) \\
& -5.6477222 \cos^3(\alpha/2) + 2.7200093 \cos^4(\alpha/2) \quad \text{for } \alpha < \alpha_{icr}
\end{aligned} \\
\\
0.0 \hspace{7cm} \text{for } \alpha \geq \alpha_{icr}
\end{cases}
\tag{3.3a}
$$

where α is in **radians** and α_{icr} is given by

$$
\begin{aligned}
\alpha_{icr} = {} & 1.7961 + 0.201580 \log(ER) + 0.023773 \, [\log(ER)]^2 \\
& + 0.006406 \, [\log(ER)]^3
\end{aligned}
\tag{3.3b}
$$

where α_{icr} is in **radians** and ER > 1 in orientation A, while ER < 1 in orientation B.

In Figures 3.32a and 3.32b, the predictions by the interpolated formula - equation (3.3) are shown along with the analytical[50] and numerically computed singularities for ER = 1 and ER = 14.2 (A) respectively. The accuracy and limitations of the above interpolation formula for λ_b are the same as those that were discussed for the case of λ_a (see Section 3.2.3.1).

3.3. Mixed Mode Fracture in Iosipescu Specimens

3.3.1. Introduction

The design and development of composite materials relies on the fundamental knowledge of the failure processes in these advanced materials. From an engineering perspective, the knowledge of single crack-tip fracture parameters like the stress intensity factor or the energy release rate is required to predict the strength and life of cracked structures. The above information, in conjunction with experimentally determined critical values (K_{Ic} or G_{Ic}) and crack growth rates for structural materials make such predictions possible. Since exact solutions of the elasticity problem formulated for cracked composite structures are very difficult or nearly impossible to obtain, recourse is taken to numerical methods such as the finite element method to obtain the fracture parameters. In this part of the study, a finite element analysis of coplanar cracks along the fiber direction in Iosipescu specimens ($\alpha = 90°$) was carried out. Mixed mode crack propagation was studied for loading angles ϕ in the range $-45° \leq \phi \leq 30°$, and for crack lengths a from 1mm to 13mm. Stress intensity factors (K_I, K_{II}) and energy release rates (G_I, G_{II}, G_{total}) were evaluated as a function of the crack length a and loading angle ϕ. Beam theory solutions for the energy release rates in Iosipescu specimens were also proposed and subsequently compared to the results obtained from the finite element computations.

3.3.2. Finite Element Model

The finite element mesh of the Iosipescu specimen with two skew-symmetric cracks ($a = 10$mm) is shown in Figure 3.33; the mesh consists of 1426 elements and 4339 nodes. Force-couple boundary conditions for $\phi = 0°$ are also illustrated in Figure 3.33. The total

compressive load P was assumed to be 1kN. A fan-shaped mesh was constructed around both the crack tips; the maximum separation between the crack faces was taken as 1% of the crack length a. There are 12 elements in the circumferential direction around the crack-tip. In Figure 3.34, the inner mesh along with the crack-tip elements (non-singular elements) are shown. Ordinary six-noded triangular elements were used at the crack tip for the energy release rate computations by the J-integral and the virtual crack closure schemes (2C- and 1C-methods); for the displacement extrapolation method, quarter-point elements[39,40], with the mid-side nodes moved to the quarter-position were used. The crack-tip element size was 0.025mm for all crack lengths. The fan-shaped mesh around the crack tip facilitated easier mesh refinement without unduly increasing the total number of elements; in addition, the circular nodal paths were well-suited for the J-integral calculations.

The orthotropy ratios considered were those for ER = 1 (isotropic) and ER = 14.2 (A-type); the elastic properties are listed in Table 3.1. **The isotropic case has physically no meaning since such cracks cannot form in isotropic materials;** it was taken more as a means to compare the G values with those obtained for the orthotropic case.

3.3.3. Computation of Fracture Parameters

3.3.3.1. Numerical Schemes

There have been very few numerical studies concerned with the fracture mechanics aspects of the Iosipescu shear test. [7,26,27] Hence, there is a need for further work in this direction. The displacement extrapolation technique, J-integral, and VCC-methods are very well established in linear elastic fracture mechanics of homogeneous isotropic

materials. However, the extrapolation and VCC-schemes haven't been thoroughly investigated for orthotropic fracture analysis. Since the code development for orthotropic material behavior is not the same in all commercially available finite element programs (ANSYS 4.4A[77] in this study), one can't rely on the fracture parameters obtained without any prior validation. Moreover, considering the fact that this is the first attempt at numerically investigating mixed mode fracture under **biaxial loading conditions** in orthotropic Iosipescu specimens, it was all the more necessary to firstly validate the chosen numerical schemes. In order to verify the numerical schemes for orthotropic fracture analysis, a single edge-crack in an orthotropic strip under uniaxial tension was considered. The reference solution by Kaya and Erdogan[78] provided a simple means for comparison, and thereby to check the accuracy of the numerical schemes. In an earlier study, Buchholz and co-workers[26,27] chose the same test problem in order to validate the VCC-scheme for orthotropic Iosipescu specimen under pure shear ($\phi = 0^\circ$) loading conditions. The numerical results obtained by the VCC schemes (2C- and 1C-methods) and the displacement method – equation (2.11), for the above test problem, are listed in Appendix D. It can be seen from Tables D.1 – D.3, that there is very good agreement between the numerical and reference solution[78] results. Due to the excellent results obtained for the test problem, some confidence was attained in the methods, prior to their application to the case of coplanar cracks in the Iosipescu specimen.

The stress intensity factors K_I and K_{II} are widely used in the fracture analysis of isotropic materials; however, in composite fracture mechanics, the energy release rates G_I, G_{II}, and G are more frequently applied. In keeping with the norm, all the numerical results that follow in Section 3.3.4 are expressed in terms of G_I, G_{II}, and G. In the following sub-sections, the implementation of the displacement extrapolation methods, J-

integral, and the VCC-schemes are outlined.

(i) Displacement Method – Equation (2.11)

The displacement method using (2.11) provides a simple means to evaluate the stress intensity factors K_I and K_{II} from the crack-tip displacements. Using (2.10) and (2.11), the stress intensity factors in orthotropic materials for plane stress problems can be written as

$$K_I = \sqrt{\frac{\pi}{2}} \frac{\mu_1 \mu_2}{a_{22}(\mu_1 + \mu_2)} \left[\frac{4u_{By} - u_{Cy}}{\sqrt{L}} \right] \qquad (3.4)$$

and

$$K_{II} = \sqrt{\frac{\pi}{2}} \frac{1}{a_{11}(\mu_1 + \mu_2)} \left[\frac{4u_{Bx} - u_{Cx}}{\sqrt{L}} \right] \qquad (3.5)$$

where L is the crack-tip element size; B and C are the evaluation points – B is the quarter-point node, while C is the corner node along the crack-tip element (Figure 2.8); μ_1 and μ_2 are the roots of the transcendental equation (2.12); and, a_{11} and a_{22} are the elastic compliances (Section 2.4.1).

The stress intensity factors were evaluated by the above approach, and subsequently the energy release rates G_I and G_{II} were computed from (2.20) and (2.21). Since the problem under consideration is for orthotropic materials under mixed mode loading conditions, the stress intensity values obtained from the upper and lower crack faces may differ; hence, K_I and K_{II} were calculated from the nodal displacements at points B and C (Figure 2.8) on either crack face.

(ii) Displacement Extrapolation Method

The most accurate results for the stress intensity factor from the crack-tip displacements are obtained by the displacement extrapolation method. For cracks in homogeneous isotropic materials, the KCALC command on ANSYS 4.4A[77] was used to automatically evaluate the stress intensity factors by a displacement extrapolation technique. However, for the orthotropic cracked-Iosipescu specimen, the analysis had to be manually performed. A linear regression of the displacements scaled by $r^{1/2}$ from $r = 0.025$mm to $r = 0.4$mm was carried out; the analysis was performed separately for the upper and lower crack faces (Figure 3.35a). The best-fit straight line was obtained and extrapolated to the crack-tip ($r = 0$). Using the x-displacements in the analysis, the parameter u_x^* was obtained at $r = 0$, while the y-displacements yielded the parameter u_y^* at $r = 0$ (Figure 3.35b). Substituting u_x^* and u_y^* instead of $(4u_{Bx} - u_{Cx})/\sqrt{L}$ and $(4u_{By} - u_{Cy})/\sqrt{L}$ in (3.4) and (3.5) respectively, the stress intensity factors, and thereafter the energy release rates were computed.

(iii) J-Integral

The J-integral[32] characterizes the crack-tip stress state in linear as well as nonlinear elastic materials. In case of isotropic materials (linear elastic), the J-integral is equivalent to the energy release rate G. Since J is a path-independent integral, the J results obtained along any path around the crack-tip must yield the same value. The macro JIN2.MAC, which is available on ANSYS 4.4A, [77] was used in the estimation of the J-integral; two different paths were considered in the J-integral calculations (Figure 3.36).

(iv) Virtual Crack Closure (2C-method)

The virtual crack closure (2C-method) scheme was outlined in Section 2.4.2.3. Two finite element analyses at crack lengths a and $a + \Delta a$ respectively were performed. From the first analysis (crack length a), the forces ahead of the crack tip were determined, while from the second analysis (crack length $a + \Delta a$), the displacements behind the crack-tip were evaluated. Using the nodal displacements and the nodal forces, the mode partitions G_I and G_{II} were estimated from (2.22a) and (2.22b) respectively.

(v) Virtual Crack Closure (1C-method)

The modified virtual crack closure (1C-method) technique, wherein only one analysis is required to be performed, was outlined in Section 2.4.2.3. The displacements behind the crack tip, and the nodal forces ahead of the crack tip were computed. Subsequently, the G-components, namely, G_I and G_{II} were evaluated using (2.23a) and (2.23b) respectively.

3.3.3.2. Beam Theory Solutions

On the basis of Williams' beam theory analysis for cracked laminates, [47] an analytical model for the energy release rates in cracked Iosipescu specimens under biaxial loading conditions was proposed. [79] The details of the approach and the expressions obtained for G, G_I, and G_{II} are presented in Appendix C. The moment M_2 and it's derivative dM_2/da were evaluated from (C.1)–(C.6) in Appendix C, and then substituted into equations (C.7)–(C.9), to obtain the estimates for G, G_I, and G_{II} respectively. Since the mixed mode energy release rate G obtained from the analytical solution was significantly

different in comparison to the J-integral values, the analytical results for G from (C.7) were not considered in this study; instead, the sum $G_I + G_{II}$ was taken to be the analytical estimate for the mixed mode energy release rate G.

3.3.4. Energy Release Rates G_I, G_{II}, and G

The mode partitions G_I and G_{II}, and the mixed mode energy release rate G ($G_I + G_{II}$) were evaluated by all the schemes discussed in the previous section. A detailed listing of all the numerical and analytical results is included in Appendix E. The J-integral values along the paths Γ_1 and Γ_2 (Figure 3.36) differed by 2% or less; the J-integral values listed in Appendix E are the average of the two path calculations. Herein, some of the important results and observable trends are presented.

It can be seen from the results obtained for the edge-crack in an orthotropic strip under tension (Appendix D), that the VCC-2C method is the most accurate among all the numerical schemes considered in this study. Hence, the VCC-2C results were taken as the representative numerical solution for G_I, G_{II}, and G. In Table 3.7, the numerical results obtained by the displacement method – equation (2.11) for the particular case of $\phi = 0°$ and ER = 14.2 (A-type) are compared to the VCC-2C results. The loading angle $\phi = 0°$ (pure shear) is used by practitioners involved in the analysis of the Iosipescu shear test; also, based on the experimental findings of Broughton, [2] crack lengths of 10-13mm are observable in the Iosipescu shear test, for the specimen dimensions shown in Figure 3.2. In light of the above two facts, the VCC-2C and beam solution results will be presented for the above conditions.

In Figure 3.37a, the deformed structure for $a = 10$mm, $\phi = 0°$, and ER = 14.2 (A-type) is shown, while in Figure 3.37b, the deformation of the crack-tip region is

illustrated. It is apparent from the above deformed plots that the displacements around the crack tip exhibit mixed mode fracture conditions. In Table 3.8, the total energy release rates are listed for $a = 10mm$ and ER $= 1$, while in Table 3.9, the results are presented for ER $= 14.2$ (A-type). In Figures 3.38a and 3.38b, the above data is shown for isotropic and orthotropic (A-type) Iosipescu specimens respectively. The total energy release rate G monotonically decreases as ϕ is varied from $\phi = -45°$ to $\phi = 30°$. The only exception is $\phi = -45°$ for ER $= 14.2$ (A-type), where there is a noticeable decrease in the G value. In Table 3.10, the total energy release rates are listed as a function of the crack length a, for the loading angle $\phi = 0°$ and ER $= 1$, while in Table 3.11, the results are presented for ER $= 14.2$ (A-type). In Figures 3.39a and 3.39b, the above data is illustrated for isotropic and orthotropic (A-type) Iosipescu specimens respectively. For short and medium length cracks, there is very poor agreement between the G values obtained by the beam solution and those from the VCC-2C scheme; however, for long cracks ($a \geq 10mm$), there is a reasonable match between the beam solution and VCC-2C results. In Table 3.12, the energy release rates G_I (opening mode) and G_{II} (shearing mode) are listed for $a = 10mm$ and ER $= 1$, while in Table 3.13, the results are presented for ER $= 14.2$ (A-type). In Figures 3.40a and 3.40b, the above data is shown for isotropic and orthotropic (A-type) Iosipescu specimens respectively. The trends exhibited by G_I and G_{II} are similar to those observed for G; both, G_I and G_{II} decrease as ϕ changes from $-\phi$ to $+\phi$, with $\phi = -45°$ and ER $= 14.2$ (A-type) being the sole and notable exception to the general trend. In Table 3.14, the mode partitions G_I and G_{II} are listed as a function of the crack length a, for the loading angle $\phi = 0°$ and ER $= 1$, while in Table 3.15, the results are presented for ER $= 14.2$ (A-type). In Figures 3.41a and 3.41b, the above data is illustrated for isotropic and orthotropic (A-type) Iosipescu specimens respectively. It

can be seen from Tables 3.12 − 3.15, that the results for G_I and G_{II} by the beam solution are in total disagreement with the VCC-2C results.

Table 3.1. Input elastic properties[8] of the materials used in the analysis for the finite element and Finite Element Iterative Method.

Material	Isotropic	Glass/polyester	Carbon/epoxy
ER	1.00	3.45	14.20
E_{11} (GPa)	3.60	37.00	137.90
E_{22} (GPa)	3.60	10.70	9.70
ν_{12}	0.36	0.27	0.25
G_{12} (GPa)	1.40	4.00	4.20

Table 3.2. Shear stress concentration (K_t) at the notch root as a function of notch–root element size.

Notch-root element size (mm)	Orthotropy ratio ER	Shear stress concentration K_t
0.50	14.2 (B)	0.5149
	3.45 (B)	0.7009
	1.0	1.1023
	3.45 (A)	1.5120
	14.2 (A)	2.1579
0.25	14.2 (B)	0.4740
	3.45 (B)	0.6889
	1.0	1.1699
	3.45 (A)	1.7081
	14.2 (A)	2.5409
0.10	14.2 (B)	0.4225
	3.45 (B)	0.6738
	1.0	1.2435
	3.45 (A)	2.0071
	14.2 (A)	3.1562

Table 3.3. Stress singularity (λ_a) in tension.

ER	Strong Singularity (λ_a)						
	$\alpha = 0°$	$\alpha = 60°$	$\alpha = 75°$	$\alpha = 90°$	$\alpha = 105°$	$\alpha = 120°$	$\alpha = 150°$
14.2 (B)	0.4989	0.4601	0.4390	0.4128	0.3802	0.3386	0.2149
3.45 (B)	0.4990	0.4758	0.4587	0.4358	0.4055	0.3652	0.2378
1	0.4992	0.4873	0.4747	0.4547	0.4248	0.3823	0.2452
1	0.5000*	0.4878*	0.4752*	0.4555*	0.4261*	0.3843*	0.2480*
3.45 (A)	0.4976	0.4926	0.4869	0.4777	0.4627	0.4390	0.3321
14.2 (A)	0.4890	0.4900	0.4869	0.4894	0.4793	0.4698	0.4072

* Theoretical solution by Williams[50]

Table 3.4 Stress singularity (λ_b) in shear.

ER	Weak Singularity (λ_b)						
	$\alpha=0°$	$\alpha=60°$	$\alpha=75°$	$\alpha=90°$	$\alpha=105°$	$\alpha=120°$	$\alpha=150°$
14.2 (B)	0.4975	0.0430	0.0046	0.0001	0.0000	0.0000	0.0000
3.45 (B)	0.4970	0.1476	0.0647	0.0083	0.0002	0.0000	0.0000
1	0.4978	0.2715	0.1889	0.0924	0.0093	0.0000	0.0000
1	0.5000*	0.2691*	0.1868*	0.0915*	0.0000*	0.0000*	0.0000*
3.45 (A)	0.4981	0.3072	0.2453	0.1758	0.0957	0.0157	0.0000
14.2 (A)	0.4979	0.3403	0.2878	0.2329	0.1577[+]	0.0980[+]	0.0116[+]

* Theoretical solution by Williams[50]
+ 'Expected' values; convergence wasn't observed

Table 3.5. Stress singularity under mixed mode loading for $\alpha = 90°$.

ER	Stress Singularity				
	$\phi = 45°$	$\phi = 60°$	$\phi = 75°$	$\phi = 89.5°$	$\phi = 89.9°$
14.2 (B)	0.4128	0.4128	0.4128	0.4128	0.4128
1	0.4547	0.4547	0.4547	0.4547	0.4547
14.2 (A)	0.4861	0.4861	0.4861	0.4861	0.4861

Table 3.6. Convergence under mixed mode loading (ER = 1 and $\alpha = 90°$).

Number of iterations	Stress Singularity				
	$\phi = 45°$	$\phi = 60°$	$\phi = 75°$	$\phi = 89.5°$	$\phi = 89.9°$
1	0.4620	0.4675	0.4834	-0.3116	0.0471
2	0.4562	0.4571	0.4595	0.6868	-0.3786
3	0.4553	0.4554	0.4558	0.4790	0.6252
4	0.4551	0.4551	0.4552	0.4588	0.4747
5	0.4551	0.4551	0.4551	0.4557	0.4582
6	0.4551	0.4551	0.4551	0.4552	0.4556
7	0.4551	0.4551	0.4551	0.4551	0.4551
8	0.4551	0.4551	0.4551	0.4551	0.4551

Table 3.7. Comparison of energy release rates (G_I, G_{II}, G) by the displacement method and the VCC-2C scheme: ER = 14.2 (A-type) and $\phi = 0^\circ$.

	Displacement method[†] – equation (2.11)									VCC-2C scheme		
a	G_I^U	G_I^L	$G_I^{avg.}$	G_{II}^U	G_{II}^L	$G_{II}^{avg.}$	G^U	G^L	$G^{avg.}$	G_I	G_{II}	G
(mm)					(kJ/m^2)						(kJ/m^2)	
1	0.810	0.240	0.525	0.045	0.095	0.070	0.855	0.335	0.595	0.952	0.088	1.040
4	0.642	0.204	0.423	0.132	0.204	0.168	0.774	0.408	0.591	0.774	0.218	0.992
7	0.388	0.132	0.260	0.166	0.228	0.197	0.554	0.360	0.457	0.482	0.255	0.736
10	0.204	0.073	0.139	0.146	0.187	0.167	0.350	0.261	0.306	0.258	0.216	0.474
13	0.095	0.037	0.066	0.111	0.136	0.124	0.206	0.173	0.190	0.125	0.159	0.284

† Superscripts U and L refer to values computed from the upper and lower crack faces respectively.

Table 3.8. Mixed mode energy release rate G ($G_I + G_{II}$) for ER = 1 and a = 10mm.

ϕ (degree)	G^{BE} (kJ/m^2)	G^{VCC-2C} (kJ/m^2)
-45	126.447	33.660
-30	34.094	21.644
-15	17.840	15.219
0	10.030	9.381
15	5.147	4.415
30	2.116	1.111

Table 3.9. Mixed mode energy release rate G ($G_I + G_{II}$) for ER = 14.2 (A-type) and a = 10mm.

ϕ (degree)	G^{BE} (kJ/m^2)	G^{VCC-2C} (kJ/m^2)
-45	3.301	0.524
-30	0.890	0.643
-15	0.466	0.605
0	0.262	0.474
15	0.134	0.298
30	0.055	0.131

Table 3.10. Mixed mode energy release rate G ($G_I + G_{II}$) for ER = 1 and $\phi = 0°$.

a (mm)	G^{BE} (kJ/m^2)	G^{VCC-2C} (kJ/m^2)
0	0.000	0.000
1	0.199	5.211
4	3.177	9.087
7	7.823	10.302
10	10.030	9.381
13	8.575	7.488

Table 3.11. Mixed mode energy release rate G ($G_I + G_{II}$) for ER = 14.2 (A-type) and $\phi = 0°$.

a (mm)	G^{BE} (kJ/m^2)	G^{VCC-2C} (kJ/m^2)
0	0.000	0.000
1	0.005	1.040
4	0.083	0.993
7	0.204	0.736
10	0.262	0.474
13	0.224	0.284

Table 3.12.   Mode partitions G_I and G_{II} for ER = 1 and a = 10mm.

ϕ (degree)	Beam solution		Virtual crack closure	
	G_I^{BE} (kJ/m^2)	G_{II}^{BE} (kJ/m^2)	G_I^{VCC-2C} (kJ/m^2)	G_{II}^{VCC-2C} (kJ/m^2)
-45	3.986	122.461	16.203	17.457
-30	1.075	33.019	10.387	11.256
-15	0.562	17.278	7.290	7.929
0	0.316	9.714	4.484	4.897
15	0.162	4.984	2.104	2.311
30	0.067	2.049	0.525	0.586

Table 3.13.   Mode partitions G_I and G_{II} for ER = 14.2 (A-type)
and a = 10mm.

ϕ (degree)	Beam solution		Virtual crack closure	
	G_I^{BE} (kJ/m^2)	G_{II}^{BE} (kJ/m^2)	G_I^{VCC-2C} (kJ/m^2)	G_{II}^{VCC-2C} (kJ/m^2)
-45	0.104	3.197	0.224	0.301
-30	0.028	0.862	0.325	0.318
-15	0.015	0.451	0.321	0.284
0	0.008	0.254	0.258	0.216
15	0.004	0.130	0.166	0.132
30	0.002	0.054	0.075	0.056

Table 3.14.   Mode partitions G_I and G_{II} for ER = 1 and $\phi = 0°$.

a	Beam solution		Virtual crack closure	
	G_I^{BE}	G_{II}^{BE}	G_I^{VCC-2C}	G_{II}^{VCC-2C}
(mm)	(kJ/m^2)	(kJ/m^2)	(kJ/m^2)	(kJ/m^2)
0	0.000	0.000	0.000	0.000
1	0.006	0.192	4.183	1.028
4	0.100	3.077	5.697	3.390
7	0.247	7.577	5.515	4.787
10	0.316	9.714	4.484	4.897
13	0.270	8.305	3.289	4.199

Table 3.15.   Mode partitions G_I and G_{II} for ER = 14.2 (A-type) and $\phi = 0°$.

a	Beam solution		Virtual crack closure	
	G_I^{BE}	G_{II}^{BE}	G_I^{VCC-2C}	G_{II}^{VCC-2C}
(mm)	(kJ/m^2)	(kJ/m^2)	(kJ/m^2)	(kJ/m^2)
0	0.000	0.000	0.000	0.000
1	0.000	0.005	0.952	0.088
4	0.003	0.080	0.774	0.218
7	0.006	0.198	0.482	0.255
10	0.008	0.254	0.258	0.216
13	0.007	0.217	0.125	0.159
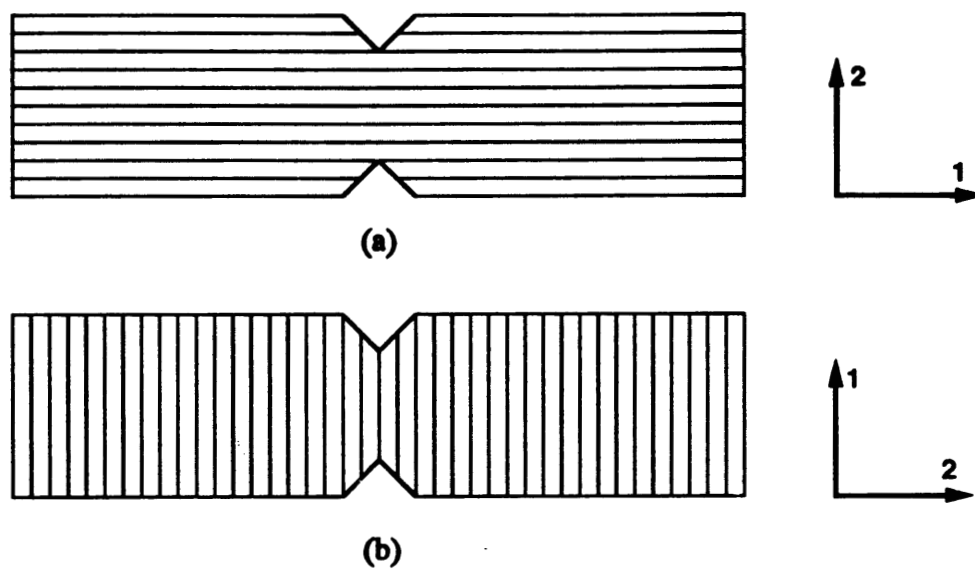
Figure 3.1 Fiber orientations in Iosipescu specimen.
(a) 0-deg (orientation A); and
(b) 90-deg (orientation B).

t = 1mm (plane stress)
h' = 20mm
w = 3h$_1$ = 12mm
L = 80mm
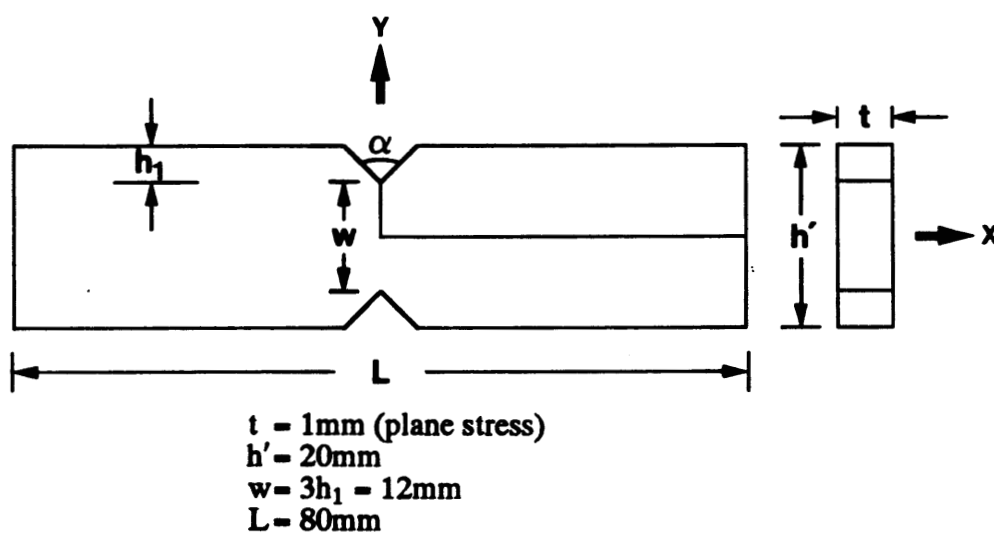
Figure 3.2 Schematic of Iosipescu specimen.
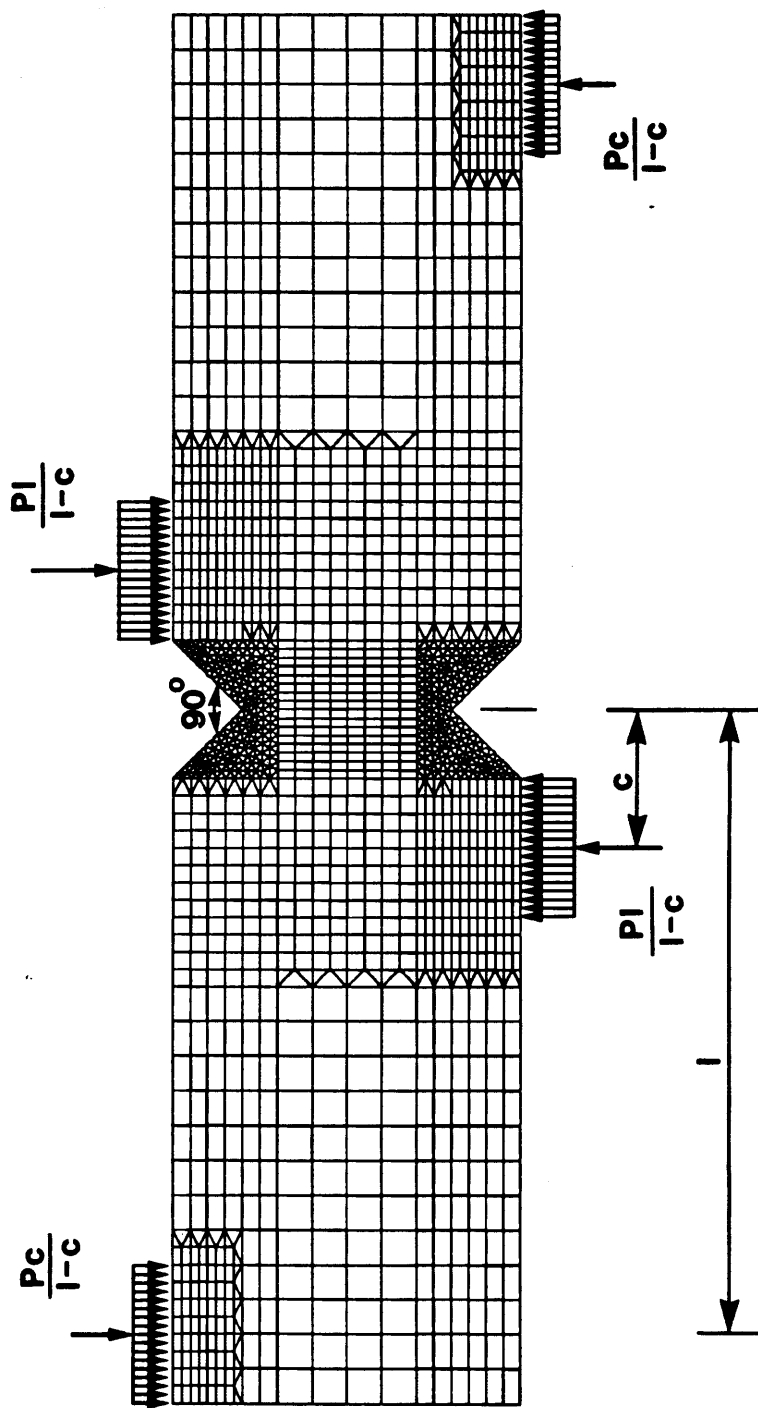
Figure 3.3 Finite element mesh of Iosipescu specimen ($\alpha = 90°$) with boundary conditions for $\phi = 0°$.

P = 115 N

(MPa)

0.587717
13.874
27.16
40.445
53.731
67.017
80.303
93.589
106.875
120.161

(a)

P = 115 N

(MPa)

0.149321
6.215
12.281
18.347
24.413
30.479
36.544
42.61
48.676
54.742
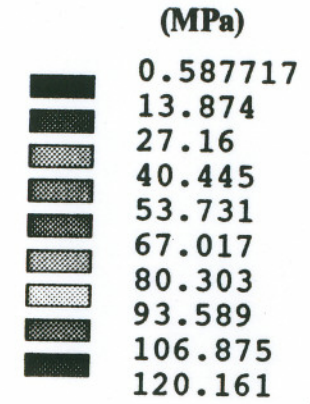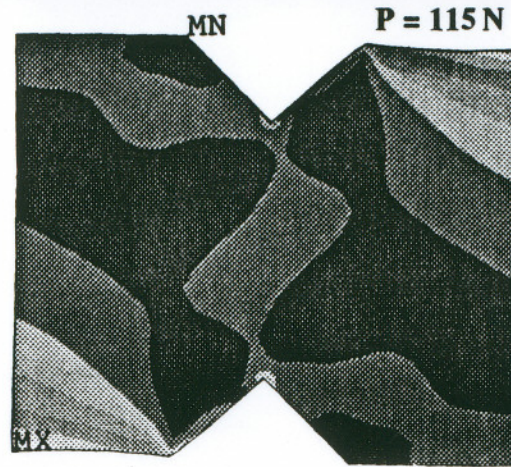
(b)
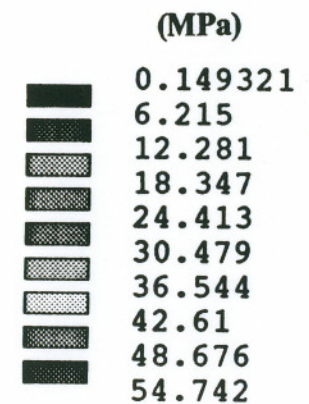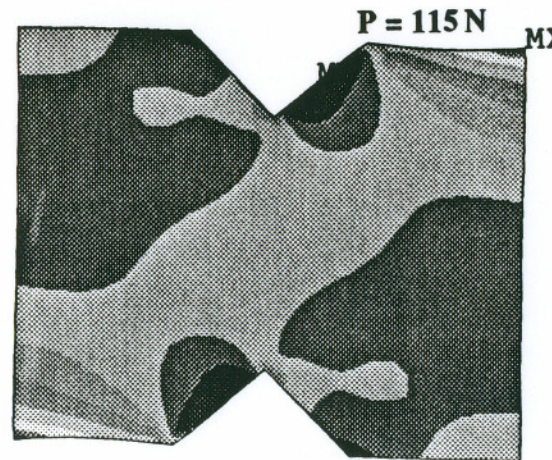
Figure 3.4 von Mises stress contours and isochromatic fringe patterns^2 for $\alpha = 90°$ and ER = 1 under shear-tension. (a) $\phi = -45°$; and (b) $\phi = -30°$.
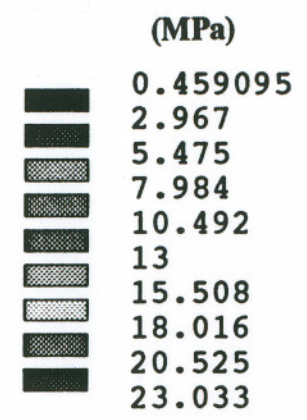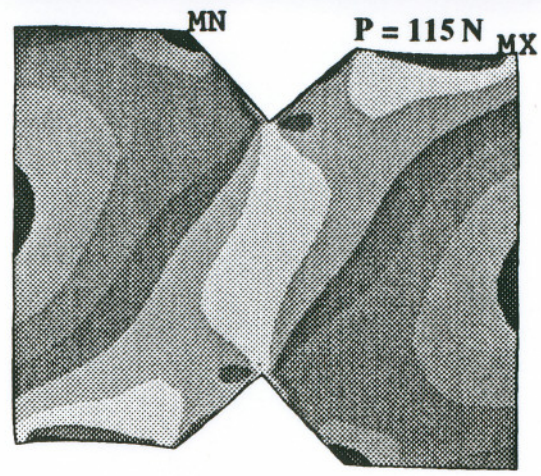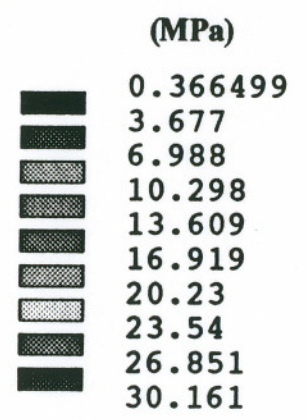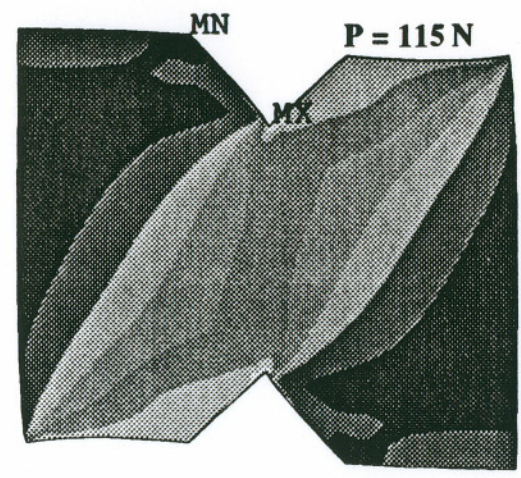
Figure 3.5 von Mises stress contours and isochromatic fringe patterns[2] for $\alpha = 90°$ and ER = 1. (a) $\phi = 0°$ (pure shear); and (b) $\phi = 30°$ (shear-compression).

P = 115 N MX
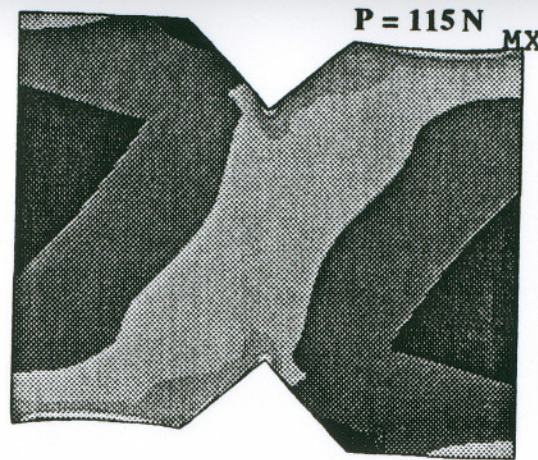
(MPa)

0.357846
6.312
12.266
18.219
24.173
30.127
36.081
42.035
47.989
53.943

Figure 3.6 von Mises stress contour and the isochromatic fringe pattern for $\alpha = 90°$ and ER = 14.2 (A-type) under pure shear.

P = 115 N
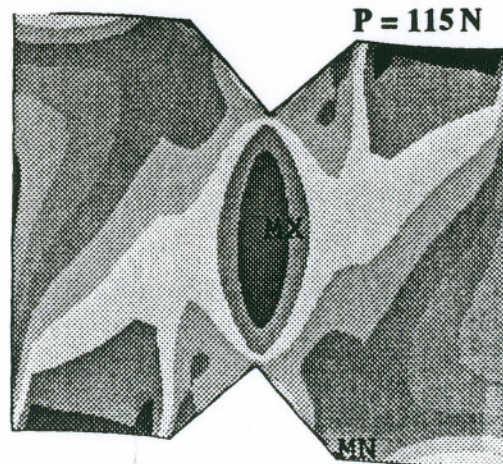
(MPa)

2.232
3.99
5.749
7.507
9.266
11.024
12.782
14.541
16.299
18.057

Figure 3.7 von Mises stress contour and the isochromatic fringe pattern[2] for $\alpha = 90°$ and ER = 14.2 (B-type) under pure shear.
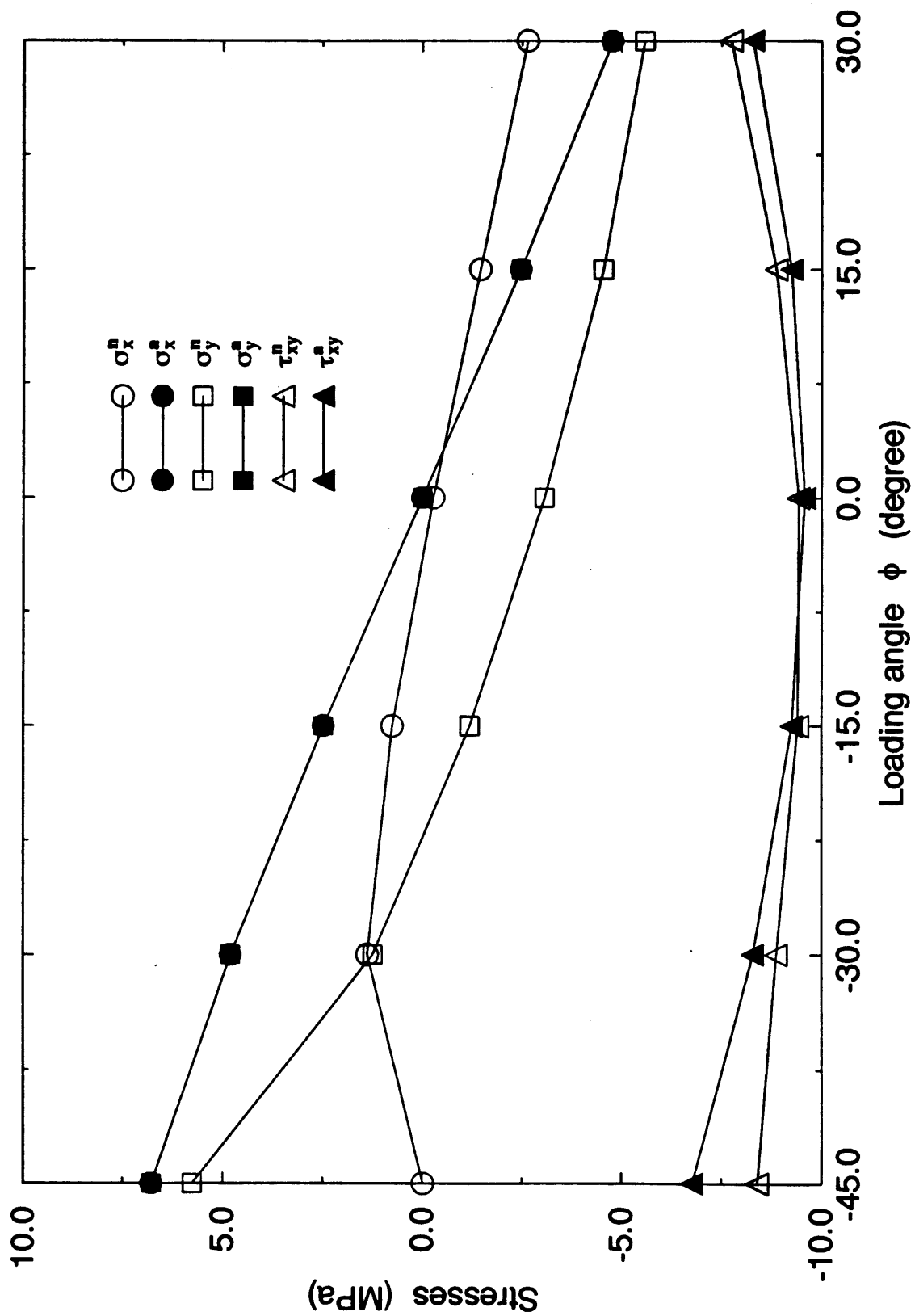
Figure 3.8 Normal and shear stresses at the center of isotropic Iosipescu specimens obtained from numerical and analytical computations.
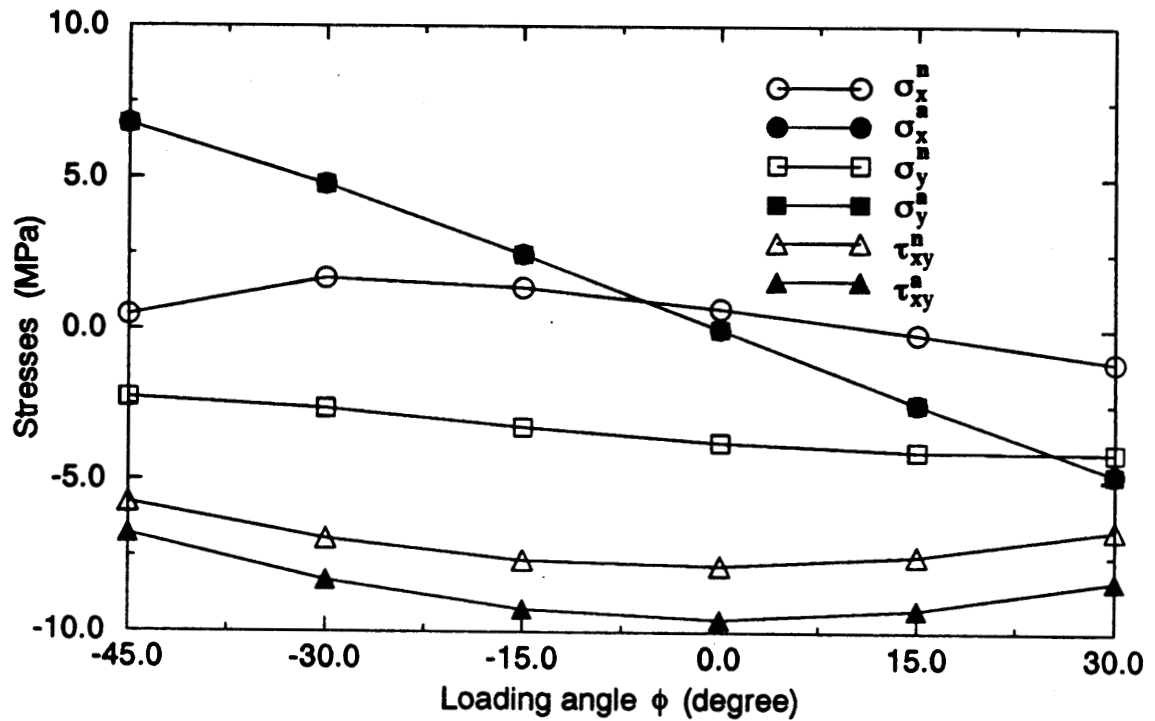
Figure 3.9 Normal and shear stresses at the center of orthotropic Iosipescu specimens (A–type) obtained from numerical and analytical computations.
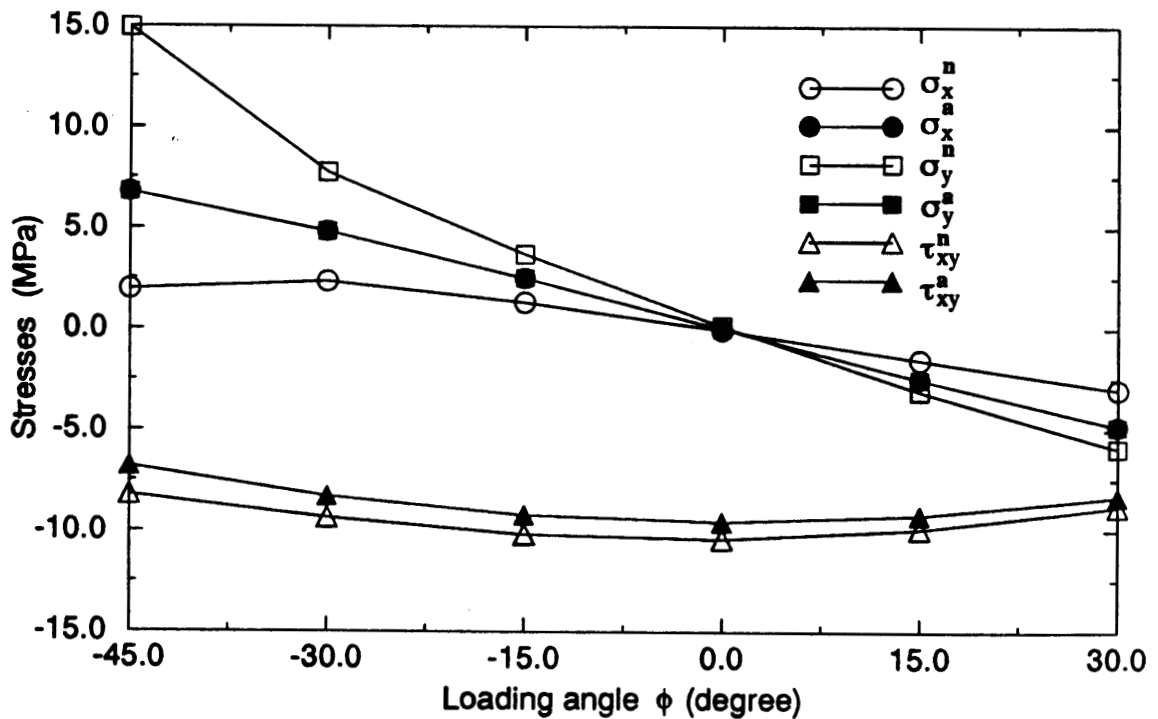
Figure 3.10 Normal and shear stresses at the center of orthotropic Iosipescu specimens (B–type) obtained from numerical and analytical computations.
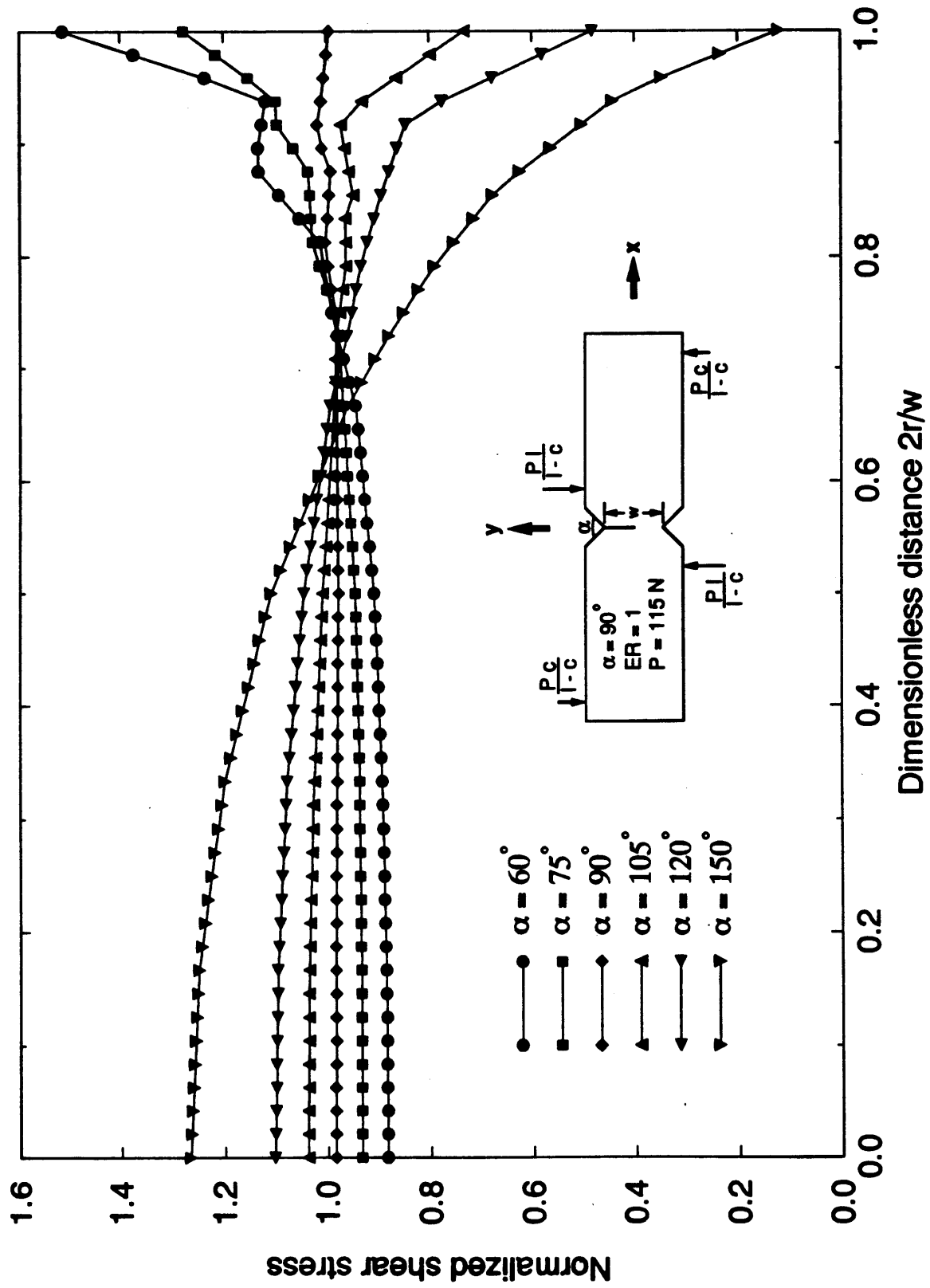
Figure 3.11 Variation of normalized shear stress between the center and the notch root for ER = 1 and $\phi = 0°$.
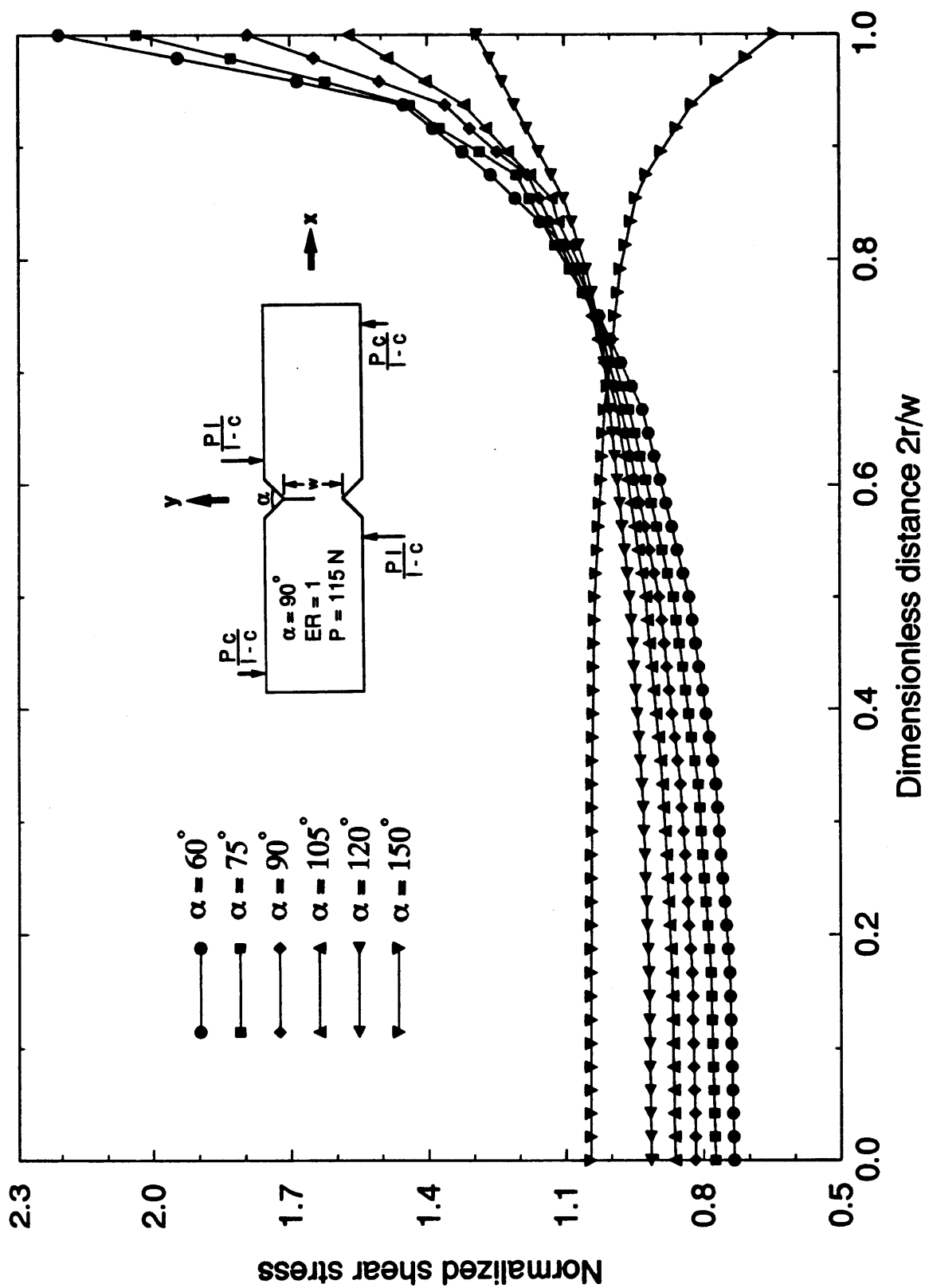
Figure 3.12 Variation of normalized shear stress between the center and the notch root for ER = 14.2 (A-type) and $\phi = 0°$.
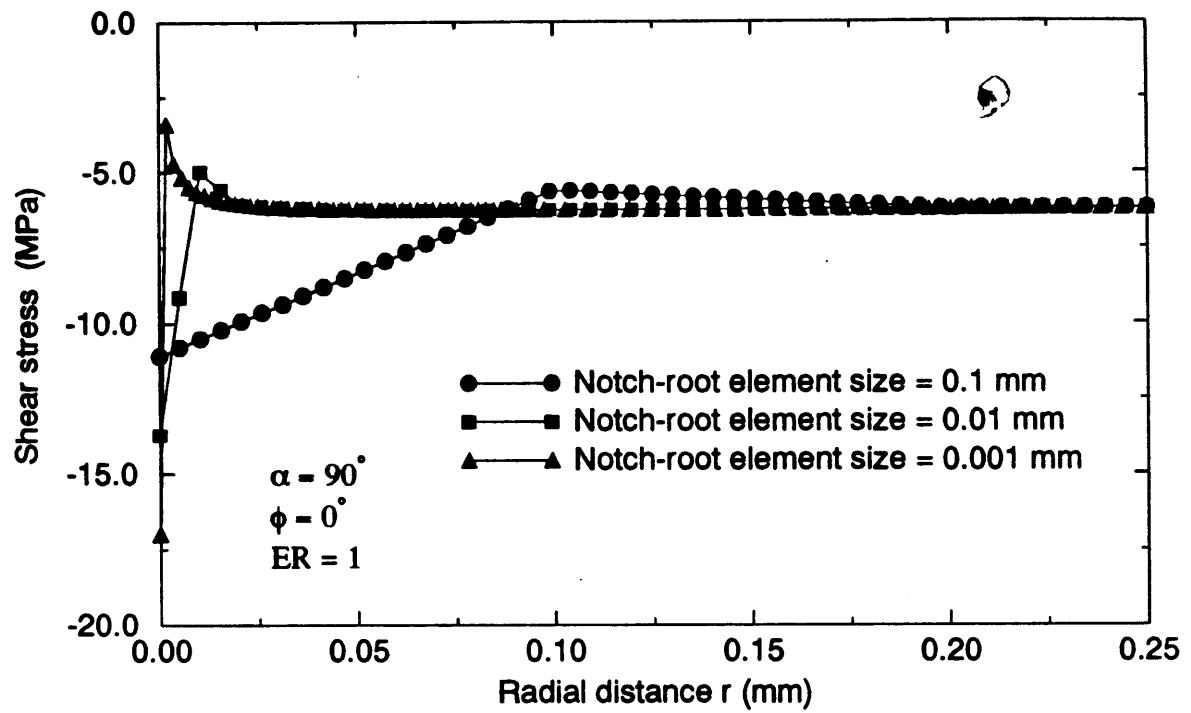
Figure 3.13 Shear stress distribution as a function of the notch-root element size.
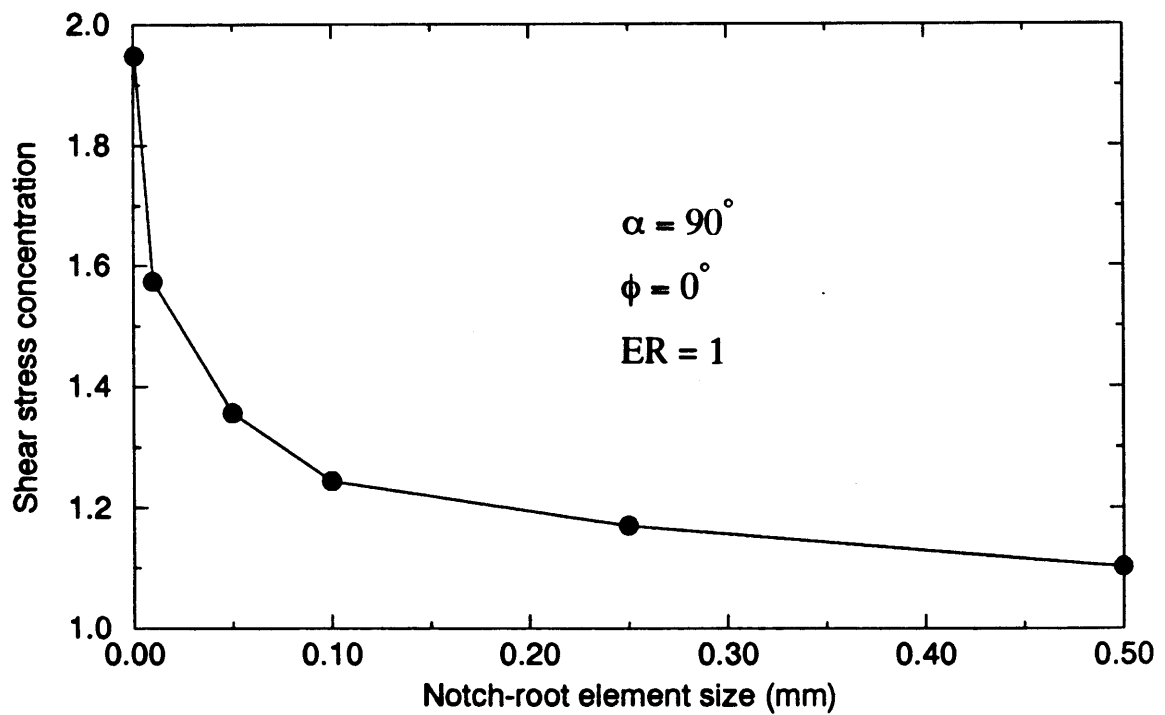
Figure 3.14 Plot of K_t versus the notch-root element size.

Figure 3.15 Plot of log K_t versus log ER for different notch-root element sizes.

The figure shows:

$$\log K_t = 0.3889 \log ER + 0.1629$$

$$\log K_t = 0.3254 \log ER + 0.1011$$

$$\log K_t = 0.2773 \log ER + 0.0522$$

$\alpha = 90°$

$\phi = 0°$

- Notch-root element size = 0.50 mm
- Notch-root element size = 0.25 mm
- Notch-root element size = 0.10 mm
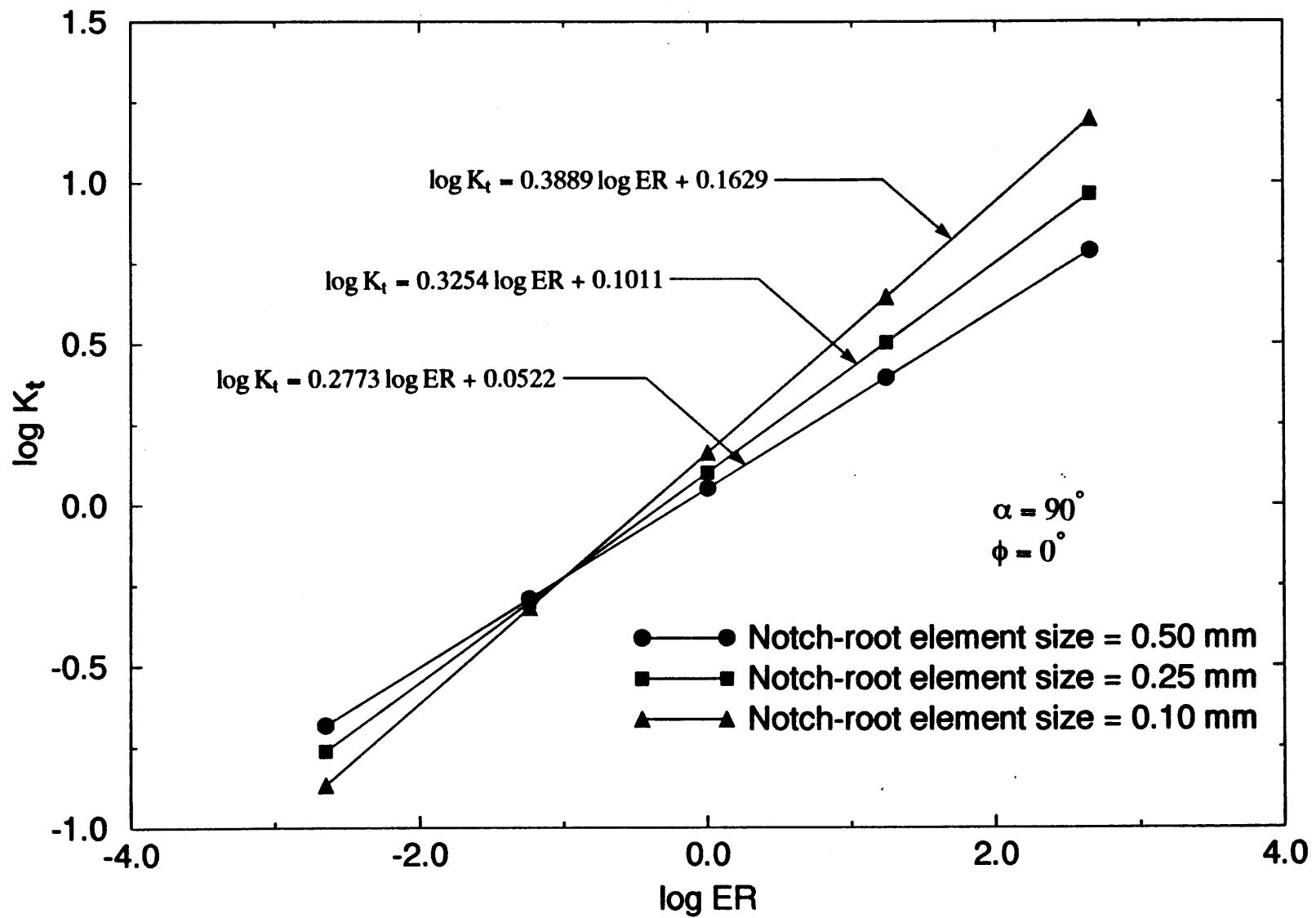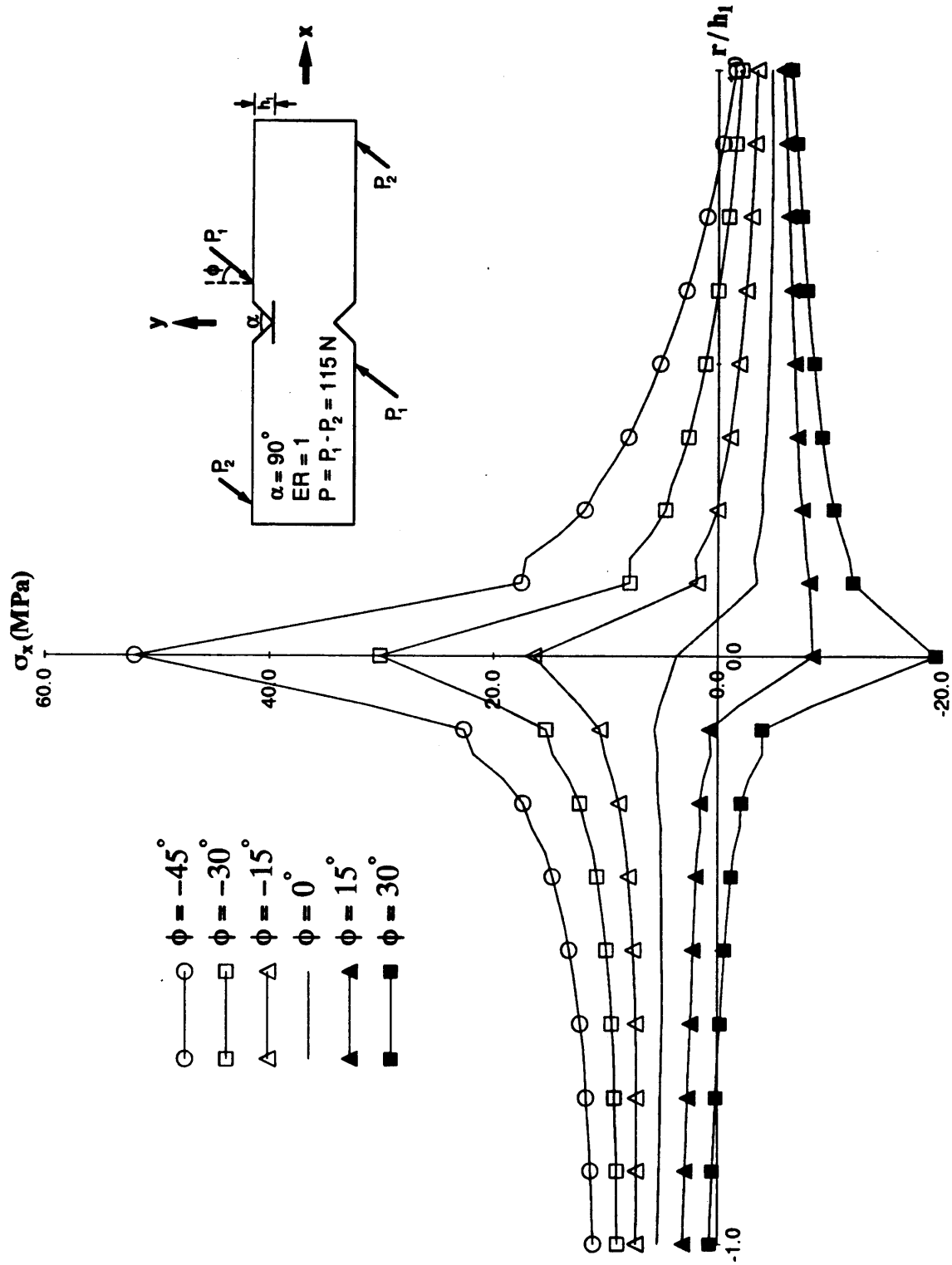
Figure 3.16 Normal stresses (σ_x) near the notch root in isotropic specimens along the line $y = w/2$ as a function of the loading angle ϕ.
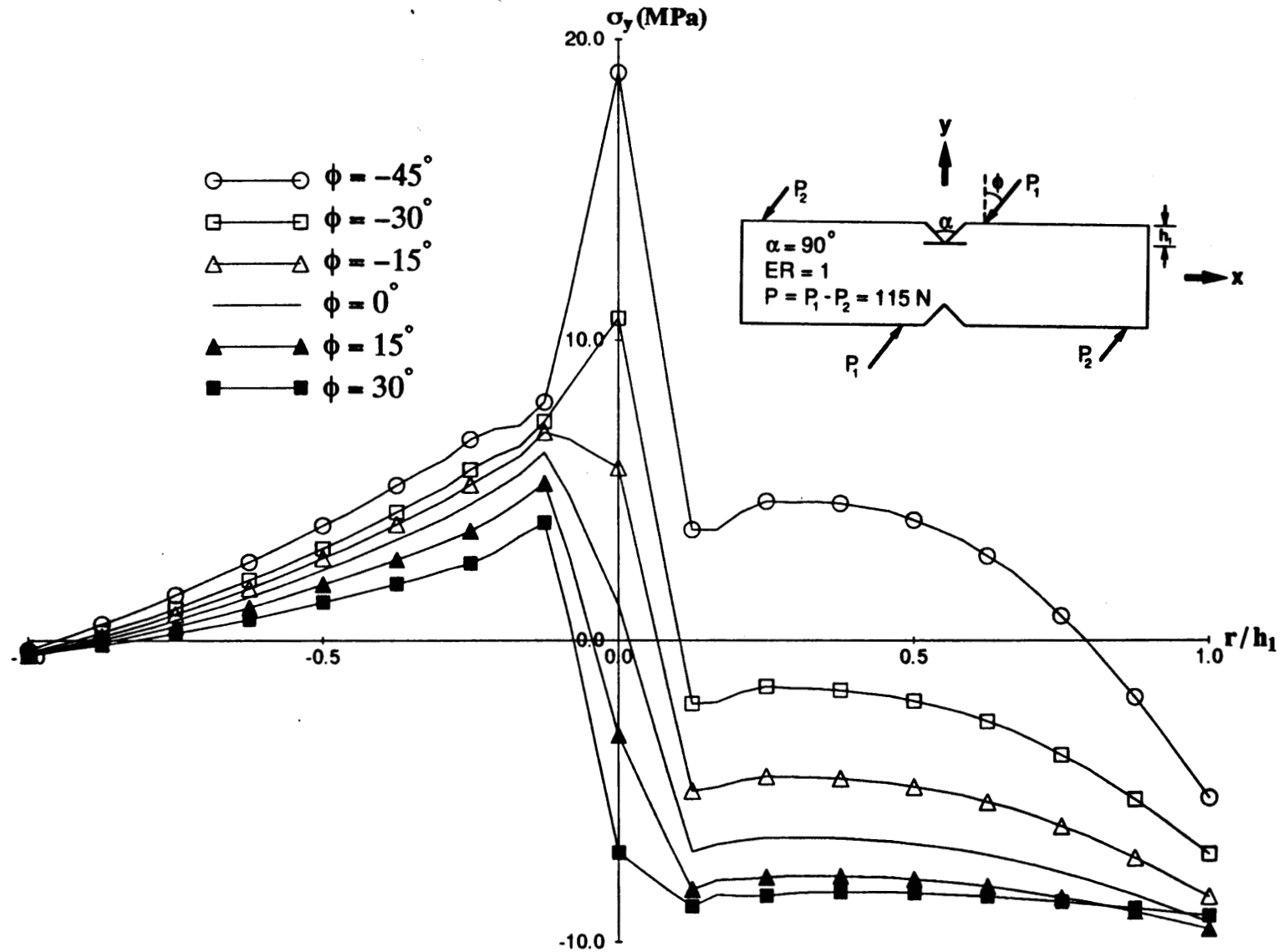
Figure 3.17 Normal stresses (σ_y) near the notch root in isotropic specimens along the line $y = w/2$ as a function of the loading angle ϕ.
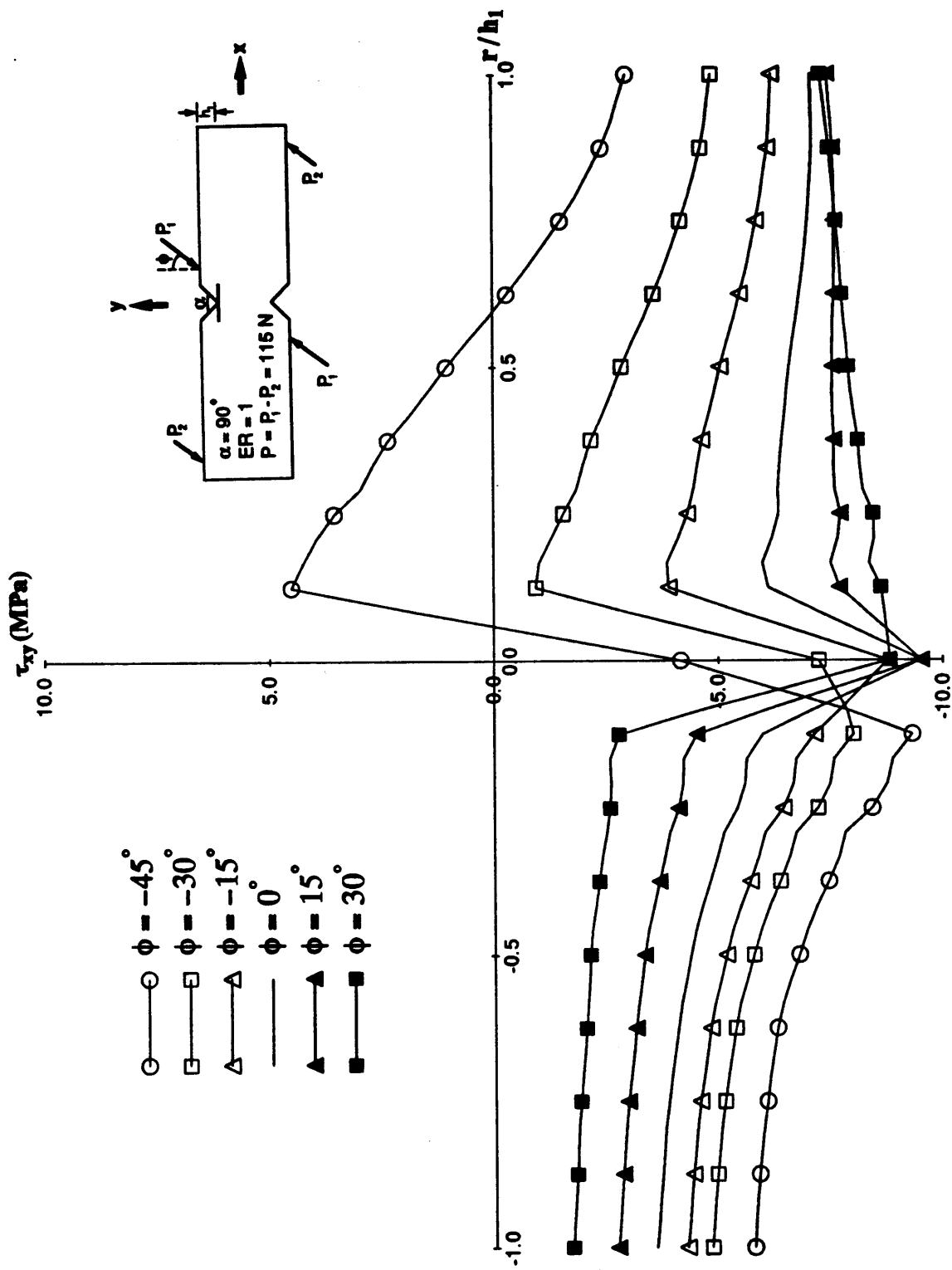
Figure 3.18 Shear stresses (τ_{xy}) near the notch root in isotropic specimens along the line $y = w/2$ as a function of the loading angle ϕ.
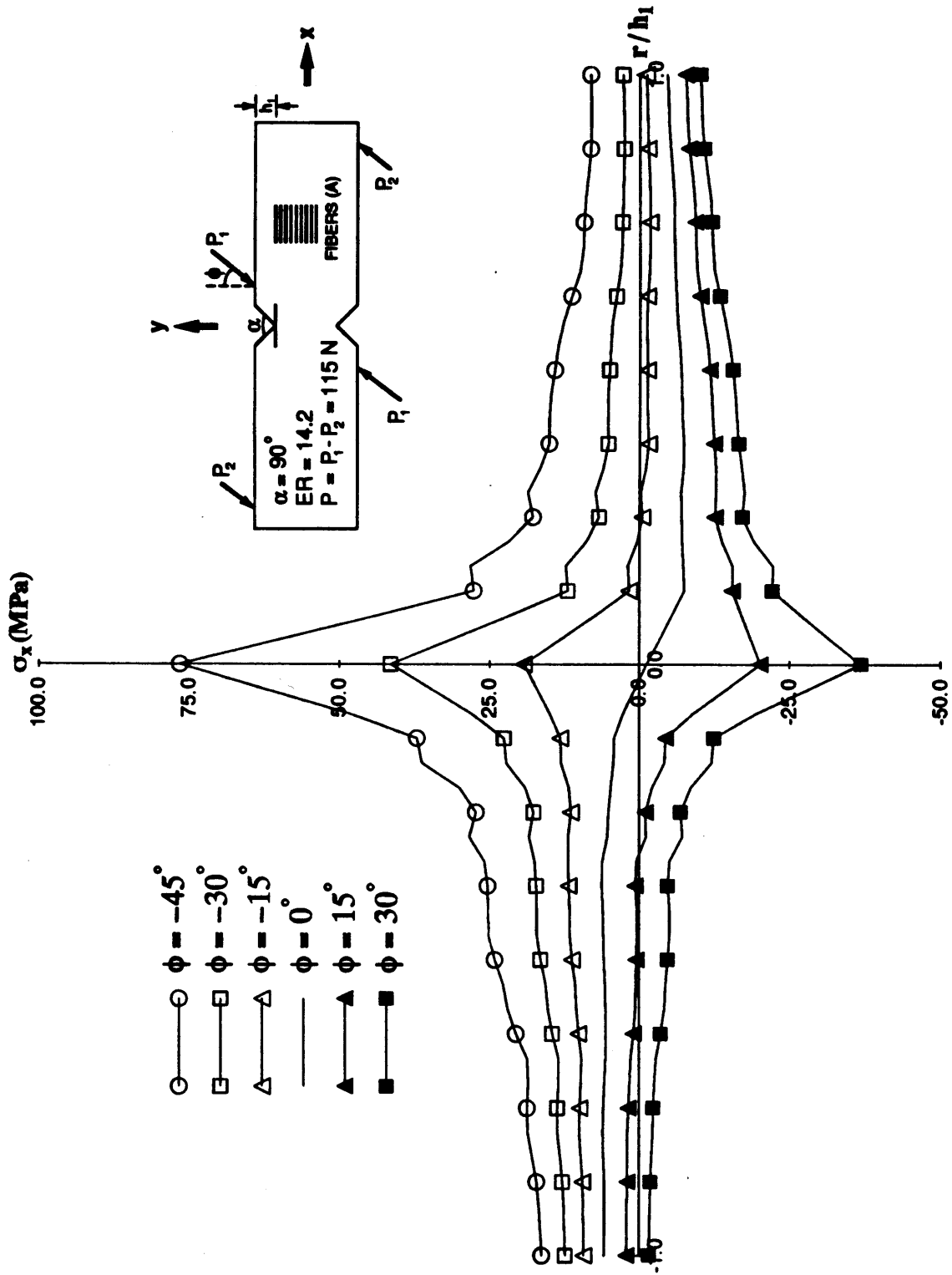
Figure 3.19 Normal stresses (σ_x) near the notch root in orthotropic specimens (A-type) along the line $y = w/2$ as a function of the loading angle ϕ.
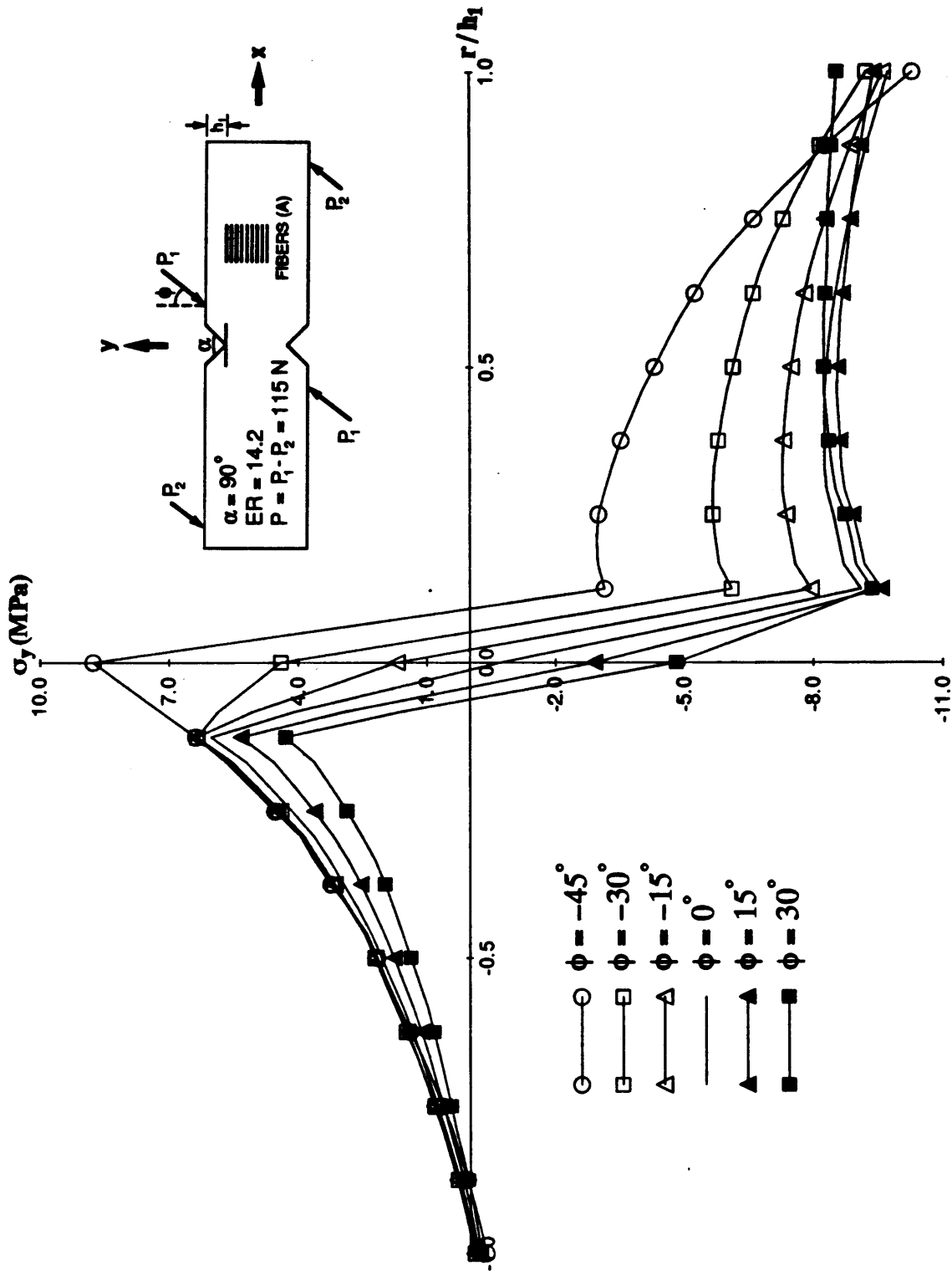
Figure 3.20 Normal stresses (σ_y) near the notch root in orthotropic specimens (A-type) along the line $y = w/2$ as a function of the loading angle ϕ.
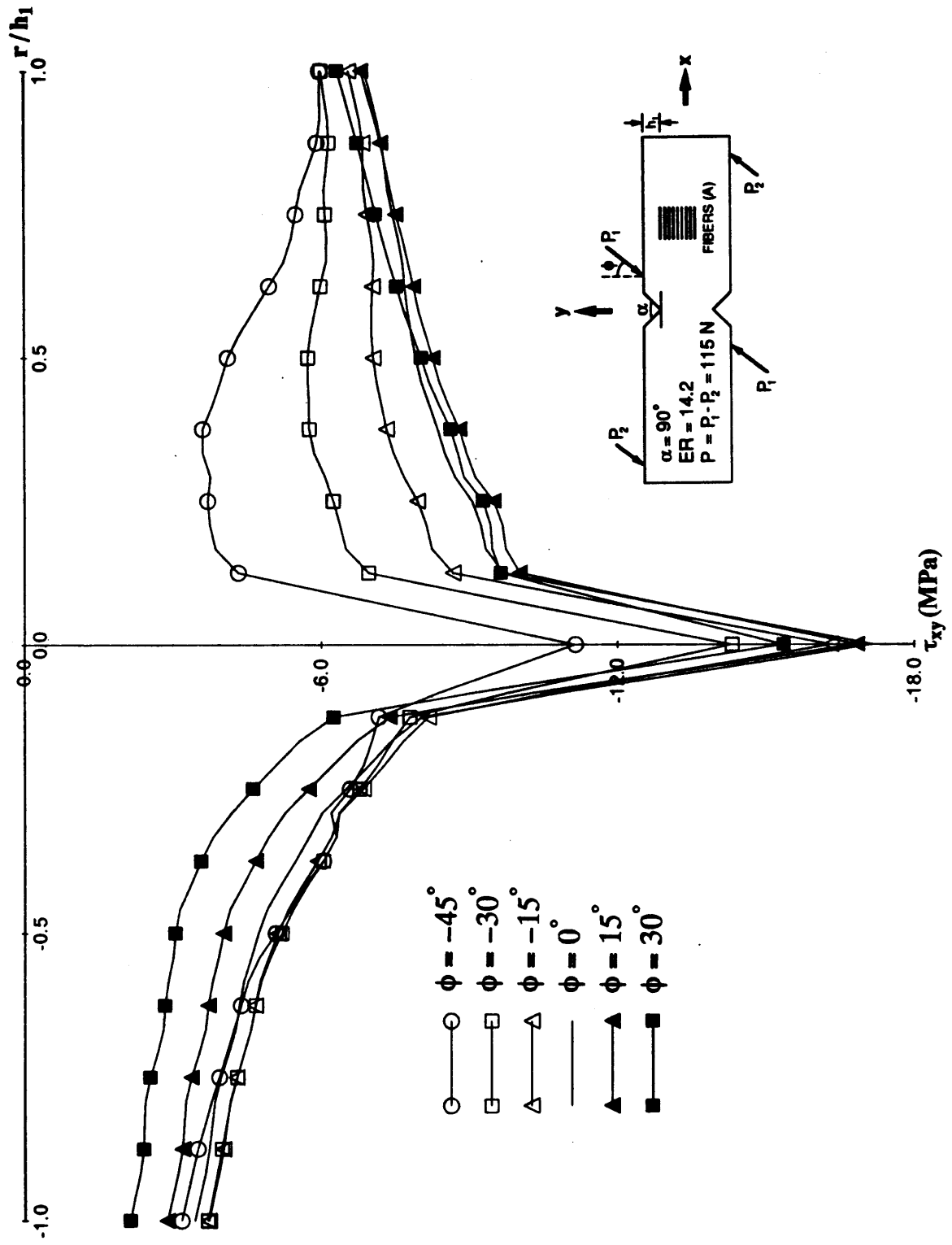
Figure 3.21 Shear stresses (τ_{xy}) near the notch root in orthotropic specimens (A-type) along the line $y = w/2$ as a function of the loading angle ϕ.
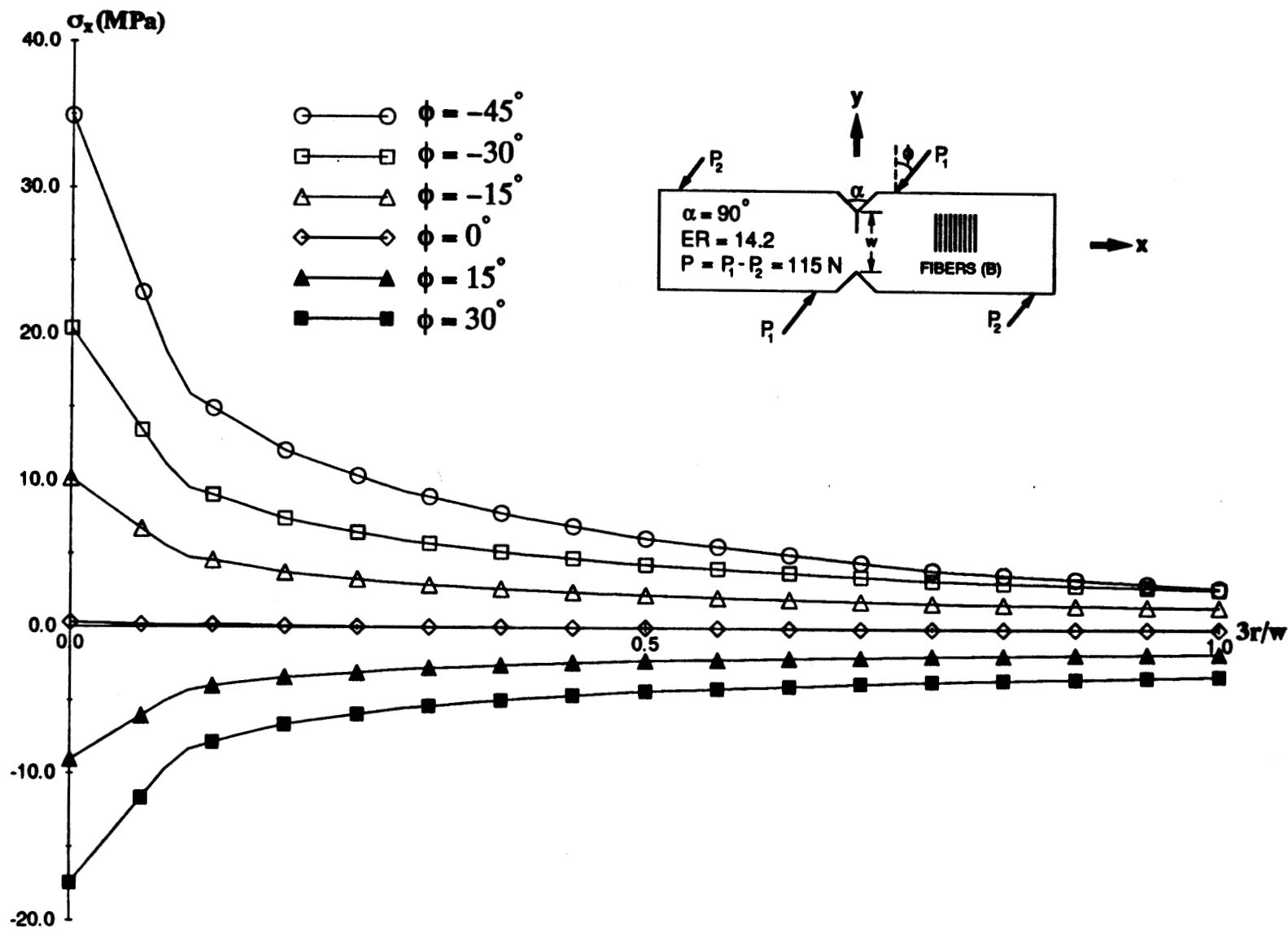
Figure 3.22 Normal stresses (σ_x) between the notch roots in orthotropic specimens (B–type) as a function of the loading angle ϕ.
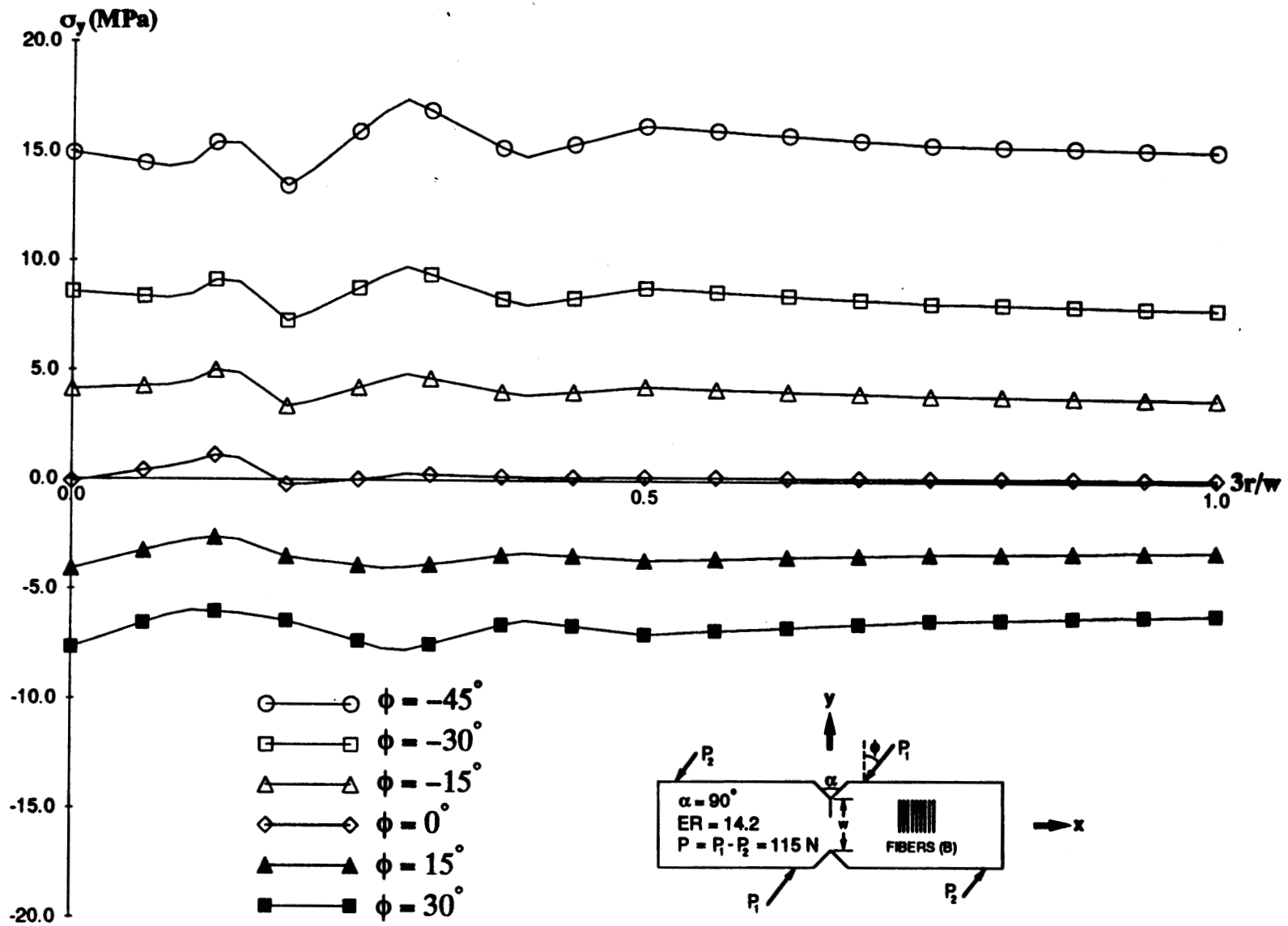
Figure 3.23 Normal stresses (σ_y) between the notch roots in orthotropic specimens (B−type) as a function of the loading angle ϕ.
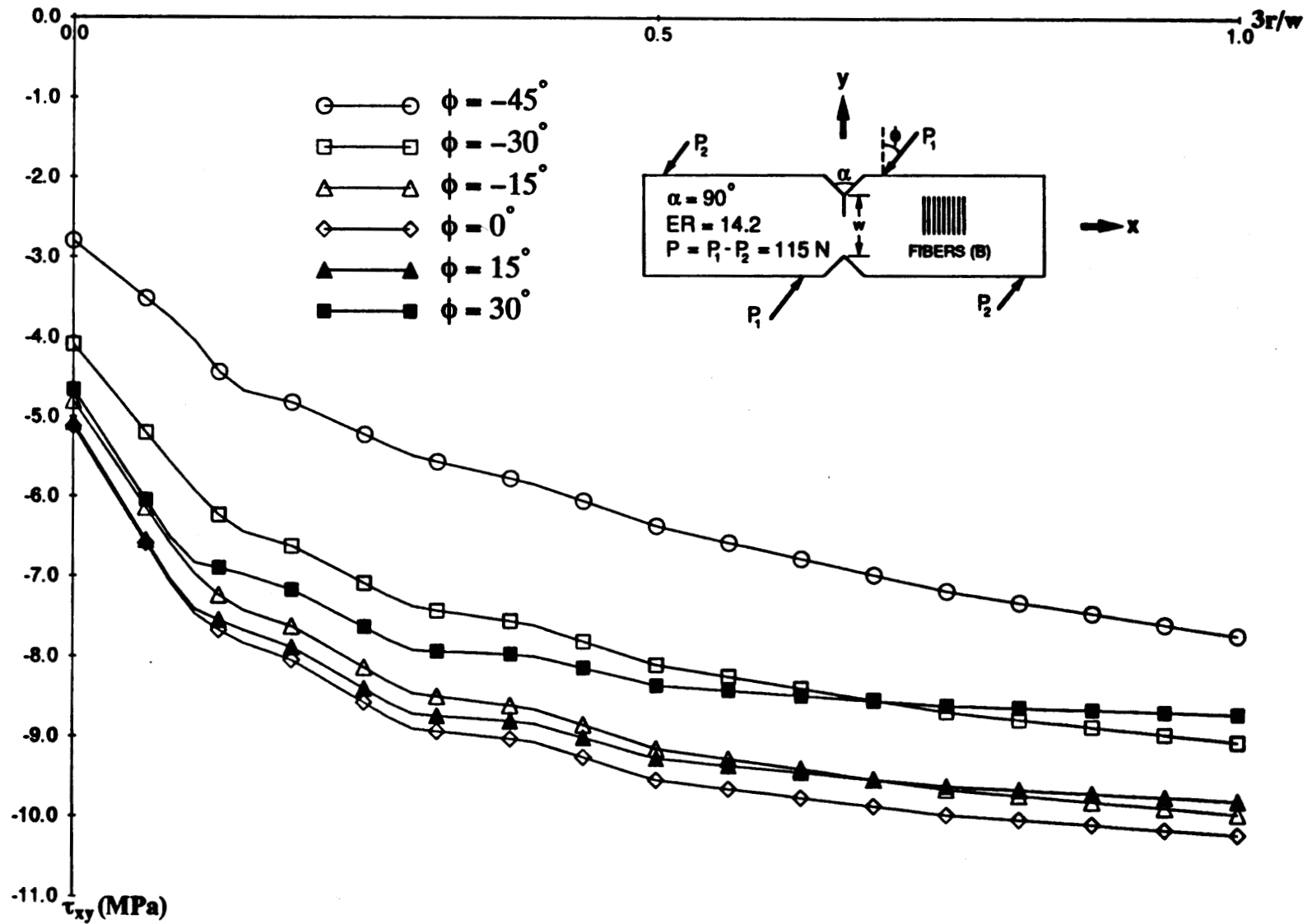
Figure 3.24 Shear stresses (τ_{xy}) between the notch roots in orthotropic specimens (B–type) as a function of the loading angle ϕ.
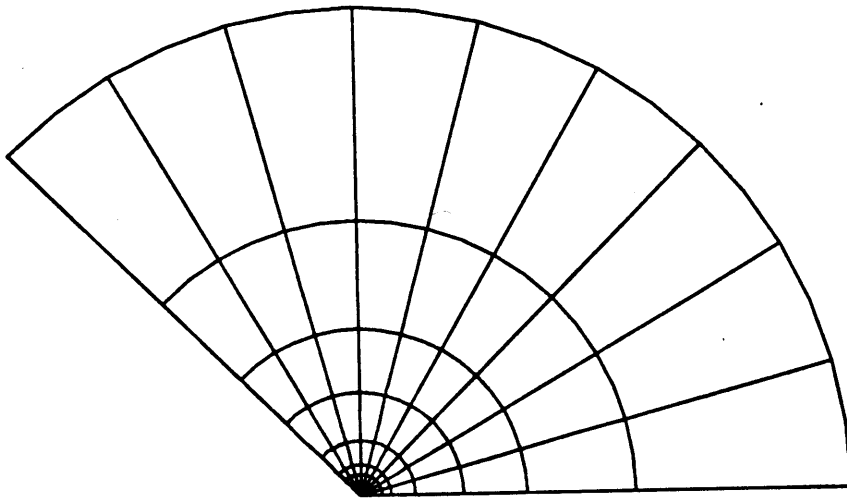
(a)
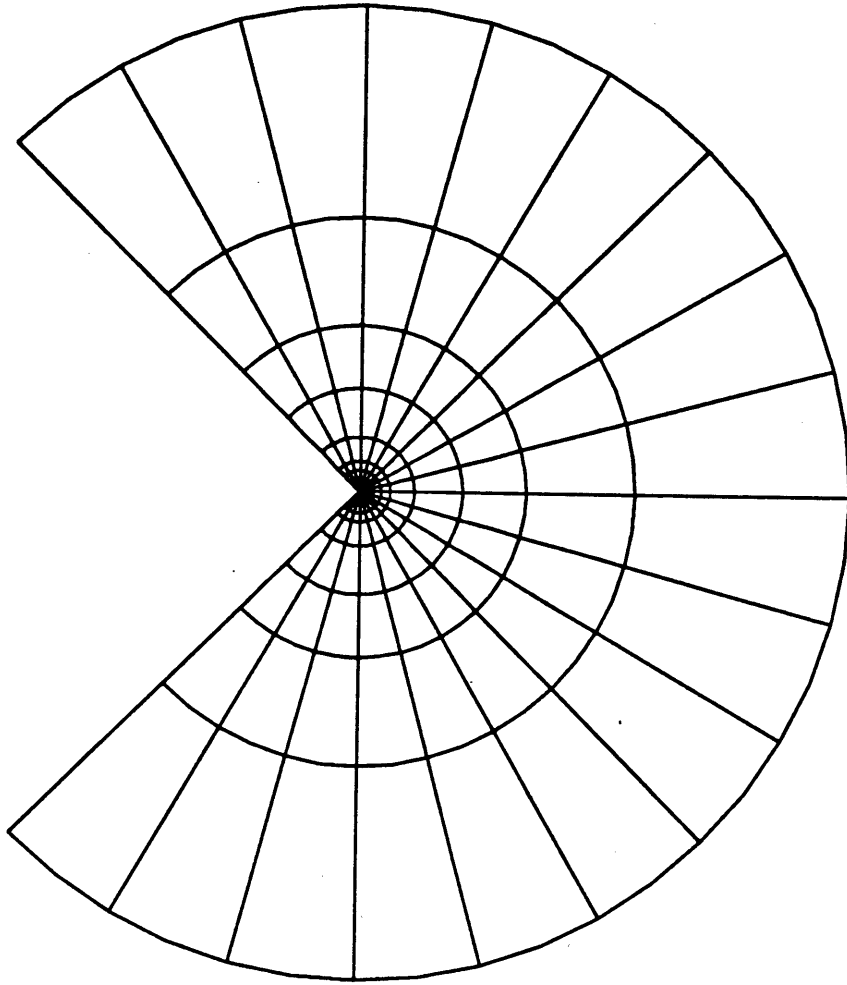
(b)

Figure 3.25 FEIM mesh. (a) Mode I or mode II loading; and (b) Mixed mode loading.
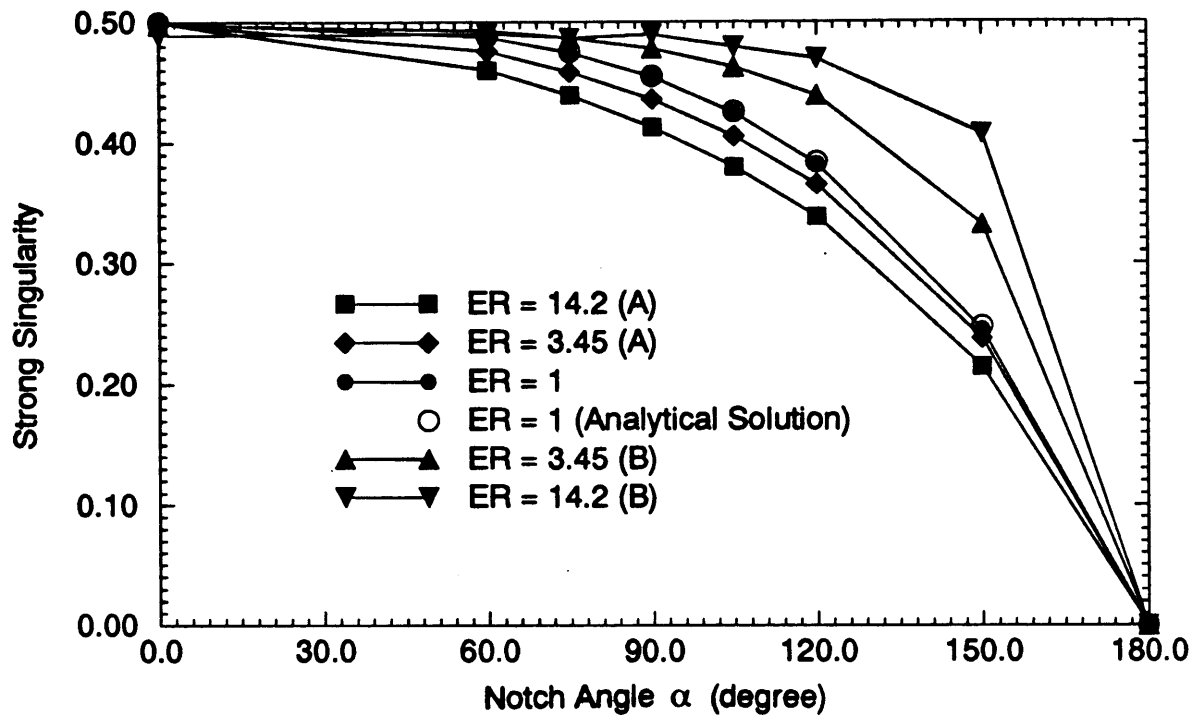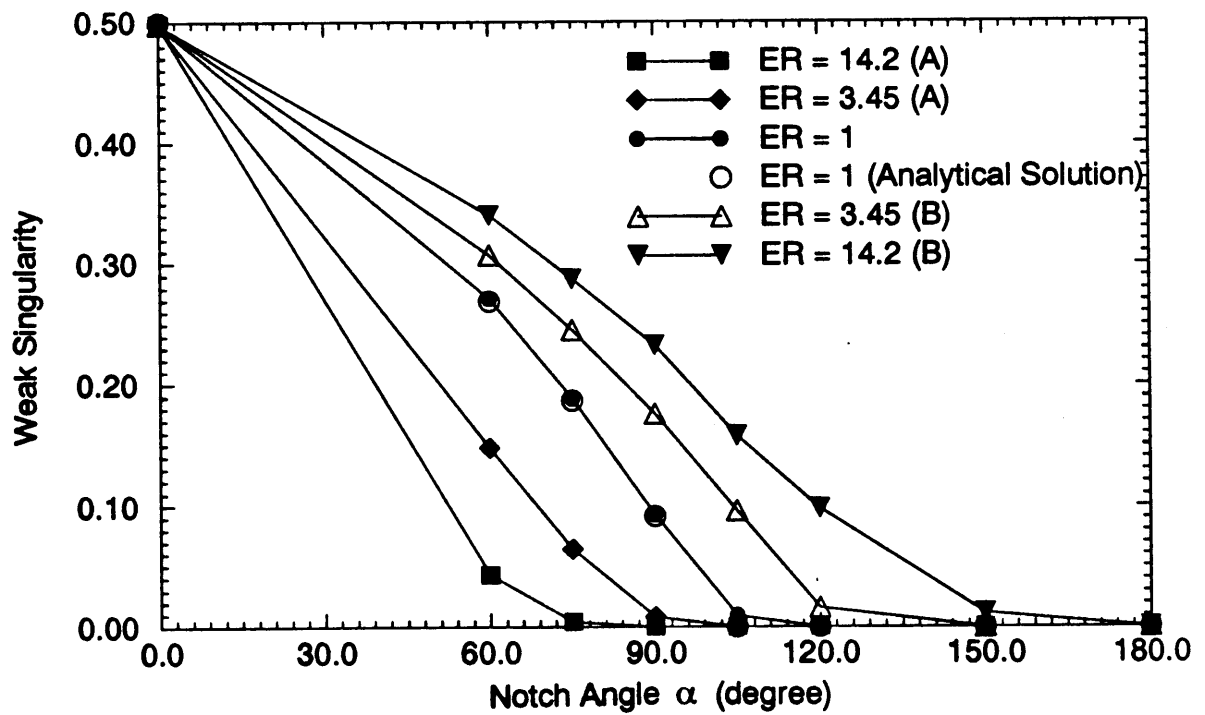
Figure 3.26 Stress singularity at sharp notches as a function of notch angle and orthotropy ratio. (a) Mode I loading; and (b) Mode II loading.
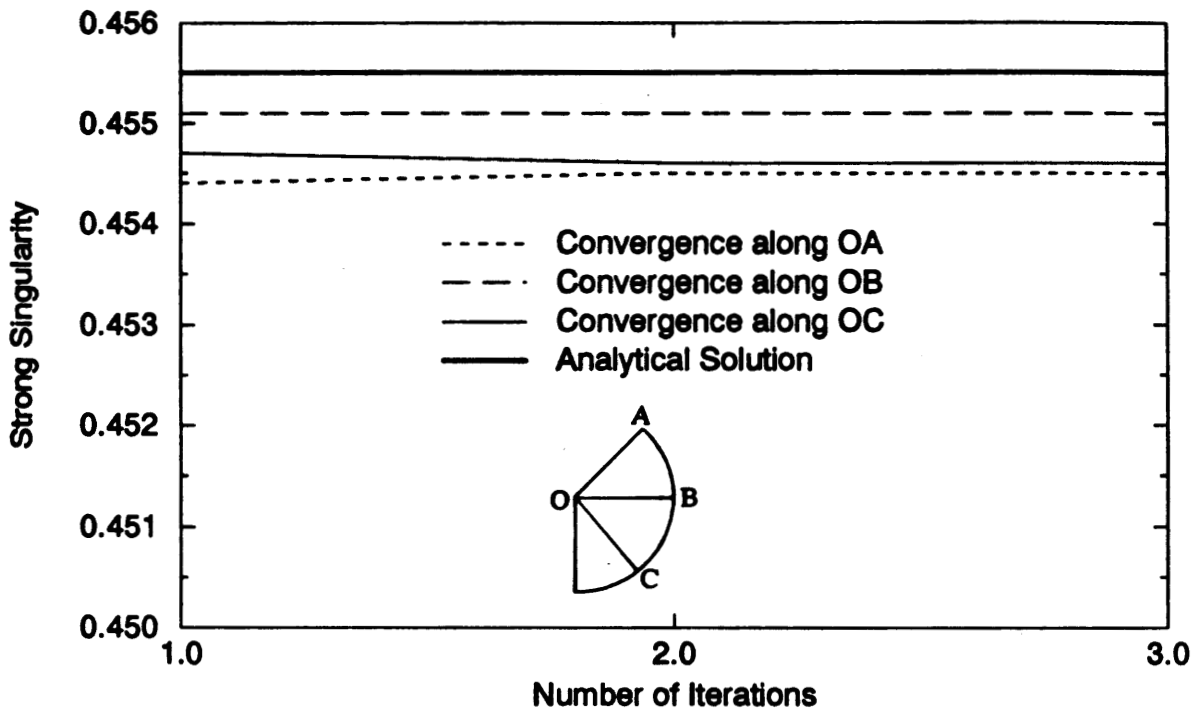
(a)
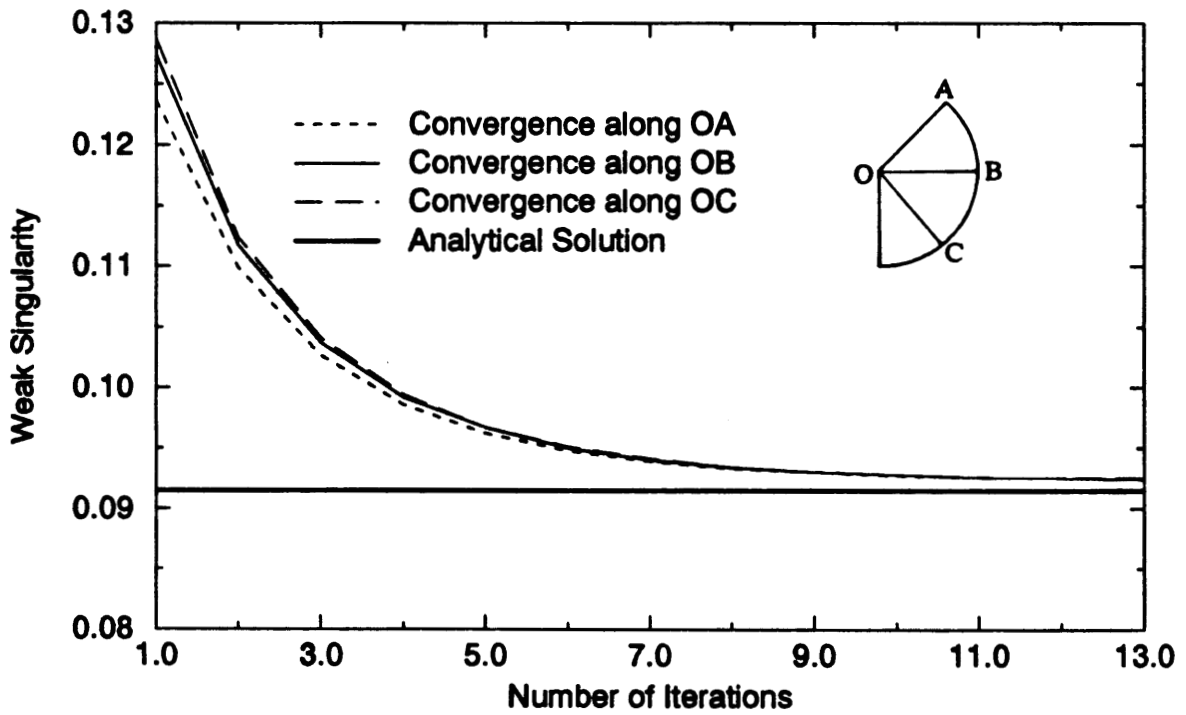
(b)

Figure 3.27 Convergence along three different rays for $\alpha = 90°$ and ER = 1. (a) Mode I loading; and (b) Mode II loading.

prescribed   displacements
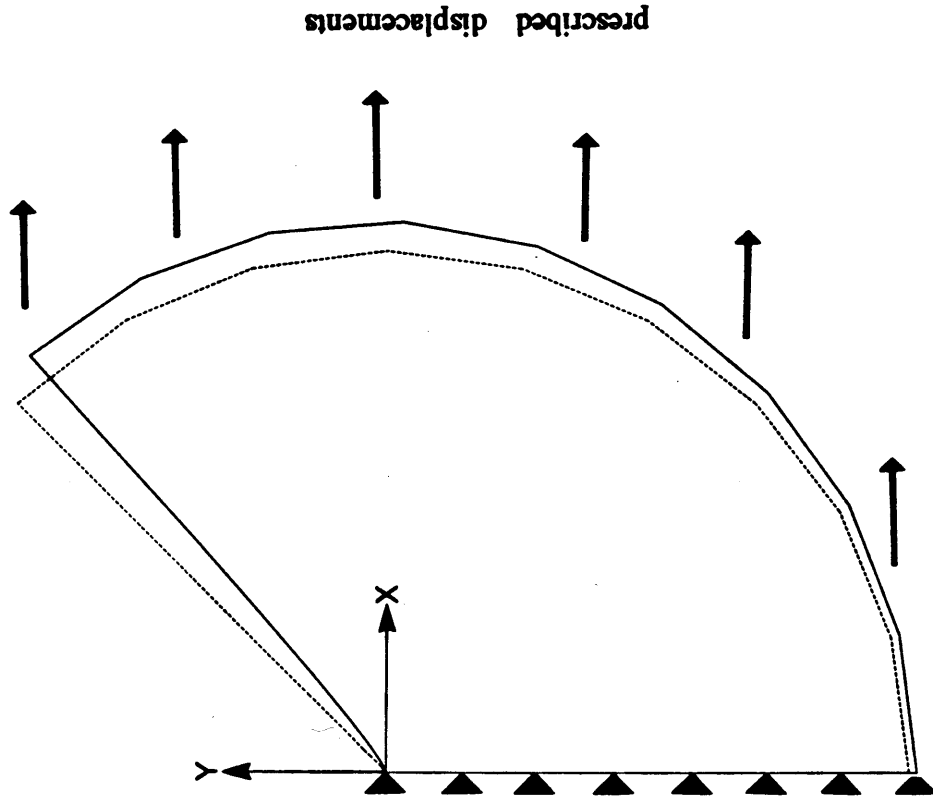
Figure 3.28 Deformed structure at convergence (2nd iteration) under mode I loading.
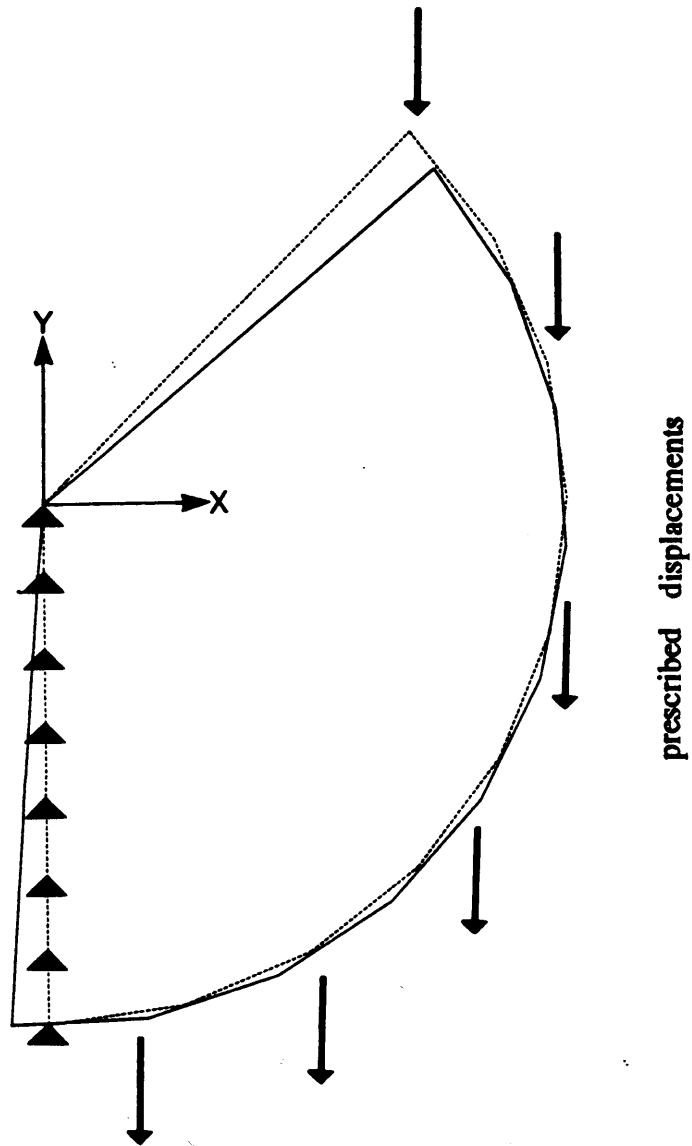
Figure 3.29 Deformed structure at convergence (13th iteration) under mode II loading.
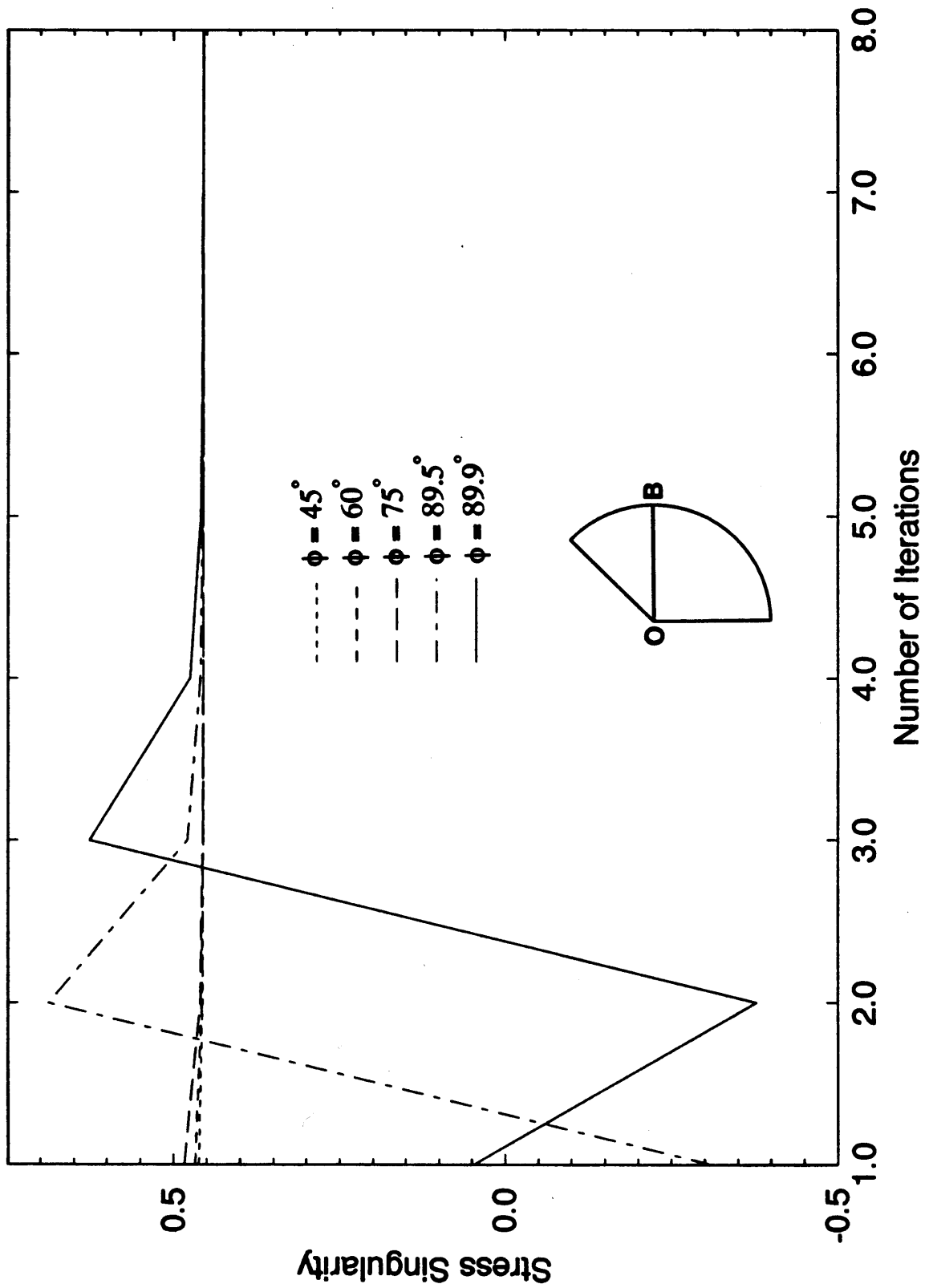
Figure 3.30 Convergence along a ray under mixed mode loadings for α = 90° and ER = 1.

(a)

(b)

prescribed displacements

prescribed displacements

$\phi = 89.9°$
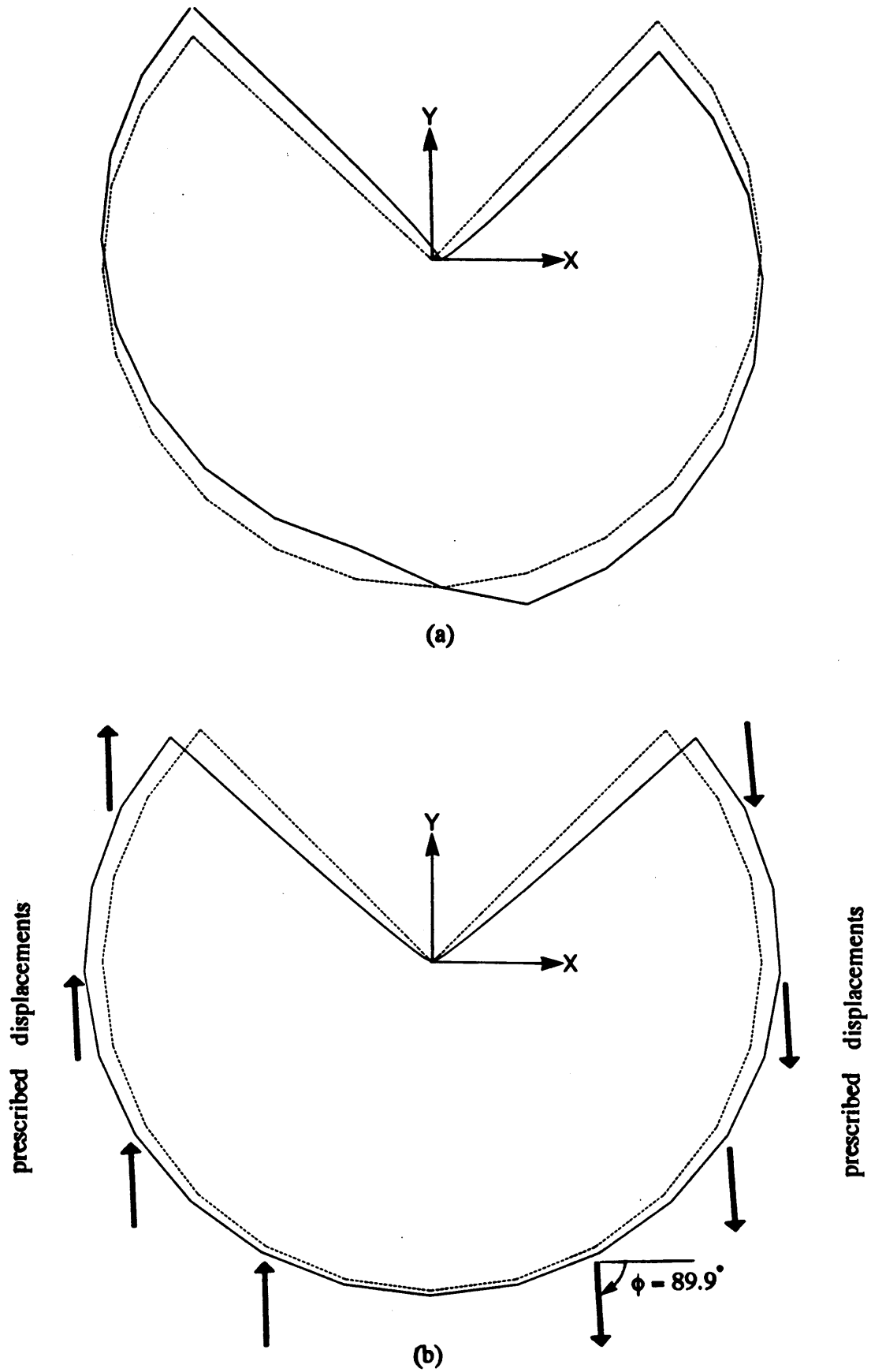
Figure 3.31 Deformed structure under mixed mode loading ($\phi = 89.9°$). (a) 0th iteration; and (b) At convergence (8th iteration).
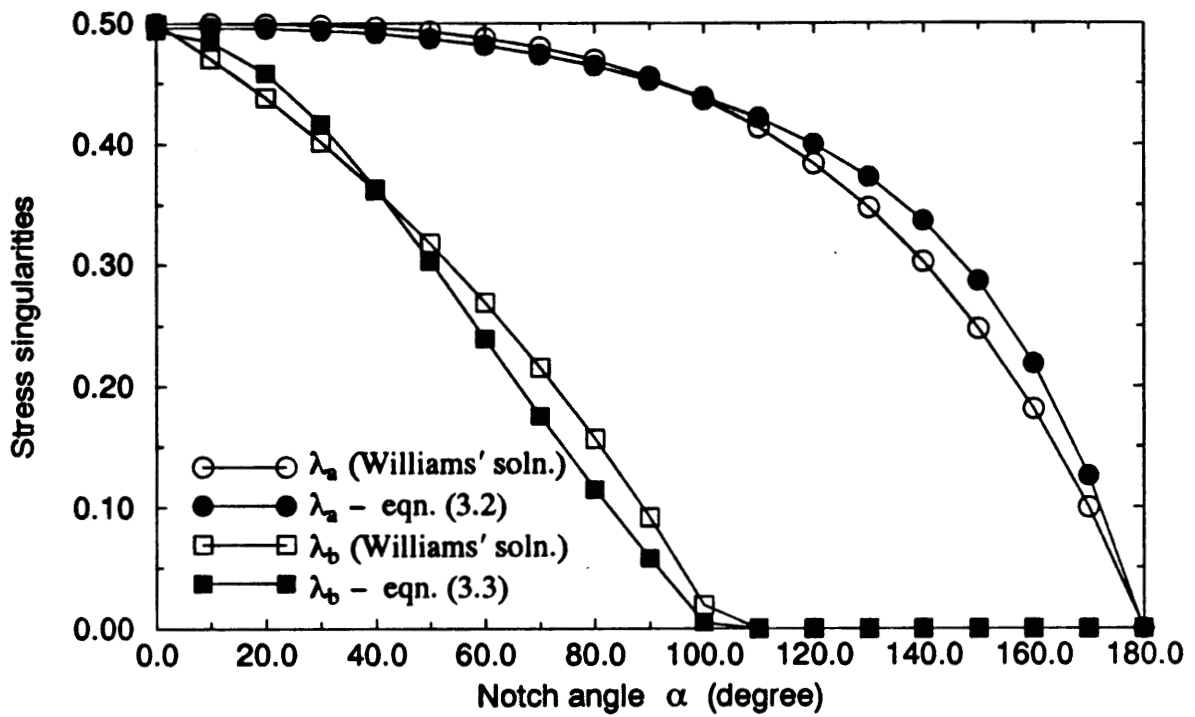
(a)
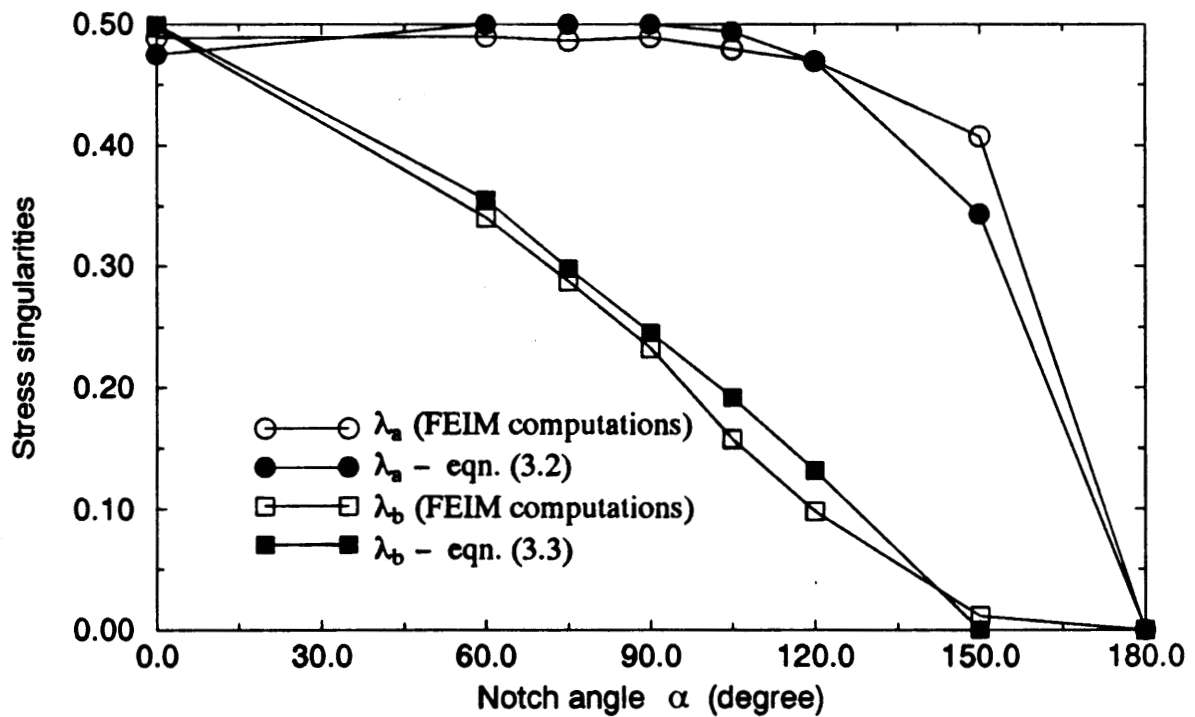
(b)

Figure 3.32 Interpolated stress singularities. (a) ER = 1; and (b) ER = 14.2.
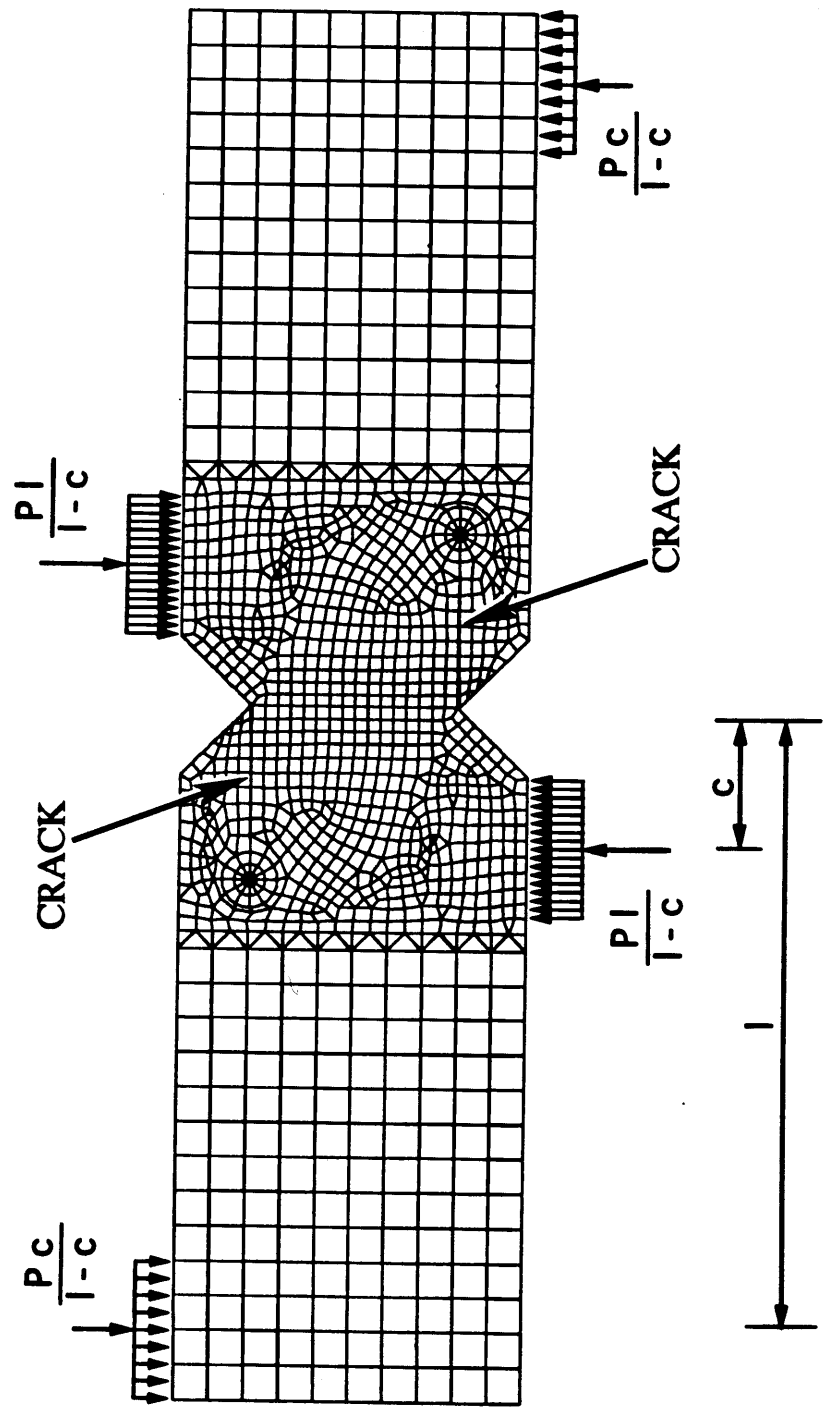
Figure 3.33 Mesh for the Iosipescu specimen with two skew-symmetric cracks ($a = 10$mm, $\phi = 0°$)

Crack
Plane
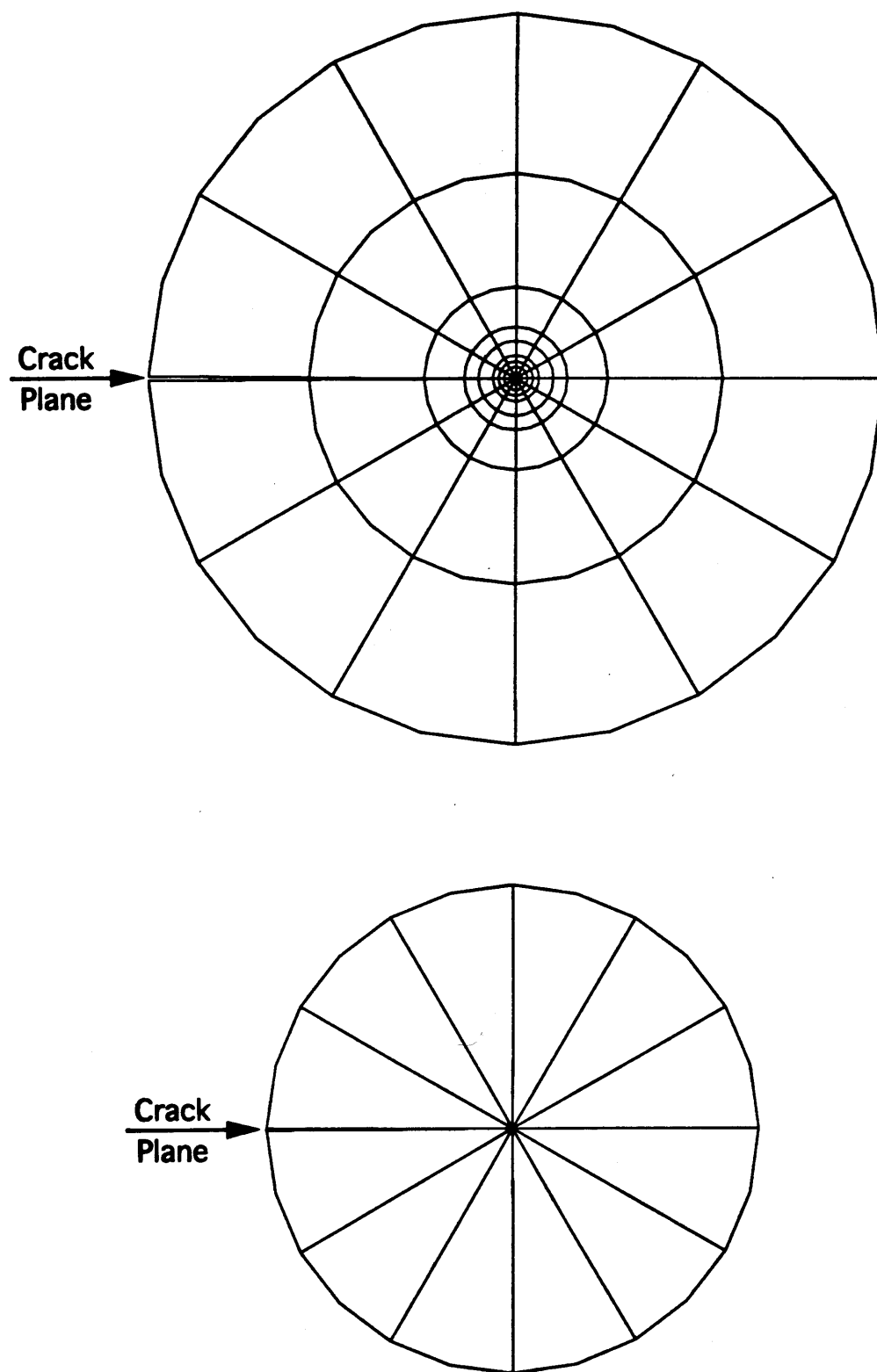
Crack
Plane

Figure 3.34 Inner mesh. (a) Fan-shaped mesh around the crack tip; and
(b) Crack-tip elements (non-singular).
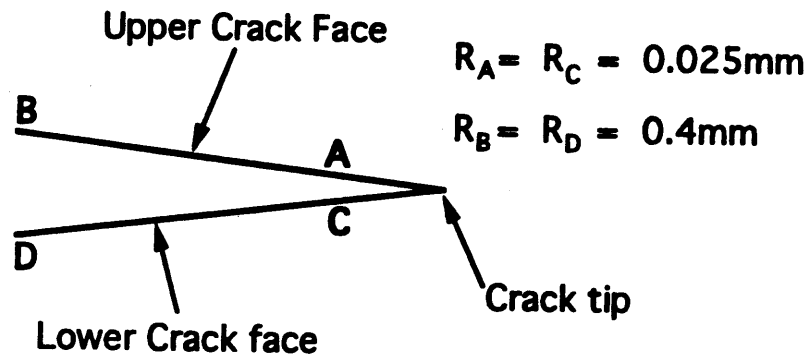
(a)
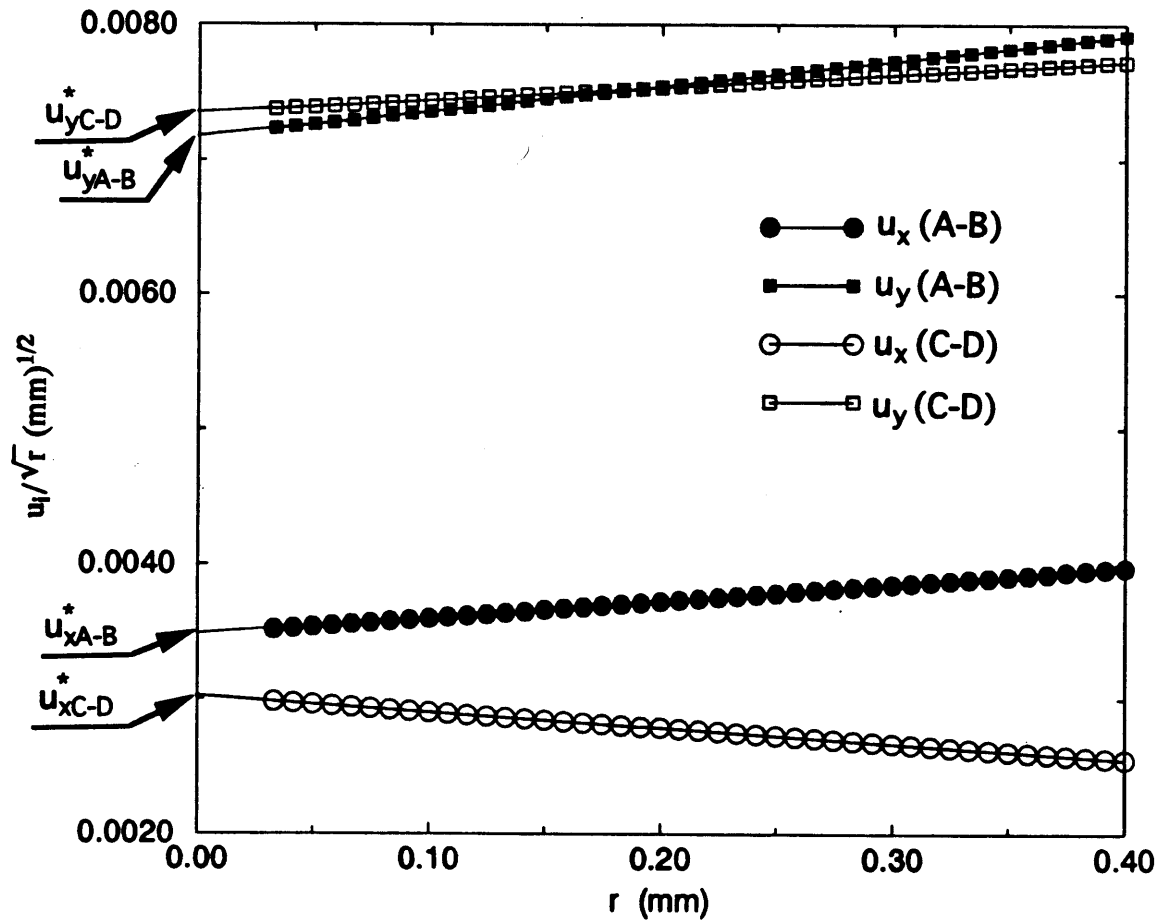
(b)

Figure 3.35 Displacement extrapolation method ($a = 10$mm, $\phi = 0°$, ER = 14.2).
(a) Regression paths A-B (upper crack face) and C-D (lower crack face); and (b) Linear regression.

Γ_2

$R_2 = 0.10mm$

Γ_1

$R_1 = 0.05mm$
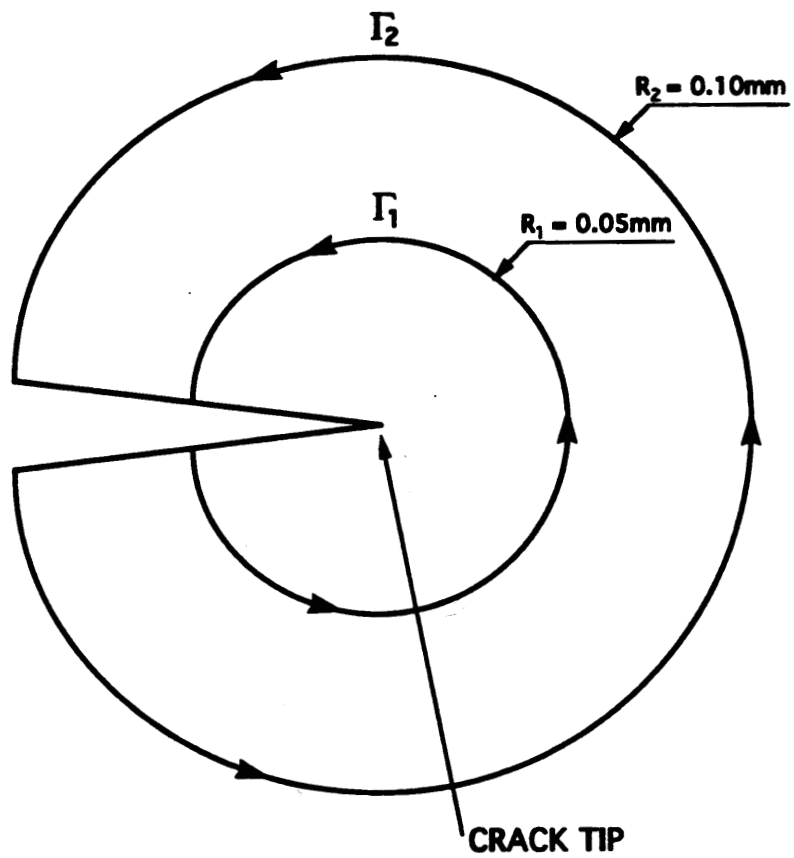
CRACK TIP

Figure 3.36 Paths for J-integral calculations.
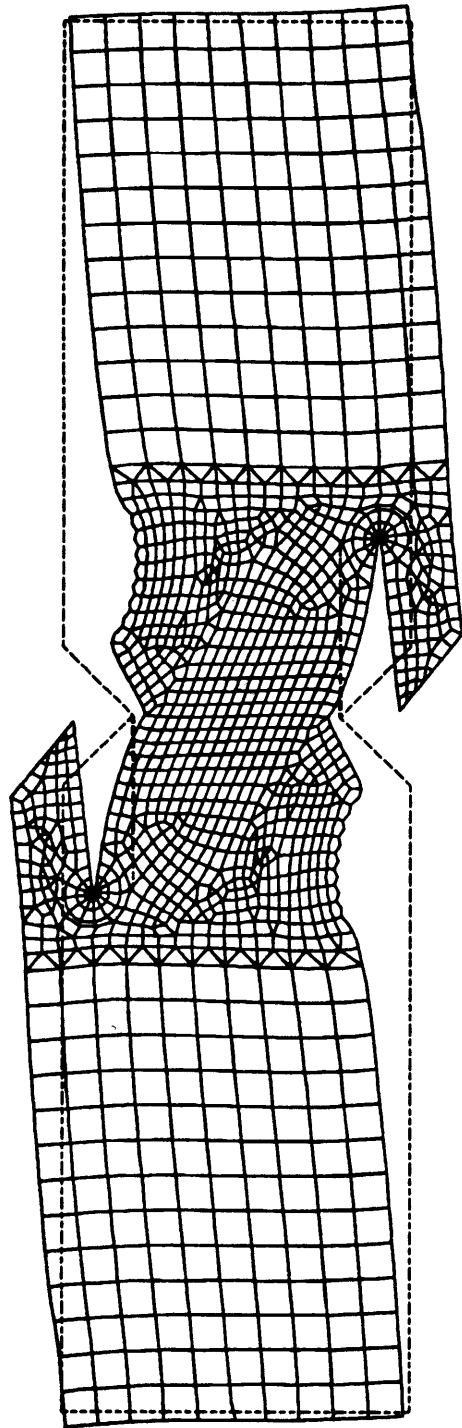
Figure 3.37 Deformed mesh for two 10mm cracks ($\phi = 0^\circ$, ER = 14.2).
(a) Full specimen; and (b) Crack-tip region.

(a)
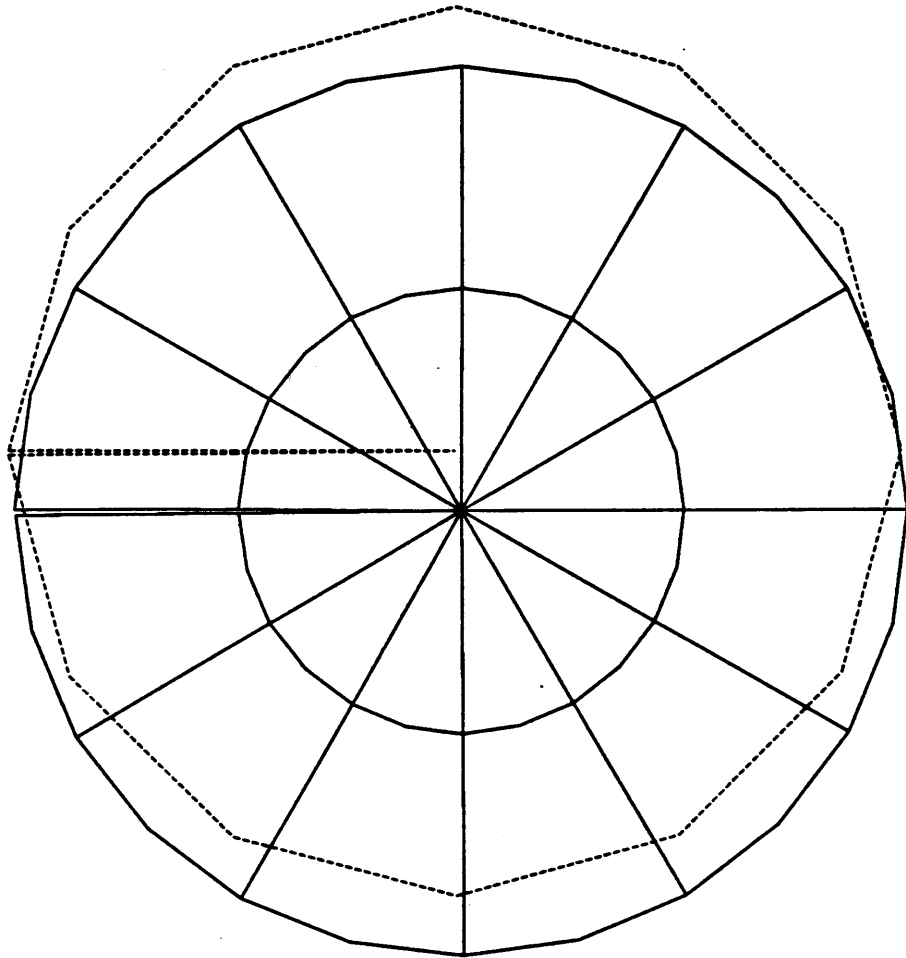
(b)
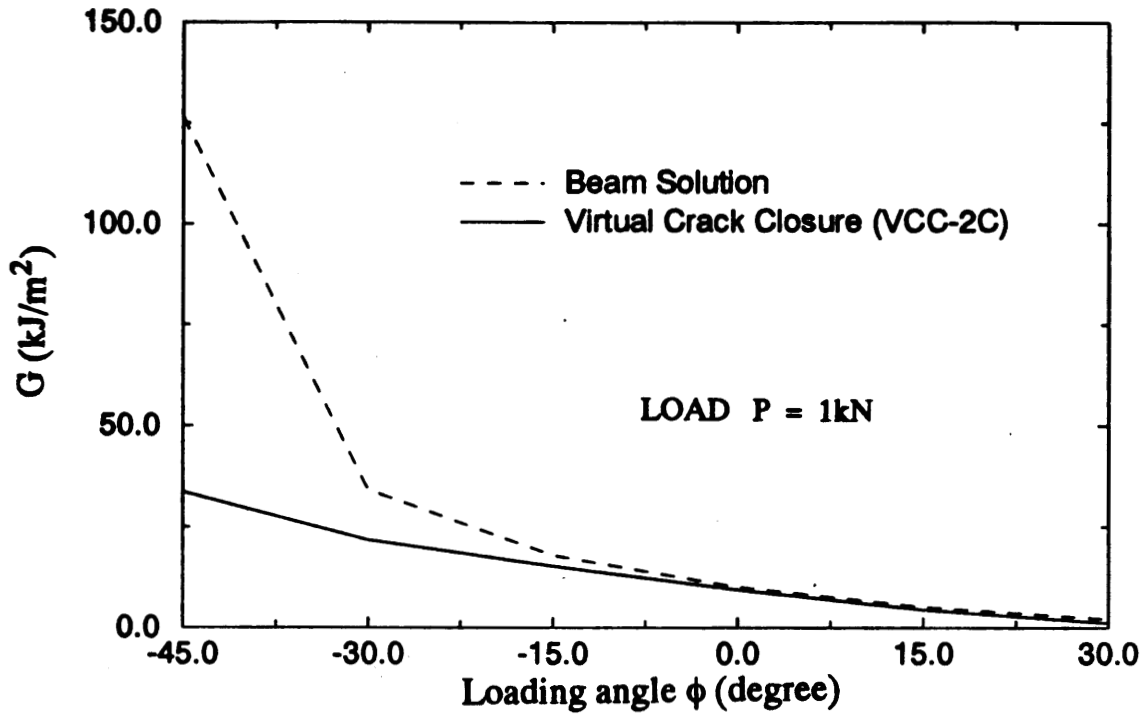
(a)
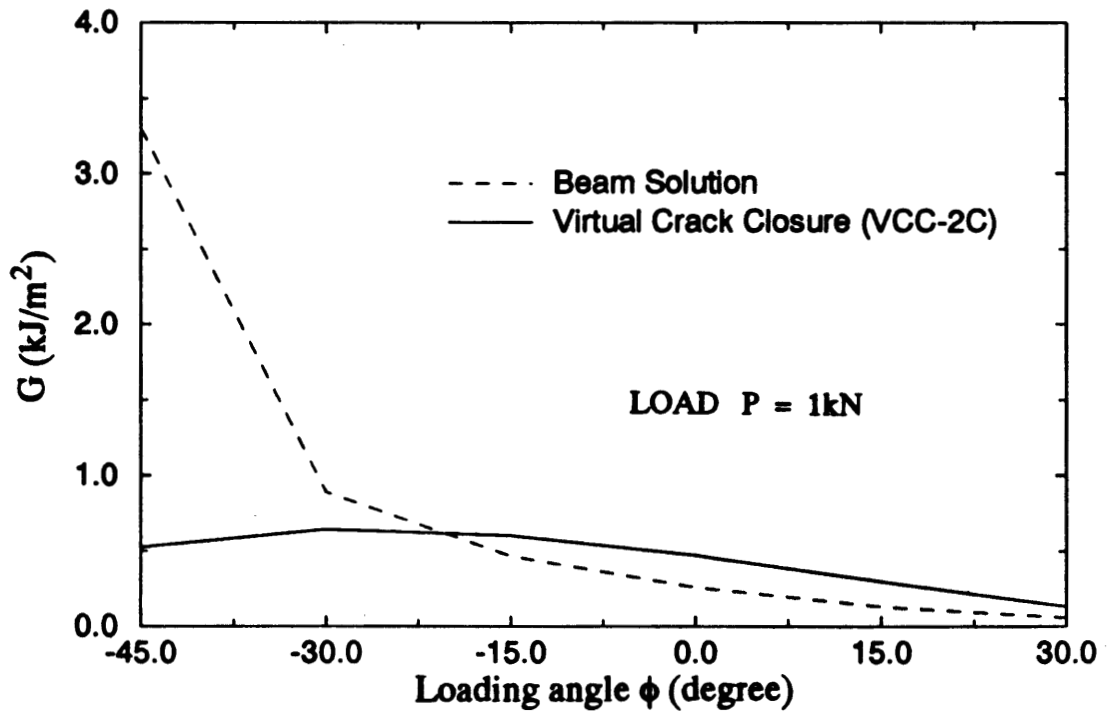
(b)

Figure 3.38 Mixed mode energy release rate G (G_I + G_{II}) as a function of loading angle ϕ for a = 10mm. (a) ER = 1; and (b) ER = 14.2 (A-type).
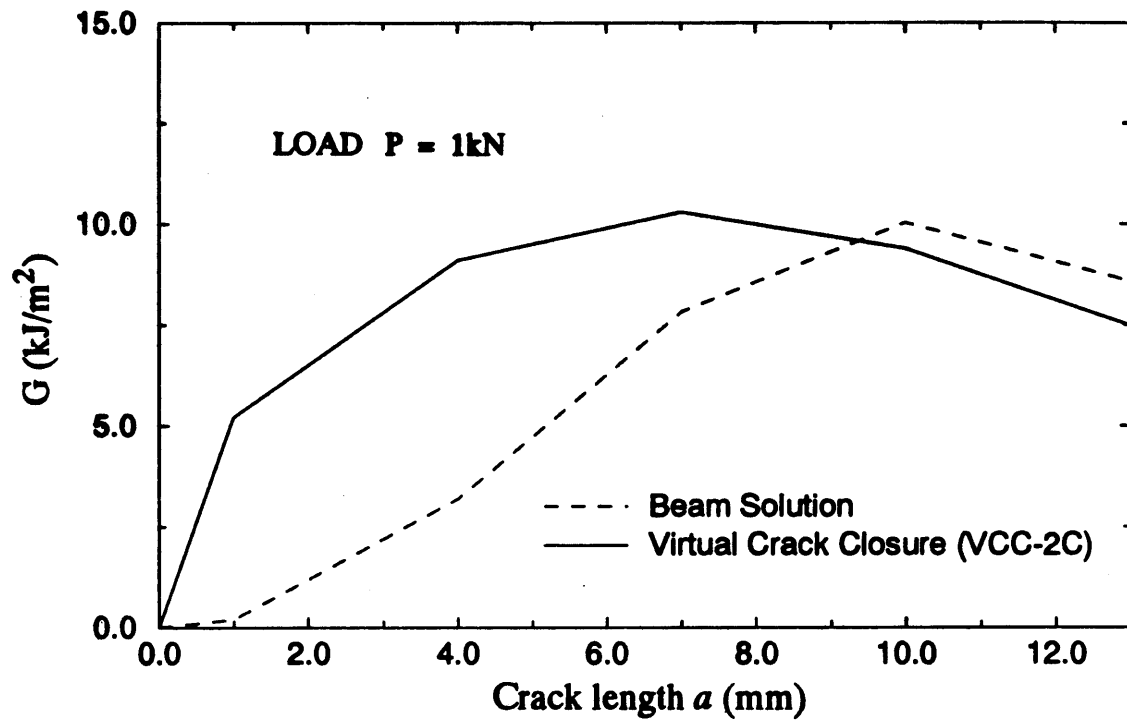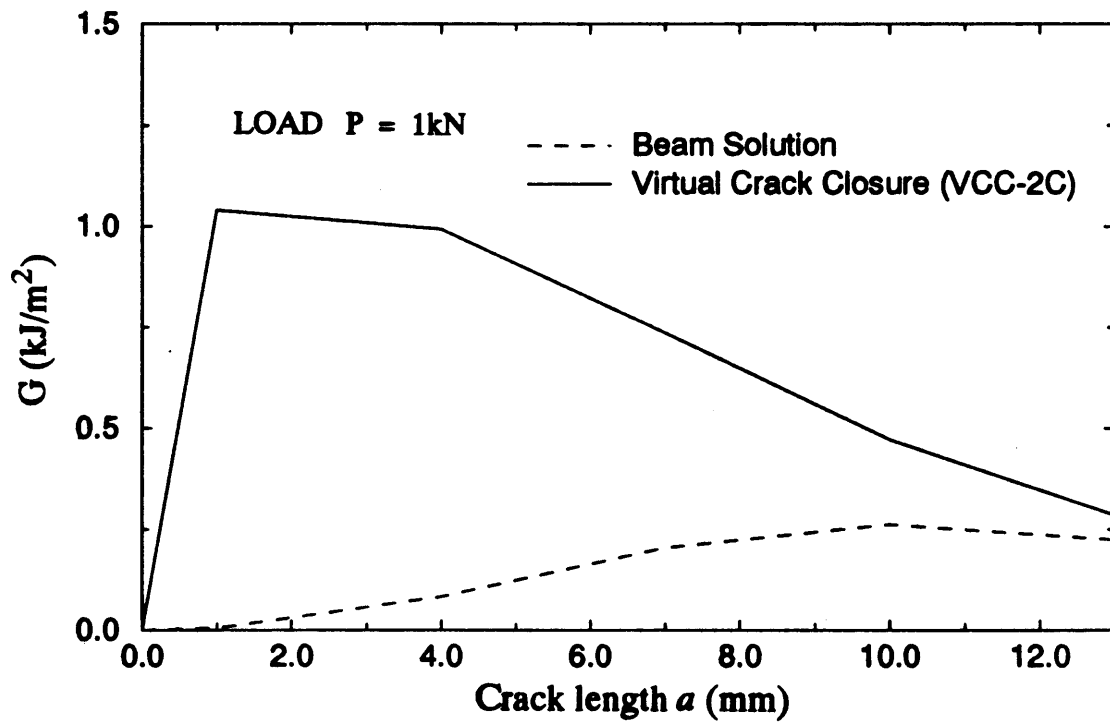
Figure 3.39 Mixed mode energy release rate G (G_I + G_{II}) as a function of crack length a for $\phi = 0°$. (a) ER = 1; and (b) ER = 14.2 (A-type).
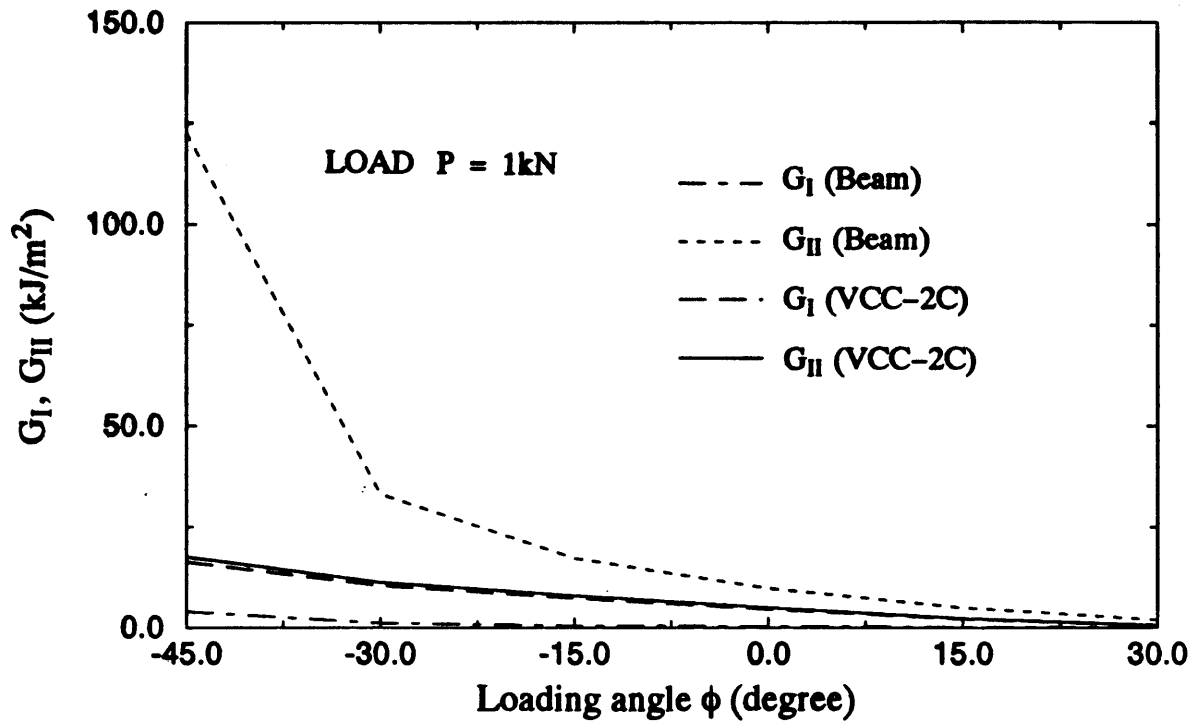
(a)
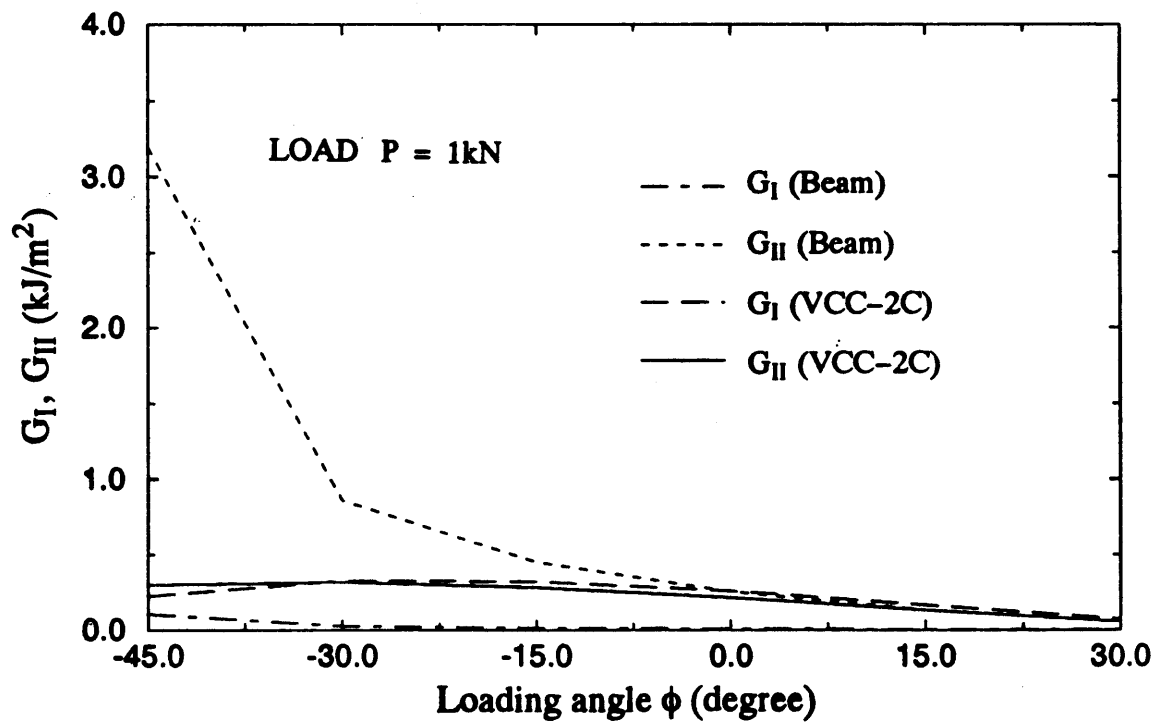
(b)

Figure 3.40 Variation of G_I and G_{II} with loading angle ϕ for $a = 10$mm. (a) ER = 1; and (b) ER = 14.2 (A-type).
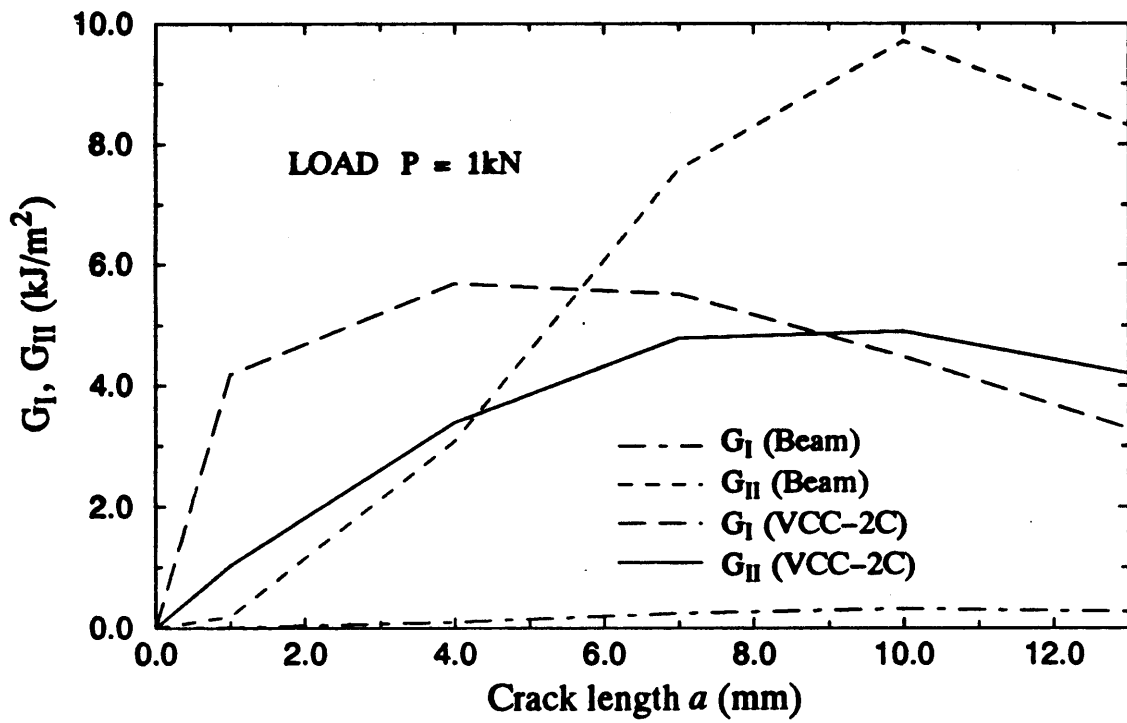
(a)
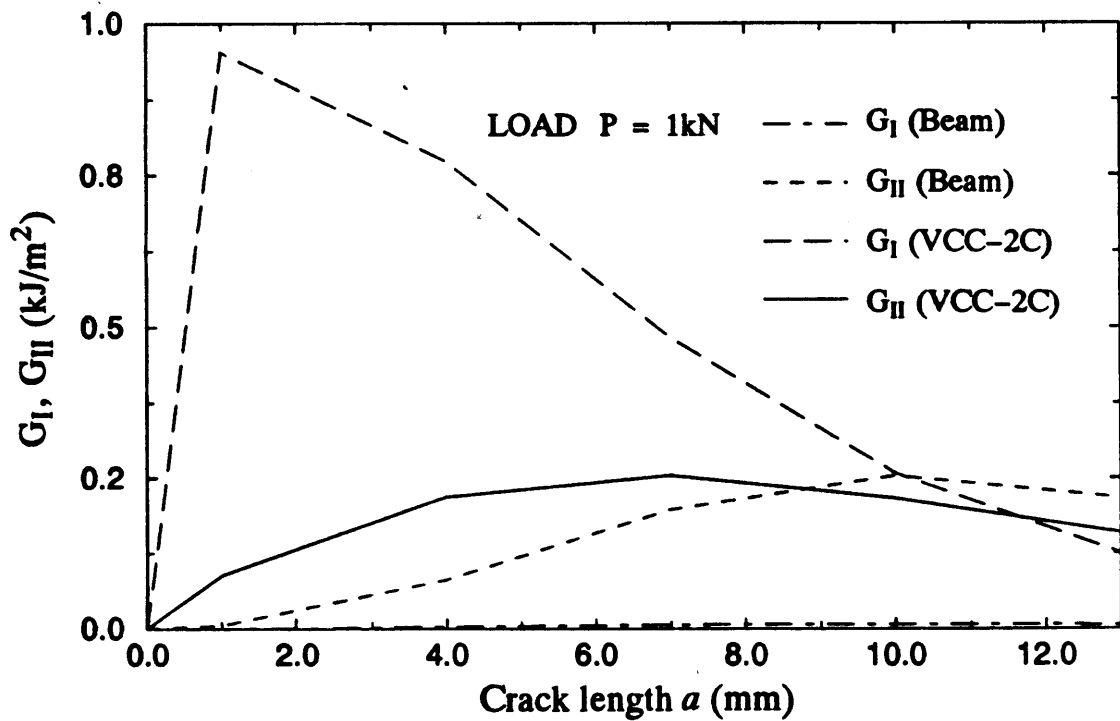
(b)

Figure 3.41 Variation of G_I and G_{II} with crack length a for $\phi = 0°$. (a) ER = 1; and (b) ER = 14.2 (A-type).

CHAPTER 4

DISCUSSIONS

4.1. Stress Distribution in Iosipescu Specimens

A linear elastic finite element analysis under generalized plane stress was performed to determine the macroscopic stress distribution in the mid-section of the Iosipescu specimen. The analysis was carried out for notch angles α in the range $60° \leq \alpha \leq 150°$ in either shear ($\phi = 0°$) or a combination of shear, transverse tension ($-\phi$) or compression ($+\phi$) loading conditions. The materials modeled in this analysis were polyester resin (isotropic), glass/polyester and carbon/epoxy unidirectional composites respectively, with orthotropy ratios ER = 1, 3.45, and 14.20 respectively.

In Figures 3.4 – 3.7, the von Mises stress contours and isochromatic fringe patterns[2,8] are presented for isotropic as well as orthotropic Iosipescu specimens. The contours for isotropic and orthotropic specimens are found to match well with the isochromatic fringe patterns. It can be seen from Figures 3.4 and 3.5 that the stress contours for ER = 1 are distributed anti-symmetrically about the notch-root axis. In Figures 3.4 and 3.5, stress concentrations near the notch root and in the vicinity of the loading points are clearly visible. In Figure 3.5, the fringe patterns and von Mises contours are shown for orthotropic Iosipescu specimens in orientations A (0-deg) and B (90-deg) respectively. As opposed to the isotropic case, in B-type unidirectional fiber composites, the maximum stress-regions are near the center of the specimen.

In Figures 3.8 – 3.10, analytical as well as numerical predictions for the stress state

at the center of Iosipescu specimens are illustrated. It is apparent from the above figures that there is a significant difference between the stresses predicted by the analytical formulae vis-à-vis those obtained from the finite element calculations. Even though the trends for at least the shear stress τ_{xy} are similar, there is a marked difference in the analytical (τ_{xy}^a) and numerical (τ_{xy}^n) values. As one would expect, the simplistic analytical approach is not sufficient to predict the stress field at the center of the Iosipescu specimen. The non-linear behavior, notch geometry, specimen dimensions, orthotropy ratio, fiber orientations and other factors need to be considered in the analytical model for accurate results.

In Figures 3.11 and 3.12 the variation of the normalized stress along the notch-root axis is presented as a function of the notch angle α. For the isotropic Iosipescu specimen under pure shear ($\phi = 0°$), the normalized shear stress at the notch root $\tau_{xy}^{norm} > 1$ for all $\alpha \leq 90°$, while $\tau_{xy}^{norm} < 1$ for all $\alpha \geq 105°$. In case of the orthotropic specimen (A-type) with ER = 14.2, $\tau_{xy}^{norm} > 1$ for all $\alpha \leq 120°$, while $\tau_{xy}^{norm} < 1$ for $\alpha \geq 150°$.

The shear stress along the notch-root axis is plotted in Figure 3.13, while the variation of the shear stress concentration K_t with notch-root element size is shown in Figure 3.14 ($\alpha = 90°$, ER = 1, $\phi = 0°$). It can be seen from Figures 3.13 and 3.14 that the stress concentration factor K_t increases with decreasing notch-root element size. Similar trends in the shear stress concentration were also seen for ER = 3.45 (A-type) and ER = 14.2 (A-type). The shear stress concentration K_t as a function of the notch-root element size is presented in Table 3.2; the same data is plotted in Figure 3.15. Kumosa and Hull[7] have proposed the relation $K_t = A (ER)^{1/4}$ (refer equation (2.2) in Section 2.1) for the variation of the shear stress concentration with fiber orientation. It can be clearly seen from Figure 3.15 that the shear stress concentration at the notch-root is a function of the

notch-root element size. The slopes of the lines increase with decreasing notch-root element sizes, and thus the above mentioned relation is inapplicable at the notch-root. All the above findings clearly indicate that the stress field is singular at the notch-root in isotropic as well as orthotropic materials.

The stress distribution around the notch-root region was studied under mixed mode loading conditions for $\alpha = 90°$ (Figures 3.16 – 3.24). The stresses were calculated along the x- and y-directions. A complex state of stress, with both normal and shear stresses are present around the notch-root region. An important feature of the normal stresses (σ_x and σ_y) that can be seen for all $\phi \geq 0°$ in Figures 3.16 and 3.17 is the changing of sign as one traverses across the vertical center-line of the specimen. When the loading changes from pure shear ($\phi = 0°$) to shear-tension ($-\phi$), the normal stresses tend to become tensile on either side of the notch. In Figure 3.19, the longitudinal normal stress σ_x for the orthotropic specimen (A-type) shows a gradual transition from tension to compression as the loading changes from $-\phi$ (shear-tension) to $+\phi$ (shear-compression). However, the transverse normal stress (σ_y) shows a distinct change in sign across the center-line of the specimen. For all ϕ, σ_y is tensile on the opposite side of the loading points, while it is compressive on the same side of the loading points for orthotropic specimens (A-type). In Figures 3.22 and 3.23, the normal stresses for the orthotropic specimen (B-type) show marked differences in comparison to ER = 1 or ER = 14.2 (A-type). Both the normal stresses for the B-type specimen show an appreciable rate of change from tension to compression as the loading changes from $-\phi$ (shear-tension) to $+\phi$ (shear-compression). From Figures 3.20 and 3.23, the respective transverse normal stresses for the A-type and B-type orthotropic specimens can be compared. Under pure shear ($\phi = 0°$) there exists a small transverse-tensile stress at the notch root for the B-type

specimen (Figure 3.23), while in case of the A-type specimen, the stress is compressive in nature (Figure 3.20). This difference is responsible for the lower shear strengths recorded in orthotropic Iosipescu specimens tested in the B-type fiber orientation. This observation has been found to be true from earlier experimental as well as numerical studies on the Iosipescu shear test. [6-8]

4.2. Singular Stress Fields at Sharp Notches

The Finite Element Iterative Method was applied to sharp notches for evaluating the singular power at the notch root. The stress singularity was studied as a function of the notch angle α, and the orthotropy ratio ER. The simplicity and accuracy of the FEIM approach was demonstrated in the determination of the stress singularity at the notch root, in either isotropic or orthotropic materials.

The analytical solution by Williams[50] indicates that there are two stress singularities at the notch root: the strong singularity λ_a, and the weak singularity λ_b. The FEIM results always converges to the dominant singularity at the notch root, when multiple singular powers exist. It can be seen from the data presented in Table 3.3 that the numerically evaluated stress singularity at the notch root under mode I loading always converges to λ_a. The numerical results for the isotropic case (ER = 1) are in excellent agreement with the analytical solution proposed by Williams. [50] As the notch angle is decreased, the singular power increases, attaining a maximum value of 0.5 for $\alpha = 0°$, which is the limiting case when a notch becomes a crack. The same trend can be seen in Figure 3.26a with increasing ER (orientation A), though the rate of increase in the stress singularity is significantly greater. In orientation B, the stress singularity values are lower than those computed for the isotropic case. In all cases, two or three iterations

were sufficient for convergence. The few iterations needed for convergence were due to two factors: the presence of a strong singular field λ_a, and a large region dominated by it in comparison to the λ_b singular field.

The numerically evaluated stress singularity under mode II loading always converges to λ_b, which implies that the dominant singular power at the notch root is the weak singularity. Even though λ_a still exists at the notch root, the intensity of the λ_a field is zero, and hence the asymptotic term involving λ_a makes no contribution to the stress field in the immediate vicinity of the notch tip. **There exists a critical angle above which λ_b vanishes under shear loading conditions (see Table 3.4).** For the isotropic case, α_{cr} is approximately $103°$. This suggests that the stress field at the notch root is non-singular in the above case. Moreover, the critical angle α_{cr} varies with the orthotropy ratio ER. With increasing ER, α_{cr} increases in orientation A, but decreases in orientation B, with respect to the isotropic case. The above findings can explain some of the finite element results obtained in regard to the shear stress distribution near the notch root in isotropic and orthotropic Iosipescu specimens under pure shear (Figures 3.11 and 3.12). **The numerically computed critical angle α_{cr} for ER = 1 and ER = 14.2 (A-type) are approximately $105°$ and $150°$ respectively.** Since the stress fields are non-singular for $\alpha > \alpha_{cr}$, one would expect the normalized shear stress (τ_{xy}^{norm}) to be less than 1 for all notch angles greater than α_{cr}. These very results were obtained in Section 3.1.1.3, and the discussions that followed on the same in Section 4.1 corroborate the above inferences drawn from the stress singularity computations.

The rate of convergence under mode II loading was observed to be much slower than that for mode I loading. This suggests, apart from the fact that the singular power λ_b is much weaker than λ_a, that the region dominated by the λ_b singular stress field is

also much smaller than that of the λ_a stress field.

The mathematical and numerical basis for the convergence to the weak singularity λ_b under mode II loading needs to be elaborated. The mathematical formulation for the case when there are two terms in the asymptotic expansion of the singular field is outlined in Section 2.3.4. The numerical scheme to evaluate both the singularities (strong and weak singularities in this study) is also discussed. The displacement field at the nth iteration $\{u_{Rb}^n\}$ can be represented as a linear sum of the complete set of eigenfunctions. Let $\mathbf{u}_a$ and $\mathbf{u}_b$ be the eigenvectors corresponding to λ_a and λ_b respectively. At convergence, only the dominant eigenvector $\mathbf{u}_a$ is present in the expansion. Since the system is self-adjoint, and the transfer matrix [T] is real (real λ), the eigenvectors are orthogonal ($\mathbf{u}_a^\Gamma \cdot \mathbf{u}_b = 0$). Hence, if the trial vector in the numerical analysis is taken to be orthogonal to $\mathbf{u}_a$, the second term in the asymptotic expansion (λ_b in this study) can be evaluated. [70] In a mode I analysis, λ_a was obtained. Since the initial displacement vector for a mode II analysis is orthogonal to that in a mode I analysis, convergence to λ_b is realized in a mode II analysis.

Under mixed mode loading, convergence was always to the strong singularity λ_a, irrespective of the loading angle ϕ. This suggests that the dominant singular power at the notch root for any mixed mode loading is always λ_a. Since the weak singularity λ_b still exists at the notch root, the stress state at the notch root is always a biaxial one. This indicates that failure at the notch root is always under mixed mode stress conditions. It is apparent from Figure 3.30 that with increasing ϕ, the number of iterations for convergence increases. Qualitatively, this indicates that the region dominated by the λ_a singular stress field decreases as the loading changes from mixed mode to mode II.

Interpolation formulas for λ_a and λ_b as a function of the notch angle α and orthotropy ratio ER were proposed. In Figure 3.32a, the interpolated values obtained for ER = 1 from equations (3.2) and (3.3) are shown along with the results from Williams' solution, [50] while in Figure 3.32b, the interpolated values for ER = 14.2 (A-type) are compared to the numerically computed stress singularities (refer Tables 3.3 and 3.4). The stress singularity predictions by equations (3.2) and (3.3) were found to be within 10% of the numerically computed values for the entire range of α and ER considered in this study. Hence, the interpolation formulas can be viewed as a simple and adequate tool for an engineer who does not need high-precision in the singularity-estimations.

4.3. Mixed Mode Fracture in Iosipescu Specimens

A linear elastic finite element analysis under generalized plane stress was performed to compute the energy release rates (G_I, G_{II}, G) for two skew-symmetric splits along the fiber direction in Iosipescu specimens. The computations were carried out for specimens with notch angle $\alpha = 90°$ in either shear ($\phi = 0°$) or a combination of shear, transverse tension ($-\phi$) or compression ($+\phi$). The energy release rates were evaluated for crack lengths a from 1mm to 13mm in isotropic as well as orthotropic Iosipescu specimens (A-type).

In order to validate the VCC-schemes for orthotropic fracture analysis, the benchmark test of an edge-crack in an orthotropic strip in tension was considered; the numerically and analytically[78] determined stress intensity factors are listed in Appendix D (Tables D.1 – D.3). The numerical and reference solution results are in good agreement. It can be seen that, for orthotropic fracture analysis, a crack-tip element size of the order of 2% or less of the crack length gives accurate results, with the VCC-2C method giving

the best results among the numerical techniques used in this study. The above observation of VCC-2C being more accurate than the VCC-1C approach is expected, since the 2C-approach is applicable for finite crack extensions $\Delta a >> 0$, while the 1C-scheme is strictly exact only in the limit $\Delta a \to 0$. In contrast to the VCC-schemes, the displacement method results are less accurate, and are also a stronger function of the crack-tip element size. Since only two values from the finite element calculations (u_B and u_C – Figure 2.8) are needed for the displacement method, it is by far the easiest to apply. However, it leads to the least accurate results, a finding which is supported by other studies too. [43,44]

In Table 3.7, the energy release rates obtained in orthotropic (A-type) Iosipescu specimens by the displacement method – equation (2.11) are compared to the VCC-2C scheme. The Iosipescu test loading configuration is rather unusual in the sense that the upper crack face is stressed, while the lower one is unstressed (Figure 4.1). Hence, in a mixed mode fracture analysis of the Iosipescu specimen, it is likely that the G values obtained from the upper and lower crack faces will differ. It can be seen from Table 3.7 that there is a significant difference in the G values computed from the upper and lower crack faces. The displacement method results from either crack face or even their average are in poor agreement with the VCC-2C results for the orthotropic composite specimen. Kumosa and Hull[7] used the average value of the corner-node displacements in their orthotropic fracture analysis of the Iosipescu specimen under pure shear ($\phi = 0°$). The energy release rates reported in their study are erroneous; Buchholz et al. [26] have subsequently correctly recalculated the G values using the virtual crack closure technique. **The above findings indicate that the stress intensity factors obtained by considering only two nodal displacements in the mixed mode orthotropic fracture analysis of the Iosipescu specimen are fraught with inaccuracies.**

In Appendix E, the detailed listing of the energy release rate computations for isotropic as well as orthotropic (A-type) fracture analyses are presented. Due to the poor results of the displacement method for orthotropic (A-type) Iosipescu specimens, a linear regression (displacement extrapolation method) of the displacements along either crack face (Figure 3.35a) was performed; the results are listed in Table E.4. For isotropic specimens, all the numerical estimates match very well (Tables E.1 and E.2); however, for orthotropic (A-type) fracture analysis, there is a marked difference in the G values obtained from the energy methods (VCC) vis-à-vis the displacement extrapolation technique. The results obtained from the VCC-1C scheme are within 2% of those from the VCC-2C method; however, the results from the displacement extrapolation vary as much as 10 to 20% from the VCC-2C results. In order to facilitate the discussions for this part, some of the results listed in Tables E.3 and E.4 are reproduced in Table 4.1. From Table 4.1, a direct comparison of the results obtained from the dispacement extrapolation method and the VCC-2C scheme can be made. It can be seen that even in case of the extrapolation technique, there are marked differences in the G values computed from the upper and lower crack faces. A striking observation is that the G_I, G_{II}, and G values from the upper crack face are by and large much greater than those computed from the lower crack face. This appears to be so, because the upper crack face is stressed, while the lower one is unstressed. Taking into account the average values for G_I, G_{II}, and G, an error of 10-20% with respect to the reference numerical solution (VCC-2C) is observable. However, if the results from only the upper crack face are taken into consideration, the errors involved are 5% or less. Even though the displacement extrapolation scheme tends to give conservative estimates for the energy release rates, it is undoubtedly much more accurate than the displacement method – equation (2.11).

In Tables 3.8 – 3.15, the energy release rates obtained from the beam solution are compared to those from the VCC-2C method (the representative numerical scheme), while in Figures 3.38 – 3.41, the same data are graphically illustrated. From the data, it is apparent that there is a disagreement between the beam solution and numerical results. The disparity is especially large for short cracks. In a study conducted by Broughton, [2] cracks lengths of 10-13 mm were observed in composite specimens tested in the Iosipescu shear test (Figure 4.2). Considering the above fact, it is appropriate to discuss the results for long cracks only. From Tables 3.8 and 3.9, it can be seen that even for $-\phi$ and $+\phi$ loading angles, there is a significant disagreement; however, from Tables 3.8 – 3.11, it can be observed that, for long cracks (a $\geq$ 10mm) under pure shear $\phi = 0°$, there is reasonable agreement between the beam solution and the VCC-2C results. The G values for long cracks under pure shear from the beam theory solutions are within 10% of the numerical results. The estimates for the mode partitions G_I and G_{II} from the beam theory solution do not match the 2C-results (Tables 3.12 – 3.15) at all.

The cause for the disagreement between the predictions from the analytical model in comparison to the numerical results needs to be elaborated. The beam theory is applicable to beams of constant cross-section, with the well-known parabolic shear stress distribution. As opposed to a beam, in the Iosipescu specimen, the shear stress distribution is uniform along the notch-root axis due to the presence of two sharp V-notches. In case of short cracks, the constant shear stress distribution affects the G calculations, and hence a marked difference between the analytical and numerical G values is observable. For long cracks, the notch-effects are reduced, and therefore, the Iosipescu specimen can be considered to be equivalent to a beam. In this case, the G values from the beam solution are found to be in fair agreement with the VCC-2C results.

In Figure 3.41, the variation of G_I and G_{II} with crack length for $\phi = 0°$, and ER = 1 and ER = 14.2 (A-type) is shown. The crack-tip loading conditions are always mixed mode, with the normal- and shear-components varying with the crack length a. For short cracks ($a \leq 4mm$), mode I is dominant ($G_I > G_{II}$), while for long cracks ($a \geq 10mm$), mode II is dominant ($G_{II} > G_I$). The above trends are also evident in Tables E.1 – E.4 for all other loading angles too. It is seen from Tables E.1 – E.4 that for a particular crack length a and ER = 1, the mixed mode energy release rate G monotonically decreases as the loading changes from $\phi = -45°$ (shear-tension) to $\phi = 30°$ (shear-compression). Similar trends are also observable for ER = 14.2 (A-type), although for $\phi = -45°$, there is a drop in the G value. Taking into account the observable trends in the G values, it can be inferred that orthotropic composites are more prone to fracture under shear-tension (–ϕ) loading conditions than under shear-compression (+ϕ) loading conditions.

Table 4.1. Comparison of energy release rates (G, G_I, G_{II}) by the displacement extrapolation method and the VCC-2C scheme: ER = 14.2 (A-type)

ϕ (deg.)	a (mm)	G_I^U	G_I^L	G_{II}^U	G_{II}^L	G^U	G^L	G_I	G_{II}	G
		Displacement extrapolation[†] – linear regression (kJ/m²)						VCC-2C scheme (kJ/m²)		
-45	1	1.207	0.644	0.254	0.178	1.461	0.822	1.009	0.256	1.265
	4	0.884	0.548	0.310	0.233	1.194	0.780	0.772	0.324	1.096
	7	0.565	0.403	0.369	0.275	0.933	0.679	0.520	0.381	0.901
	10	0.225	0.200	0.300	0.214	0.525	0.413	0.224	0.301	0.524
	13	0.076	0.100	0.256	0.179	0.332	0.279	0.093	0.253	0.346
0	1	1.130	0.610	0.083	0.069	1.213	0.679	0.952	0.088	1.040
	4	0.830	0.594	0.203	0.161	1.033	0.754	0.774	0.218	0.993
	7	0.483	0.404	0.240	0.188	0.723	0.592	0.482	0.255	0.736
	10	0.234	0.245	0.207	0.157	0.441	0.402	0.258	0.216	0.474
	13	0.096	0.138	0.155	0.116	0.251	0.253	0.125	0.159	0.284
30	1	0.578	0.258	0.007	0.010	0.585	0.268	0.451	0.009	0.460
	4	0.376	0.250	0.051	0.041	0.427	0.291	0.339	0.055	0.394
	7	0.182	0.147	0.066	0.052	0.248	0.198	0.177	0.070	0.247
	10	0.011	0.073	0.054	0.040	0.065	0.114	0.075	0.056	0.131
	13	0.019	0.033	0.036	0.027	0.055	0.060	0.027	0.037	0.064

[†] Superscripts U and L refer to values computed from a linear regression along the upper and lower crack faces respectively (see Figure 3.35a).
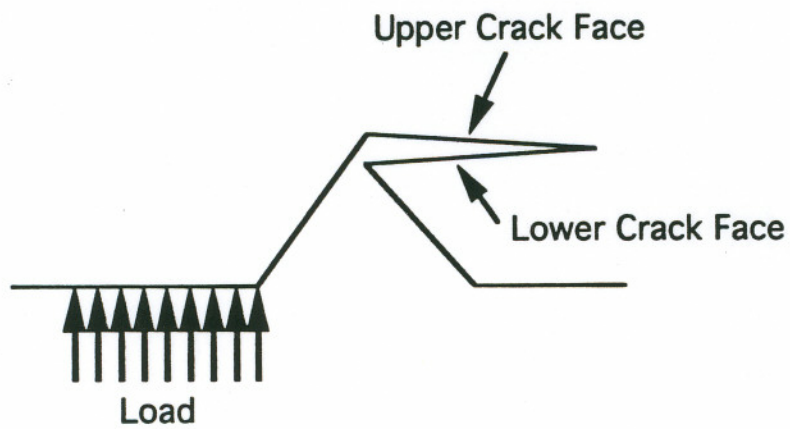
Figure 4.1 Crack faces.
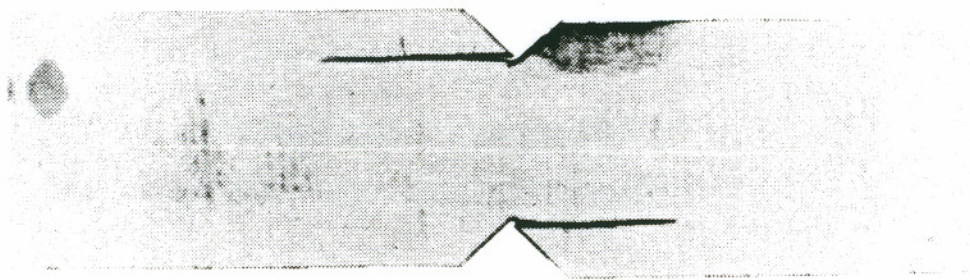
Figure 4.2 Two skew-symmetric cracks in a APC-2 carbon/PEEK Iosipescu
specimen tested under shear loading conditions ($\phi = 0°$).[2]

CHAPTER 5

CONCLUSIONS

In this study, a preliminary numerical investigation of the biaxial Iosipescu test method was carried out. The numerical study, using linear elastic finite element analysis under generalized plane stress, can be broadly divided into three parts: stress distribution in isotropic and orthotropic Iosipescu specimens; evaluation of the stress singularity at angular sharp notches by the Finite Element Iterative Method; and extraction of fracture parameters (G_I, G_{II}, G) for skew-symmetric splits along the fiber direction in Iosipescu specimens. The results obtained in this study lead to the following conclusions:

(1) The stress distribution in the Iosipescu specimen strongly depends on the specimen geometry, elastic properties, and the biaxial loading conditions.

(2) There exists a complex stress distribution in the vicinity of the notch roots. The transverse normal stresses are tensile on the opposite side of the loading points, while they are compressive on the same side of the loading points along the horizontal line passing through the notch roots.

(3) Singular stress fields are present at the notch roots ($\rho = 0$) in isotropic as well as orthotropic materials. Hence, the usage of the term "stress concentration factor K_t at the notch root" is meaningless.

(4) The relation $K_t = A(E_{11}/E_{22})^{1/4}$, proposed by Kumosa and Hull[7], is inapplicable at the notch root of sharp V-notches ($\rho = 0$). The above equation breaks-down in the region dominated by the singular stress field; however, outside the singular domain,

the relation between the orthotropy ratio and the shear stress is valid. This fact has been demonstrated by Broughton and co-workers[2, 8] who have successfully applied the above relationship as a shear correction factor in the estimation of shear modulus for unidirectional composite materials.

(5) The Finite Element Iterative Method is a simple and accurate tool to determine the power of the singular field at sharp notches in either isotropic or orthotropic materials.

(6) The strong singularity λ_a, and the weak singularity λ_b are dominant at the notch root, under mode I and mode II loadings respectively.

(7) There exists a critical angle α_{cr} above which λ_a and λ_b vanish under shear loading conditions. With increasing ER, the critical angle α_{cr} increases when the stiffness is greater along the X-axis, but decreases when the stiffness is greater along the Y-axis, with respect to $\alpha_{cr} \approx 103°$, which is the critical angle for the isotropic case.

(8) The stress singularities at the notch root are a function of the orthotropy ratio ER, and also depend on the material orientation. With increasing ER, λ_a and λ_b increase when the stiffness is greater along the X-axis, but decrease when the stiffness is greater along the Y-axis, with respect to the isotropic case.

(9) Under mixed mode loading, the strong singularity λ_a is always dominant at the notch root.

(10) In composite Iosipescu specimens, with fibers along the X-direction, skew symmetric splits, originate from the notch roots, and propagate along the fiber direction. The axial splits propagate under mixed mode conditions, with $G_I > G_{II}$ for short cracks ($a \leq 4\text{mm}$), and $G_{II} > G_I$ for long cracks ($a \geq 10\text{mm}$).

(11) The fracture-parameter estimations for axial splits in Iosipescu specimens is strongly dependent on the material behavior: accurate results for isotropic materials are obtained by all the numerical schemes considered in this study; however, the same isn't true for orthotropic materials. The numerical results obtained for the energy release rates by the modified crack closure integral schemes (energy-based methods) are much more accurate than the displacement extrapolation techniques.

(12) The analytical estimations for the energy release rates by the beam theory solution are in poor agreement with the numerical results obtained from the modified crack closure integral schemes, especially for short and medium crack lengths. However, for long crack lengths (a ≥ 10mm), the G values from the beam solution are found to be in fair agreement with those from the crack closure schemes.

CHAPTER 6

SUGGESTIONS FOR FUTURE WORK

This work has raised several interesting questions in regard to the fracture and failure aspects of Iosipescu specimens under biaxial loading conditions. Some of the subject areas that can be explored in future research-studies are as follows:

(1) The material behavior and the notch geometry are two critical parameters that govern the stress state in the vicinity of the notch roots in the Iosipescu specimen. An elasto-plastic analysis, with finite notch-root radius would be a much better computational model, in order to represent the actual stress state realized in an experiment, wherein, plasticity-effects are always present at the notch root of the specimen. Furthermore, from a 3-D analysis, it would be possible to ascertain if through-the-thickness effects are pronounced, and also if the loading points and other constraints in the experimental set-up have an influence on the stress distribution in the specimen.

(2) In this study, the finite element meshes for uncracked as well as cracked Iosipescu specimens were not optimized. Future studies could look into the optimization of the finite element meshes, which could lead to a standardization of the finite element meshes used in the numerical analysis of the biaxial Iosipescu test.

(3) In order to develop the "ideal" specimen geometry for shear testing, the optimum notch angle and orthotropy ratio for which there is pure shear in the specimen can be investigated.

126

CHAPTER 6

SUGGESTIONS FOR FUTURE WORK

This work has raised several interesting questions in regard to the fracture and failure aspects of Iosipescu specimens under biaxial loading conditions. Some of the subject areas that can be explored in future research-studies are as follows:

(1) The material behavior and the notch geometry are two critical parameters that govern the stress state in the vicinity of the notch roots in the Iosipescu specimen. An elasto-plastic analysis, with finite notch-root radius would be a much better computational model, in order to represent the actual stress state realized in an experiment, wherein, plasticity-effects are always present at the notch root of the specimen. Furthermore, from a 3-D analysis, it would be possible to ascertain if through-the-thickness effects are pronounced, and also if the loading points and other constraints in the experimental set-up have an influence on the stress distribution in the specimen.

(2) In this study, the finite element meshes for uncracked as well as cracked Iosipescu specimens were not optimized. Future studies could look into the optimization of the finite element meshes, which could lead to a standardization of the finite element meshes used in the numerical analysis of the biaxial Iosipescu test.

(3) In order to develop the "ideal" specimen geometry for shear testing, the optimum notch angle and orthotropy ratio for which there is pure shear in the specimen can be investigated.

(4) Extensive experimental studies need to be conducted in order to determine the elastic properties and strengths of the materials. The failure envelope of isotropic as well as composite materials must be obtained in order to evaluate the test method for biaxial characterization of isotropic as well as composite materials. The experimental data would be of tremendous importance for the development of better computational models in the future.

(5) The application of the Finite Element Iterative Method to sharp notches can be extended by investigating the eigenfunctions (angular distribution) associated with the eigenvalue problem.

(6) There have been very few studies on the nature of the singular stress field in 3-D anisotropic wedges. The power of the singular stress field in 3-D wedges would probably be a function of the through-the-thickness depth, apart from the wedge angle being a parameter that influences λ. The FEIM would be an ideal candidate to apply, in order to compute the eigenvalues and eigenfunctions associated with the 3-D singular stress field.

(7) Even for finite notch radius, singular stress fields theoretically exist. The FEIM mesh and approach for finite notch-radii can be studied in order to come-up with a suitable formulation that can be implemented on any general-purpose finite element program.

(8) Many questions still remain unanswered in the orthotropic fracture analysis of the Iosipescu specimen. Firstly, an in-depth study of all the numerical schemes (their pros and cons) for mixed mode fracture analysis needs to be carried out. This would establish firm guidelines in regard to the "best" approach for analyzing mixed mode fracture in the Iosipescu specimen.

(9) The crack closure integral schemes can only be applied to linear elastic analysis. Hence, especially for mixed mode fracture in three-dimensional nonlinear problems, the scope of other numerical techniques such as the virtual crack extension[30,31] and the equivalent domain integral[80-83] can be investigated.

(10) Experimental studies on the Iosipescu specimen under biaxial loading conditions will yield the critical values for mode I (G_{Ic}) and mode II (G_{IIc}) crack propagation. The above data, in conjunction with the numerically obtained values (G_I, G_{II}, G) in this study, will be able to give further insights in regard to the dominant fracture mechanisms in 0-deg unidirectional composites. The above analyses (experimental and numerical) can also be carried out for cracks along the notch-root axis in 90-deg unidirectional composites.

(11) In this study, the beam theory results were not in agreement with the numerical results, especially for short and medium crack lengths. Attempts at modifying the beam theory for the Iosipescu specimen configuration and loading conditions can be looked into, in order to come-up with a suitable analytical model for the energy release rates in Iosipescu specimens.

(12) Finally, the biaxial Iosipescu fixture is currently being used to investigate unidirectional composite materials, as well as adhesively-bonded composite systems. Since the fixture has the capability of testing specimens under cyclic loading, fatigue and the problems that come with it are another new-dimension that can be explored using the biaxial Iosipescu fixture.

References

1. S. Lee and M. Munro, "Evaluation of in-plane shear test methods for composite materials by the decision analysis technique," *Composites*, vol. 17, pp. 11-22, January 1986.

2. W. R. Broughton, "Shear properties of unidirectional carbon fibre composites," *Ph.D. thesis*, University of Cambridge, 1989.

3. N. Iosipescu, "New accurate procedure for single shear testing of metals," *Journal of Materials*, vol. 2, no. 1, pp. 537-566, 1967.

4. D. F. Adams and D. E. Walrath, "Iosipescu shear properties of SMC composite materials," in *Composite Materials: Testing and Design (Sixth Conference), ASTM STP 787*, ed. I. M. Daniel, pp. 19-33, 1982.

5. D. E. Walrath and D. F. Adams, "Analysis of the stress state in an Iosipescu shear test specimen," Report UWME-DR-301-102-1, Department of Mechanical Engineering, University of Wyoming, Laramie, Wyoming, June 1983.

6. J. A. Barnes, M. Kumosa, and D. Hull, "Theoretical and experimental evaluation of the Iosipescu shear test," *Composites Science and Technology*, vol. 28, pp. 251-268, 1987.

7. M. Kumosa and D. Hull, "Mixed-mode fracture of composites using the Iosipescu shear test," *International Journal of Fracture*, vol. 35, pp. 83-102, 1987.

8. W. R. Broughton, M. Kumosa, and D. Hull, "Analysis of the Iosipescu shear test as applied to unidirectional carbon-fiber reinforced composites," *Composites Science and Technology*, vol. 38, pp. 299-325, 1990.

9. D. E. Walrath and D. F. Adams, "Verification and application of the Iosipescu shear test method," Report UWME-DR-401-103-1, Department of Mechanical Engineering, University of Wyoming, Laramie, Wyoming, June 1984.

10. D. E. Walrath and D. F. Adams, "Iosipescu shear properties of graphite fabric/epoxy composite laminates," Report UWME-DR-501-103-1, Department of Mechanical Engineering, University of Wyoming, Laramie, Wyoming, June 1985.

11. D. E. Walrath and D. F. Adams, "Current status of the Iosipescu shear test method," *Journal of Composite Materials*, vol. 21, pp. 494-507, June 1987.

12. D. E. Walrath and D. F. Adams, "Further developments of the Iosipescu shear test method," *Experimental Mechanics*, vol. 27, pp. 113-119 , June 1987.

13. S. S. Wang, D. P. Goetz , and H. T. Corten, "Fracture of random short short-fiber SMC composite under shear loading," *International Journal of Fracture*, vol. 26, pp. 215-227, 1984.

14. J. L. Sullivan, B. G. Kao , and H. Van Oene , "Shear properties and a stress analysis obtained from vinyl-ester Iosipescu specimens," *Experimental Mechanics* , vol. 24, pp. 223-232, 1984.

15. S. R. Swanson, M. Messick, and G. R. Toombes , *Composites*, vol. 16, no. 3, pp. 220-224, 1985.

16. S. R. Spiegel , J. W. Sawyer , and R. Prabhakaran , "An investigation of the Iosipescu and asymmetrical four-point bend tests," *Experimental Mechanics* , vol. 27 , no. 1, pp. 57-63 , 1987.

17. H. Ho, M. Y. Tsai , J. Morton, and G. L. Farley, "Numerical analysis of the Iosipescu specimens for composite materials," *Experimental Mechanics*, 1992, in

press.

18. J. Morton, H. Ho, M. Y. Tsai , and G. L. Farley, ''An evaluation of the Iosipescu specimen for composite materials shear property measurements,'' *Journal of Composite Materials* , vol. 26, no. 5, pp. 708-750, 1992.

19. M. J. Pindera and C. T. Herakovich, ''Shear characterization of unidirectional composites with off-axis tension test,'' *Experimental Mechanics*, vol. 26, pp. 103-112, 1986.

20. J. A. Barnes, ''Torsion testing of filament wound composite cylinders,'' *Ph.D. thesis*, University of Cambridge, 1986.

21. M. Kumosa, ''Fracture of hoop wound GRP tubes with circumferential cracks subjected to torsional loading,'' *Fatigue and Fracture of Engineering Materials and Structures* , in press (1992).

22. M. Arcan, Z. Hashin, and A. Voloshin, ''A method to produce uniform plane-stress states with application to fibre-reinforced materials,'' *Experimental Mechanics*, vol. 18, pp. 141-146, 1978.

23. A. Voloshin and M. Arcan, ''Failure of unidirectional fibre-reinforced materials - new methodology and results,'' *Experimental Mechanics*, pp. 280-284, August 1980.

24. S. Parhizgar, L. W. Zachary, and C. T. Sun, ''Application of the principles of linear elastic mechanics to the composite materials,'' *International Journal of Fracture*, vol. 20, pp. 247-256, 1982.

25. G. C. Sih, P. C. Paris, and G. R. Irwin, ''On cracks in rectilinearly anisotropic bodies,'' *International Journal of Fracture*, vol. 1, pp. 189-203, 1965.

26. F. G. Buchholz, M. Kumosa, and M. Burger, "Finite-element analysis of mixed mode fracture of orthotropic Iosipescu-specimens," in *Conference Proceeding 10, Reutlinger Arbeitstagung Finite Elemente in der Praxis*, pp. 353-376, Reutlinger, Federal Republic of Germany, April, 1989.

27. F. G. Buchholz, M. Burger, M. Kumosa, and H. Eggers , "Mixed mode fracture analysis of orthotropic laminates by local and global energy methods," in *Fifth International Conference on Numerical Methods in Fracture Mechanics*, Freiburg, Federal Republic of Germany, 1990.

28. D. Hull, *An introduction to composite materials*, Cambridge University Press, Cambridge, 1981.

29. D. M. Parks, "A stiffness derivative finite element technique for determination of crack tip stress intensity factors," *International Journal of Fracture*, vol. 10, pp. 487-502, 1974.

30. T. K. Hellen, "On the method of virtual crack extension," *International Journal for Numerical Methods in Engineering*, vol. 9, pp. 187-207, 1975.

31. D. M. Parks, "The virtual crack extension method for nonlinear material behavior," *Computer Methods in Applied Mechanics and Engineering*, vol. 12 , pp. 353-364 , 1977.

32. J. R. Rice, "A path independent integral and the approximate analysis of strain concentration by notches and cracks," *Journal of Applied Mechanics*, vol. 35, pp. 379-386, 1968.

33. S. K. Chan, I. S. Tuba , and W. K. Wilson , "On the finite element method in linear fracture mechanics," *Engineering Fracture Mechanics*, vol. 2, pp. 1-17, 1970.

34. E. F. Rybicki and M. F. Kanninen, "A finite element calculation of stress intensity factors by a modified crack closure integral," *Engineering Fracture Mechanics*, vol. 9, pp. 931-938, 1977.

35. T. K. O'Brien, "Characterization of delamination onset and growth in a composite laminate," in *Damage in Composite Materials, ASTM STP 775*, ed. K. L. Reifsnider, American Society for Testing and Materials, pp. 140-167, 1982.

36. F. G. Buchholz, "Improved formulae for the finite element calculation of the strain energy release rate by the modified crack closure integral method," in *Accuracy Reliability and Training in FEM-Technology (Editor J. Robinson)*, pp. 650-659, Robinson and Associates, Dorset, 1984.

37. T. Krishnamurthy, T. S. Ramamurthy, K. Vijayakumar, and B. Dattaguru, "Modified crack closure integral method for higher order finite elements," in *Proceedings International Conference on Finite Elements in Computational Mechanics (Editor T. Kant)*, pp. 891-900, Pergamon Press, Oxford, 1985.

38. I. S. Raju, "Calculation of strain energy release rates with higher order and singular finite elements," *Engineering Fracture Mechanics*, vol. 28, pp. 251-274, 1987.

39. R. D. Henshell and K. G. Shaw, "Crack tip finite elements are unnecessary," *International Journal for Numerical Methods in Engineering*, vol. 9 , pp. 495-507 , 1975.

40. R. S. Barsoum, "On the use of isoparametric finite elements in linear fracture mechanics," *International Journal for Numerical Methods in Engineering*, vol. 10 , pp. 25-37 , 1976.

41. J. M. Bloom, "An evaluation of a new crack tip element -- the distorted 8-node isoparametric element," *International Journal of Fracture*, vol. 11, pp. 705-707, 1975.

42. C. F. Shih, H. G. deLorenzi, and M. D. German, "Crack extension modeling with singular quadratic isoparametric elements," *International Journal of Fracture*, vol. 12, no. 4, pp. 647-651, August, 1976.

43. L. Banks-Sills and Y. Bortman, "Reappraisal of the quarter-point quadrilateral element in linear elastic mechanics," *International Journal of Fracture*, vol. 25, pp. 169-180, 1984.

44. L. Banks-Sills and D. Sherman, "Comparison of methods for calculating stress intensity factors with quarter-point elements," *International Journal of Fracture*, vol. 32, pp. 127-140, 1986.

45. S. L. Pu, M. A. Hussain, and W. E. Lorenson, "The collapsed cubic isoparametric element as a singular element for crack problems," *International Journal for Numerical Methods in Engineering*, vol. 12, pp. 1727-1742, 1978.

46. G. R. Irwin, *Handbuch der Physik*, 6, pp. 551-566, 1958.

47. J. G. Williams, "Energy release rates for cracked laminates," *International Journal of Fracture*, vol. 36, pp. 101-119, 1988.

48. J. G. Williams, "End corrections for orthotropic DCB specimens," *Composite Science and Technology* , vol. 35, pp. 367-376 , 1989.

49. S. Hashemi , A. J. Kinloch , and J. G. Williams, "The analysis of interlaminar fracture in uniaxial fiber-polymer composites," in *Proceedings of Royal Society A*, vol. 42, pp. 173-199, 1990.

50. M. L. Williams, "Stress singularities resulting from various boundary conditions in angular corner of plates in extension," *Journal of Applied Mechanics*, vol. 19, pp. 526-528, December 1952.

51. B. Gross and A. Mendelson, "Plane elastostatic analysis of V-notched plates," *International Journal of Fracture*, vol. 8, pp. 267-276, 1972.

52. K. Y. Lin and P. Tong, "Singular finite elements for the fracture analysis of V-notched plates," *International Journal for Numerical Methods in Engineering*, vol. 15, pp. 1343-1354, 1980.

53. A. Portela, M. H. Aliabadi, and D. P. Rooke, "Boundary element analysis of V-notched plates," in *Boundary Element Techniques: Applications in Engineering, Proceeding of the fourth International Conference on Boundary Element Technology, Windsor, Canada*, ed. C. A. Brebbia, N. G. Zamani, pp. 147-155, Computational Mechanics Publications, Southampton Boston, June, 1989.

54. V. L. Hein and F. Erdogan, "Stress singularities in a two-material wedge," *International Journal of Fracture Mechanics*, vol. 7, pp. 317-330, September 1971.

55. D. B. Bogy and K. C. Wang , "Stress singularities at interface corners in bonded dissimilar isotropic elastic materials ," *International Journal of Solids and Structures* , vol. 7 , pp. 993-1005, 1971.

56. Z. Knesl, A. Sramek, J. Kadourek, and F. Kroupa, *Stress concentration at the edges of coatings on tensile specimens*, to be published.

57. W. C. Carpenter, "A collocation procedure for determining fracture mechanics parameters at a corner," *International Journal of Fracture*, vol. 24, pp. 255-266, 1984.

58. W. C. Carpenter, "The eigenvector solution for a general corner or finite opening crack with further studies on the collocation procedure," *International Journal of Fracture*, vol. 27, pp. 63-74, 1985.

59. R. Rosel, "On the wedge / notch eigenvalues," *International Journal of Fracture*, vol. 33, pp. 61-71, 1987.

60. G. B. Sinclair, M. Okajima, and J. H. Griffin Jr., "Path independent integrals for computing stress intensity factors at sharp notches in elastic plates," *International Journal for Numerical Methods in Engineering*, vol. 20, no. 6 , pp. 999-1008, 1984.

61. G. B. Sinclair and M. Kondo, "On the stress concentration at sharp re-entrant corners in plates," *International Journal of Mechanical Sciences*, vol. 26, pp. 477-487, 1984.

62. S. S. Wang and A. Dasgupta , "Development of Iosipescu-type test for determining in-plane shear properties of fiber composite materials: critical analysis and experiment," Report No. UILU-ENG-86-5021, Department of Theoretical and Applied Mechanics and Aeronautical and Astronautical Engineering, University of Illinois, Urbana, 1986.

63. R. S. Barsoum, "Finite element solution of the eigenvalue problems associated with the fracture of composites," in *Fourth International Conference on Numerical Methods in Fracture Mechanics, San Antonio, TX, 23-27 March 1987*, pp. 533-550, Pineridge Press Ltd., Swansea UK, 1987.

64. R. S. Barsoum, "Cracks in anisotropic materials - an iterative solution of the eigenvalue problem," *International Journal of Fracture*, vol. 22, pp. 59-67, 1986.

65. R. S. Barsoum, "Theoretical basis of the finite element iterative method for the eigenvalue problem in stationary cracks," *International Journal for Numerical Methods in Engineering*, vol. 25, pp. 531-539, 1988.

66. R. S. Barsoum, "Application of the finite element iterative method to a eigenvalue

problem of a crack between dissimilar media," *International Journal for Numerical Methods in Engineering*, vol. 25, pp. 541-554, 1988.

67. R. S. Barsoum, "Singular behaviour near an interface crack tip of power law hardening materials using the finite element iterative method," *International Journal for Numerical Methods in Engineering*, vol. 29, pp. 699-717, March 1990.

68. R. S. Barsoum, "Asymptotic fields at interfaces using the finite element iterative method," *Computers and Structures*, vol. 35, pp. 285-292, 1990.

69. R. S. Barsoum, "Asymptotic fields in adhesive fracture," *Journal of Adhesion*, vol. 29, pp. 149-166, 1989.

70. R. S. Barsoum and Tzi-Kang Chen, "Three dimensional surface singularity of an interface crack," *International Journal of Fracture*, vol. 50, pp. 221-237 , 1991.

71. R. S. Barsoum, "Singularities in composite materials application," in *Composite Material Response*, ed. G. C. Sih, Elsevier Applied Science Publications, Barking, U.K., 1988.

72. I. S. Raju and John H. Crews Jr., "Interlaminar stress singularities at a straight free edge in composite laminates," *Computers and Structures*, vol. 14, pp. 21-28, 1981.

73. E. D. Reedy Jr., "Intensity of the stress singularity at the interface corner between a bonded elastic and rigid layer," *Engineering Fracture Mechanics*, vol. 36, no. 4, pp. 575-583, 1990.

74. E. D. Reedy Jr., "Intensity of the stress singularity at the interface corner of a bonded elastic layer subjected to shear," *Engineering Fracture Mechanics*, vol. 38, no. 4/5, pp. 273-281, 1991.

75. M. Stern, "Families of consistent conforming elements with singular derivative

fields," *International Journal for Numerical Methods in Engineering*, vol. 14, pp. 409-421, 1979.

76. J. H. Wilkinson, in *The Algebraic Eigenvalue Problem*, Clarendon Press, Oxford, 1965.

77. G. J. DeSalvo and R. W. Gorman, in *Ansys Engineering Analysis System; User's Manual*, vol. 1, Swanson Analysis System Inc., May 1, 1989.

78. A. C. Kaya and F. Erdogan, "Stress intensity factors and COD in an orthotropic strip," *International Journal of Fracture*, vol. 16, no. 2, pp. 171-190, April 1980.

79. J. G. Williams, *Private communications with Dr. M. Kumosa, 1989.*

80. N. Miyakazi, T. Watanabe, and G. Yagawa, "The virtual crack extension of J- and $\hat{J}$-integrals," *Engineering Fracture Mechanics*, vol. 22, pp. 975-987, 1985.

81. B. Moran and C. F. Shih, "Crack tip and associated domain integrals from momentum and energy balance," *Engineering Fracture Mechanics*, vol. 27, pp. 615-642, 1987.

82. G. P. Nikishkov and S. N. Atluri , "Calculation of fracture mechanics parameters for an arbitrary three-dimensional crack, by the 'equivalent domain integral' method," *International Journal for Numerical Methods in Engineering*, vol. 24, pp. 1801-1821, 1987.

83. K. N. Shivakumar and I. S. Raju, "An equivalent domain integral method for three-dimensional mixed-mode fracture problems," *Engineering Fracture Mechanics*, vol. 42, no. 6, pp. 935-959, 1992.

APPENDIX A

In this Appendix, using moment and force balance, the external loads in the biaxial Iosipescu stress test are derived. The loads P_1 and P_2 are expressed in terms of the total compressive load P, loading angle ϕ, and specimen dimensions.

A.1. Derivation of Load Components

In the biaxial Iosipescu test method, the total compressive load P is applied at various loading angles ϕ, where ϕ is the angle between P_o and P (see Figure 2.6 in Chapter 2). The angle ϕ is taken as positive when the specimen is rotated in a counter-clockwise direction and negative when the rotation is clockwise. The test specimen is loaded in shear-compression for positive loading angles ($+\phi$) and in shear-tension for negative loading angles ($-\phi$). The analytical models of the Iosipescu specimen for the two cases ($+\phi$ and $-\phi$) are shown in Figures A.1a and A.1b respectively.

By simple moment and force balance considerations, the following expressions for the load components as a function of ϕ are obtained:

$$P_1 = \frac{P}{\left[1 - \left\{\dfrac{2c - h'\tan\phi}{2l + h'\tan\phi}\right\}\right]} \quad \text{and} \quad P_2 = \frac{P}{\left[\left\{\dfrac{2l + h'\tan\phi}{2c - h'\tan\phi}\right\} - 1\right]} \tag{A.1}$$

where the orientation of P_1 and P_2 for $+\phi$ and $-\phi$ loading angles are shown in Figures A.1a and A.1b respectively.

In the load component calculations, the values of ϕ are to be taken as positive for

139

$+\phi$ and negative for $-\phi$ loading angles. From (A.1), the critical loading angle for counter-clockwise rotation $(+\phi)$ can be written as:

$$\phi_{cr}^{+} = \tan^{-1}(2c/h')$$
(A.2)

while that for clockwise rotation $(-\phi)$ can be expressed as:

$$\phi_{cr}^{-} = \tan^{-1}(-(l-c)/h')$$
(A.3)

From (A.2) and (A.3), it can be inferred that the expressions for the load components are admissible only for values of ϕ in the range $\phi_{cr}^{-} \leq \phi \leq \phi_{cr}^{+}$ (Note: ϕ_{cr}^{-} is a negative value).
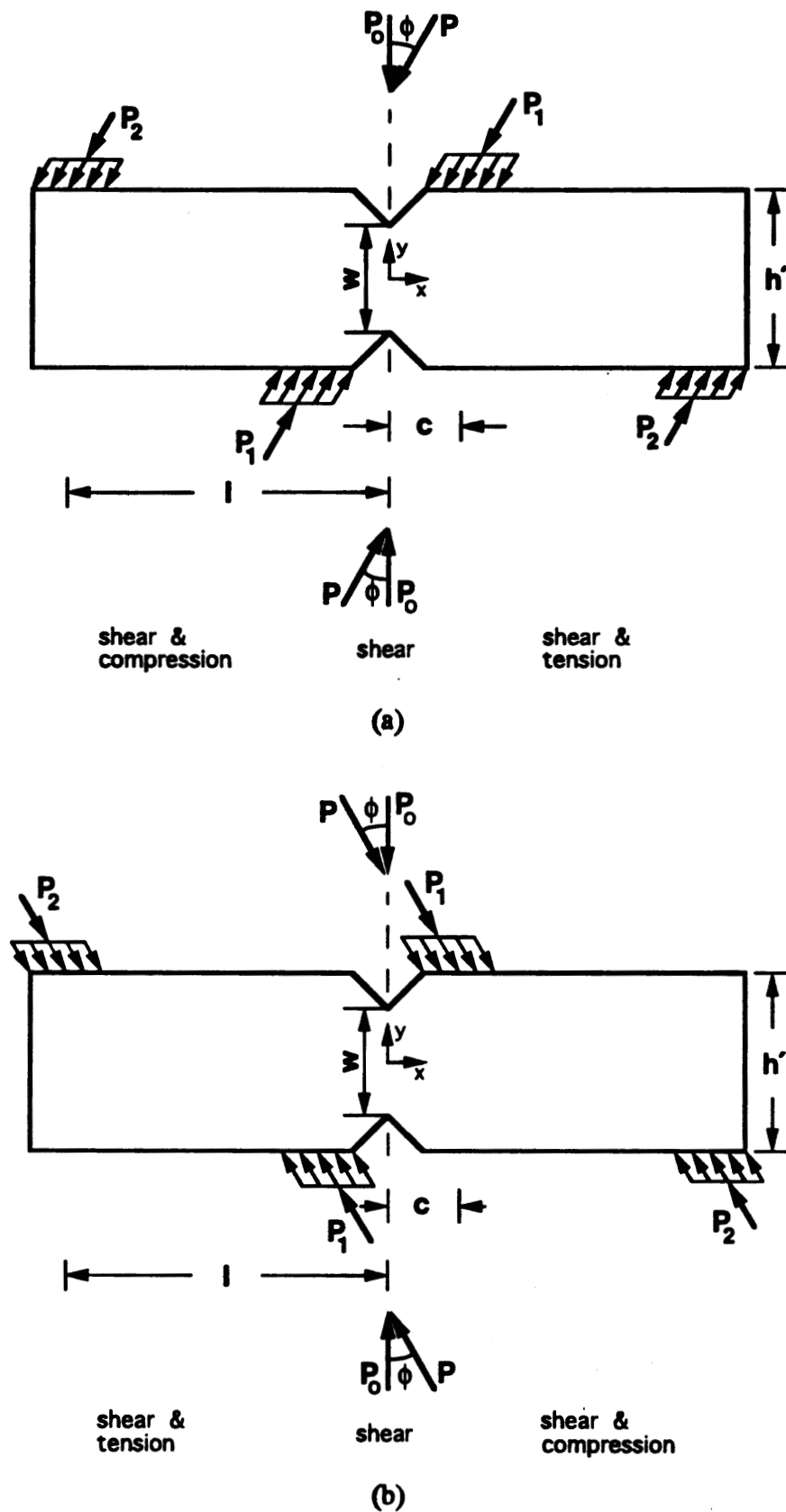
Figure A.1 Iosipescu specimen under in-plane biaxial stress state. (a) anti-clockwise rotation (+ φ); and (b) clockwise rotation (− φ).

APPENDIX B

P = 115 N

(MPa)

■	0.389445
■	15.567
▨	30.746
▨	45.924
▨	61.102
▨	76.28
▨	91.458
▨	106.636
▨	121.814
■	136.992

(a)

P = 115 N

(MPa)

■	0.241393
■	5.744
▨	11.247
▨	16.75
▨	22.252
▨	27.755
▨	33.258
▨	38.76
▨	44.263
■	49.766
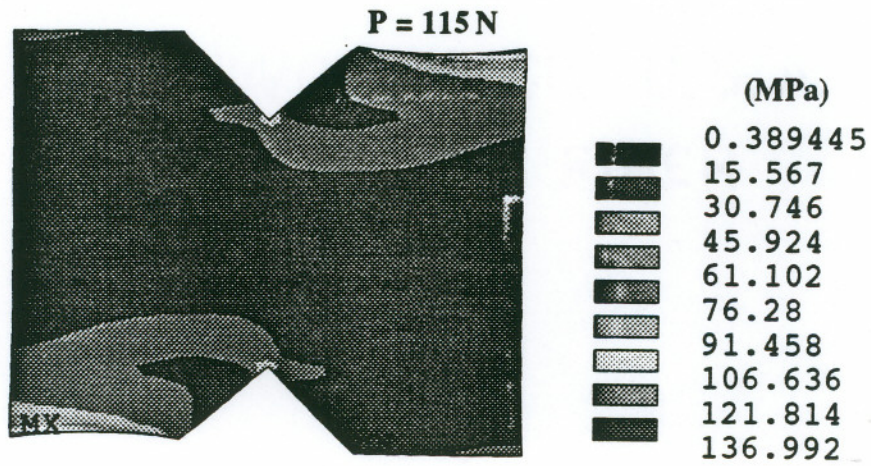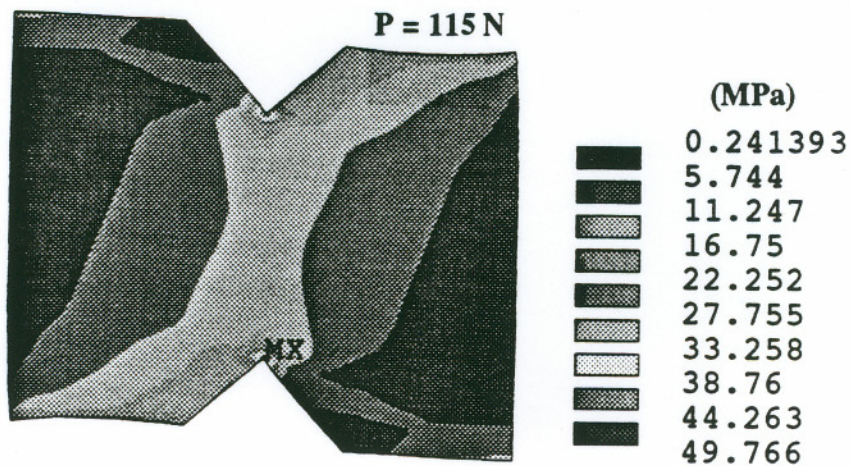
(b)

Figure B.1 von Mises stress contours for $\alpha = 90°$ and ER = 14.2 (A-type).
(a) $\phi = -30°$ (shear–tension); and (b) $\phi = +30°$ (shear–compression).

142
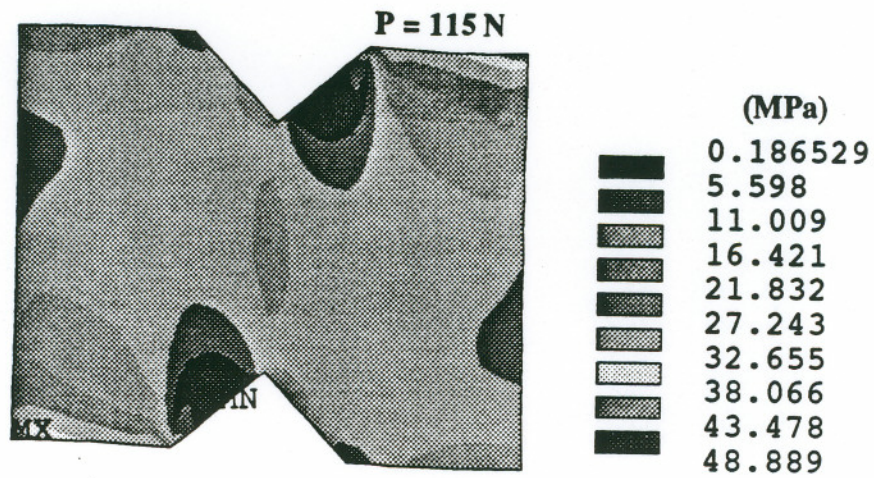
(a)
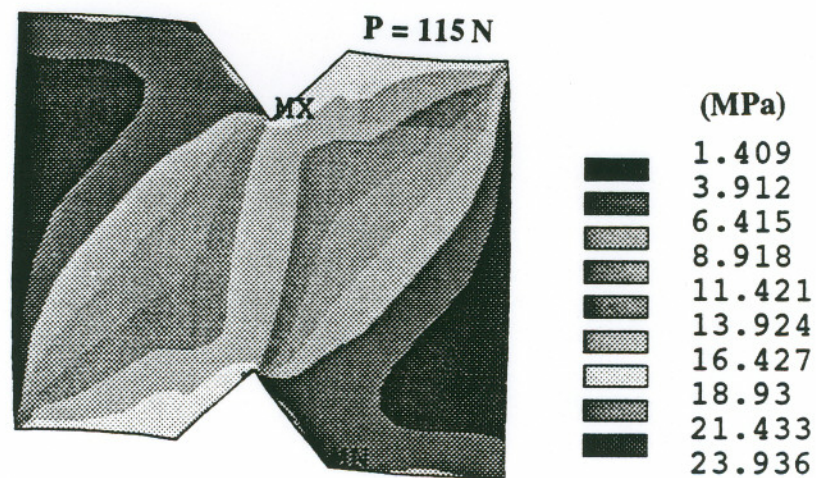
(b)

Figure B.2 von Mises stress contours for $\alpha = 90°$ and ER = 14.2 (B-type). (a) $\phi = -30°$ (shear–tension); and (b) $\phi = +30°$ (shear–compression).

144
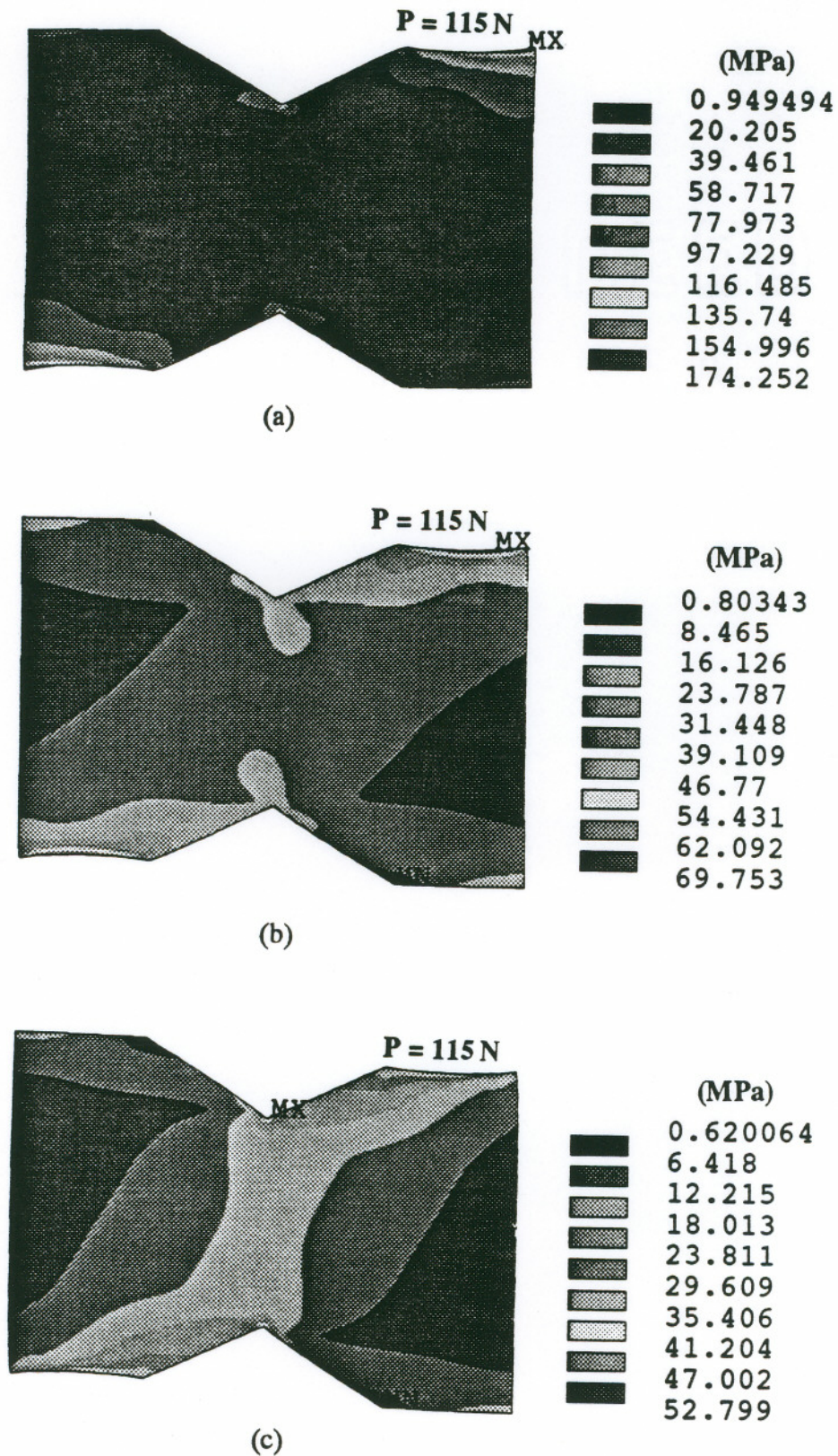
Figure B.3 von Mises stress contours for α = 120° and ER = 14.2 (A-type).
(a) φ = −30° (shear−tension); (b) φ = 0° (pure shear); and
(c) φ = +30° (shear-compression).

P = 115 N

(MPa)

1.538
44.938
88.338
131.738
175.138
218.539
261.939
305.339
348.739
392.139

(a)

P = 115 N

(MPa)

7.143
20.82
34.497
48.174
61.851
75.528
89.206
102.883
116.56
130.237

(b)

P = 115 N

(MPa)

3.447
13.021
22.595
32.169
41.743
51.317
60.89
70.464
80.038
89.612

(c)
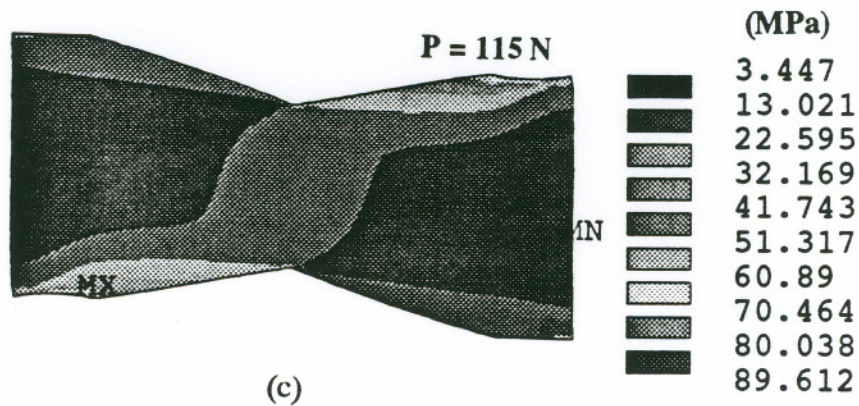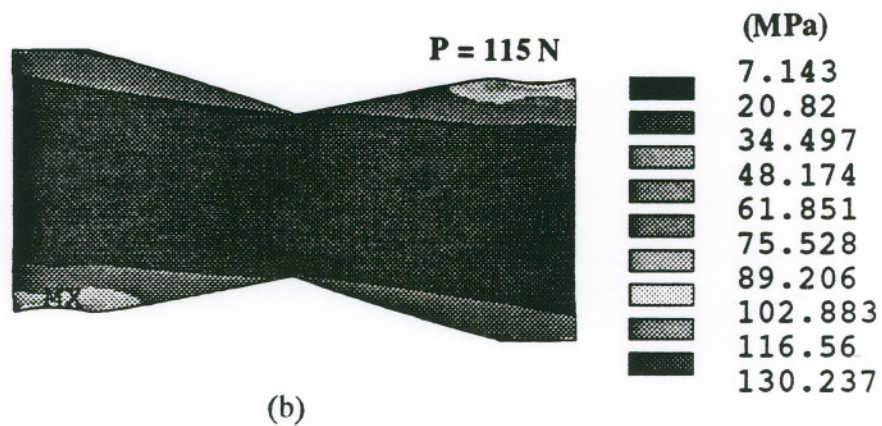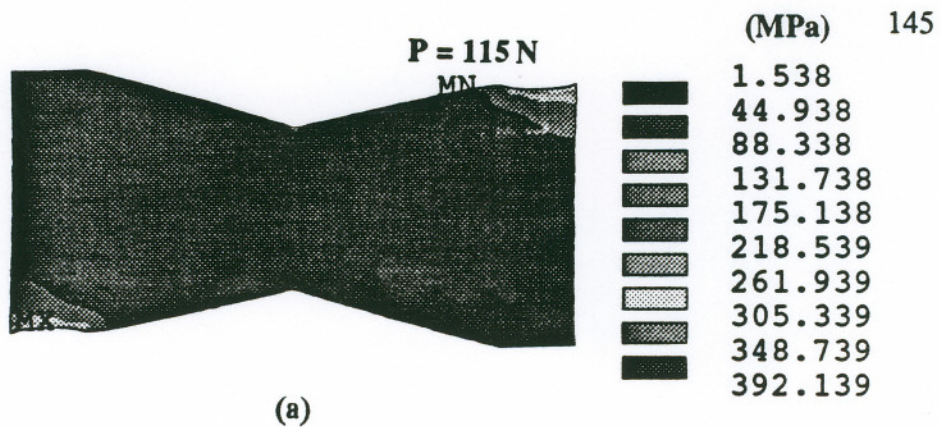
Figure B.4 von Mises stress contours for $\alpha = 150°$ and ER = 14.2 (A-type).
(a) $\phi = -30°$ (shear–tension); (b) $\phi = 0°$ (pure shear); and
(c) $\phi = +30°$ (shear-compression).
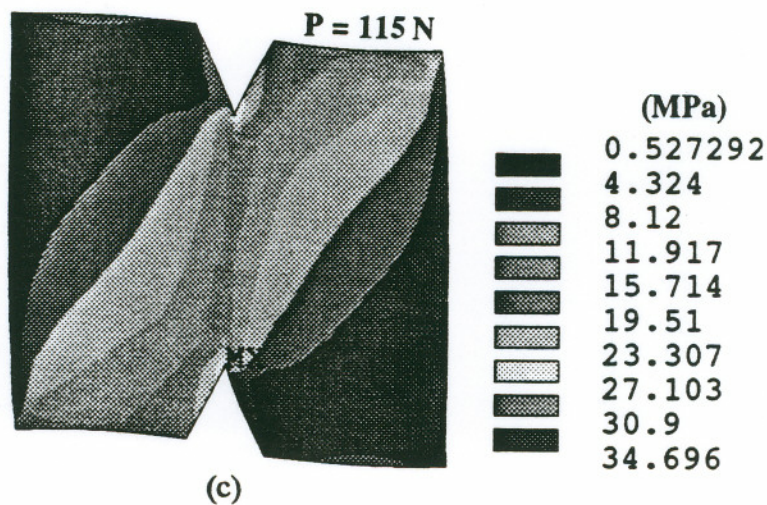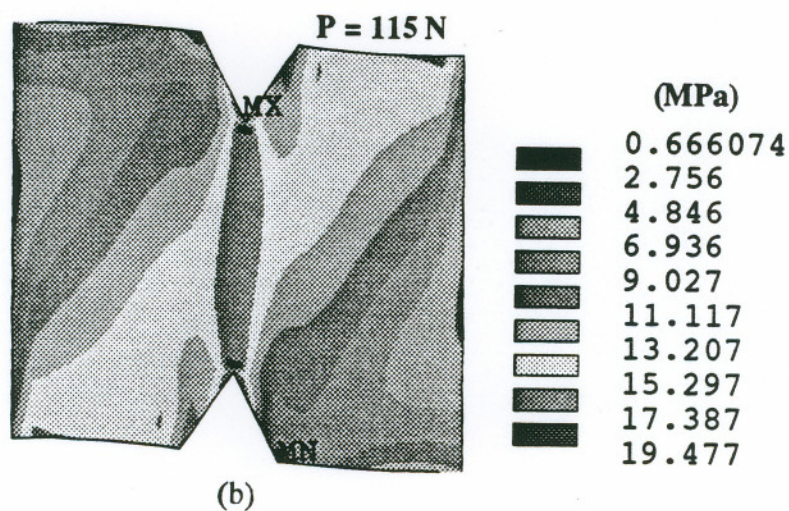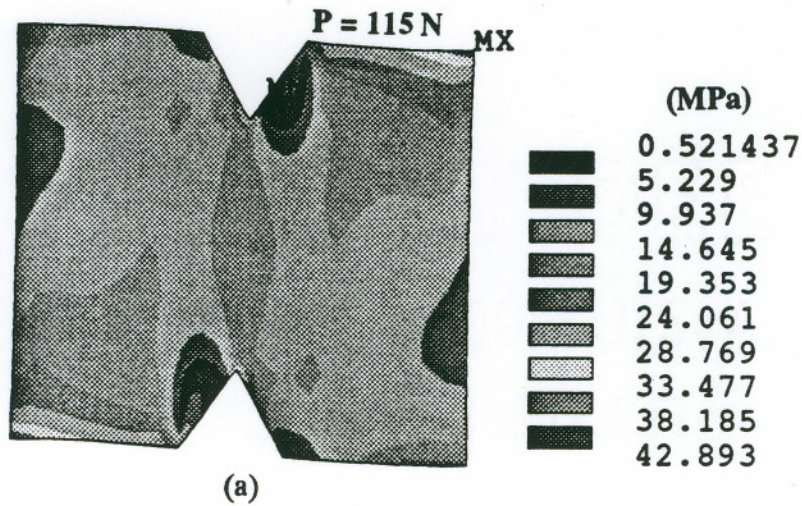
Figure B.5 von Mises stress contours for α = 60° and ER = 14.2 (B-type).
(a) φ = − 30° (shear−tension); (b) φ = 0° (pure shear); and
(c) φ = + 30° (shear-compression).

P = 115 N

(MPa)

0.243826
5.271
10.297
15.324
20.351
25.378
30.405
35.431
40.458
45.485

(a)

P = 115 N

(MPa)

1.289
3.086
4.884
6.682
8.48
10.277
12.075
13.873
15.67
17.468

(b)

P = 115 N

(MPa)

0.870604
3.922
6.974
10.026
13.078
16.129
19.181
22.233
25.284
28.336

(c)
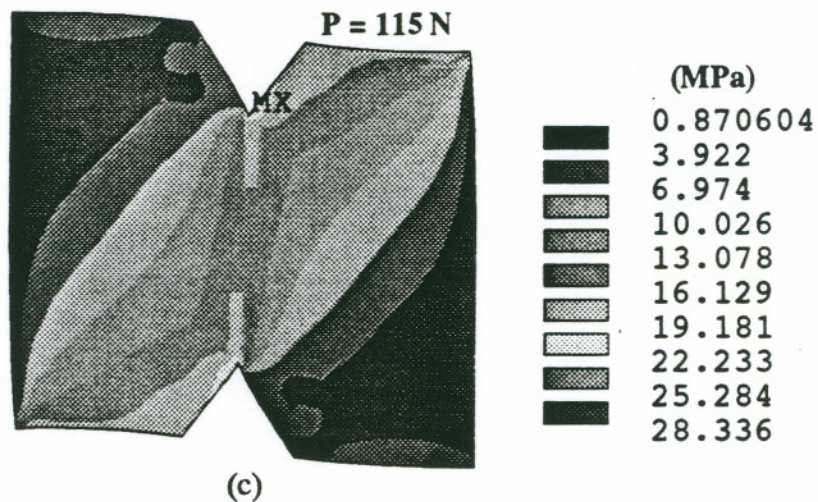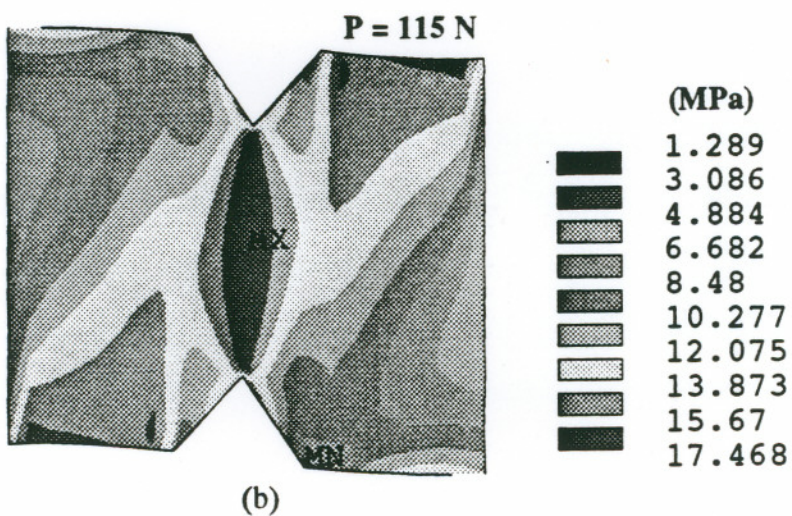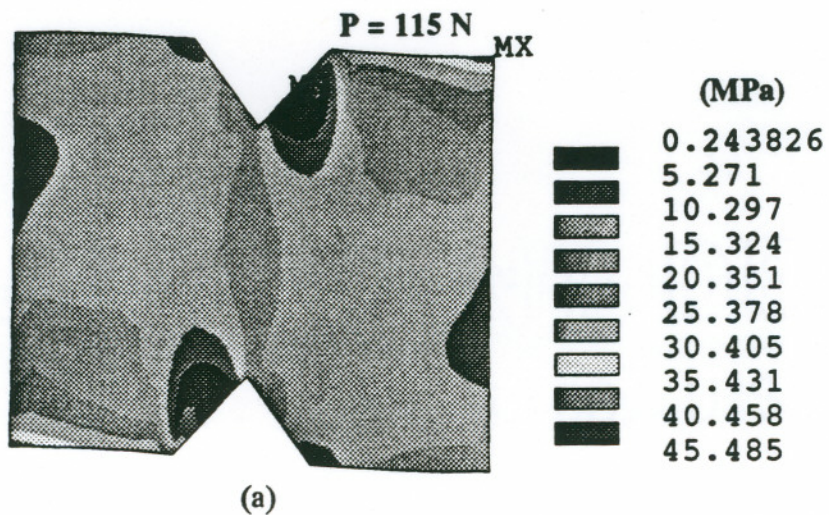
Figure B.6 von Mises stress contours for $\alpha = 75°$ and ER = 14.2 (B-type).
(a) $\phi = -30°$ (shear–tension); (b) $\phi = 0°$ (pure shear); and
(c) $\phi = +30°$ (shear-compression).

APPENDIX C

In this Appendix, the derivation of the energy release rates G, G_I and G_{II} in the Iosipescu specimen is outlined using beam theory analysis. [1] The analysis is applied for isotropic as well as unidirectional composite (orthotropic) Iosipescu specimens under combined shear and compression or tension loading conditions.

C.1. Analytical Solution

The beam solution proposed by Williams[1] for cracked laminates was applied to the Iosipescu specimen with skew-symmetric cracks. The crack configuration, along with the loading conditions and specimen dimensions are shown in Figures C.1a and C.1b. The moments M_1 and M_2 acting on the two arms of the right crack are firstly determined as a function of the crack length a and the loading angle ϕ. Then, on applying (2.25), (2.26), (2.28) and (2.27), the total energy release rate G, the opening component G_I, and the shear component G_{II} are respectively evaluated.

C.1.1. Moments M_1 and M_2

The moment M_1 is zero for all crack lengths and loading angles. Hence, only M_2, and thereafter dM_2/da need to be determined. P is the total compressive load, while P_1 and P_2 are the individual components for the inner and outer force-couples respectively. In the equations presented in this Appendix, the expressions for P_1 and P_2 in terms of P have been substituted from the results obtained in Appendix A.

The Iosipescu specimen with positive loading angle $(+\phi)$ is shown in Figure C.1a, while that with negative loading angle $(-\phi)$ is shown in Figure C.1b. As mentioned earlier, $M_1 = 0$; hence it follows that $dM_1/da = 0$ for all crack lengths a. There are three cases to be considered, [2] namely: $a \le c_1$, $c_1 < a \le c_2$ and $a > c_2$. The moment M_2 is evaluated separately for the three different cases.

(i) $a \le c_1$

In this case, the moment contribution will come from the loads on the left section $(P_1$ and $P_2)$ of the specimen. M_2 and dM_2/da can be expressed as:

$$M_2 = (P\cos\phi)a + \frac{P\cos\phi}{1-\frac{x}{y}}c - \frac{P\cos\phi}{\frac{y}{x}-1}l \tag{C.1}$$

$$- P\sin\phi \left[\frac{y+x}{y-x}\right]\left[\frac{h'}{2}\right] + P\sin\phi\left[\frac{w}{2}\right]$$

and

$$\frac{dM_2}{da} = P\cos\phi \tag{C.2}$$

(ii) $c_1 < a \le c_2$

In this case, the moment contribution will consist of two parts. The loads on the left section will contribute wholly; there will be partial contribution from the distributed load p_1 of the right section (the inner force-couple). M_2 and dM_2/da can be expressed as:

$$M_2 = (P\cos\phi)a + P\cos\phi\left[\frac{cy-lx}{y-x}\right] - P\sin\phi\left[\frac{y+x}{y-x}\right]\left[\frac{h'}{2}\right] \tag{C.3}$$

$$+ P\sin\phi \left[\frac{w}{2}\right] - \frac{P\cos\phi}{2\left\{1 - \frac{x}{y}\right\}} \frac{(a - c_1)^2}{c_2 - c_1} - \frac{P\sin\phi}{2\left\{1 - \frac{x}{y}\right\}} \frac{(a - c_1)(h' + w)}{c_2 - c_1}$$

and

$$\frac{dM_2}{da} = P\cos\phi - \frac{P\cos\phi}{1 - \frac{x}{y}} \frac{(a - c_1)}{c_2 - c_1} - \frac{P\sin\phi}{2\left\{1 - \frac{x}{y}\right\}} \frac{(h' + w)}{c_2 - c_1} \tag{C.4}$$

(iii) $a > c_2$

In this case, the moment contribution will come from the left section (P_1 and P_2) as well as from the inner force-couple on the right section (P_1). The distributed load p_1 of the right section acting over a length $c_2 - c_1$ will contribute wholly. M_2 and dM_2/da can be expressed as:

$$M_2 = (P\cos\phi)a + P\cos\phi \left[\frac{cy - lx}{y - x}\right] - P\sin\phi \left[\frac{y + x}{y - x}\right]\left[\frac{h'}{2}\right] \tag{C.5}$$

$$+ P\sin\phi \left[\frac{w}{2}\right] - \frac{P\cos\phi}{1 - \frac{x}{y}}(a - c) - \frac{P\sin\phi}{1 - \frac{x}{y}} \frac{(h' + w)}{2}$$

and

$$\frac{dM_2}{da} = \frac{-P\cos\phi}{\frac{y}{x} - 1} \tag{C.6}$$

where $x = 2c - h'\tan\phi$, and $y = 2l + h'\tan\phi$ in (C.1)–(C.6).

C.1.2. Calculation of G, G_I and G_{II}

From (2.25) in Section 2.4.3.1, the total energy release rate G can now be written as

$$G = \frac{3(1+v)}{5BEA} \frac{\xi}{(1-\xi)} \left[\frac{dM_2}{da}\right]^2 \tag{C.7}$$

From (2.26) in Section 2.4.3.2, G_I can now be expressed as

$$G_I = \frac{M_2^2}{BEI} \frac{1}{16(1+\beta)(1-\xi)^3} \tag{C.8}$$

From (2.27) in Section 2.4.3.2, G_{II} can now be written as

$$G_{II} = \frac{M_2^2}{BEI} \frac{3}{16} \frac{(1-\xi)}{(1+\beta)\xi^2} \tag{C.9}$$

where $E = E_{11}$ (orientation A) in (C.7)–(C.9), and in case of orthotropic materials, the shear modulus G_{12} should be used instead of $E/2(1+v)$ in (C.7).

By substituting the expressions derived for M_2 and dM_2/da from Section C.1.1 into (C.7)–(C.9), the energy release rates G, G_I and G_{II} can be computed.
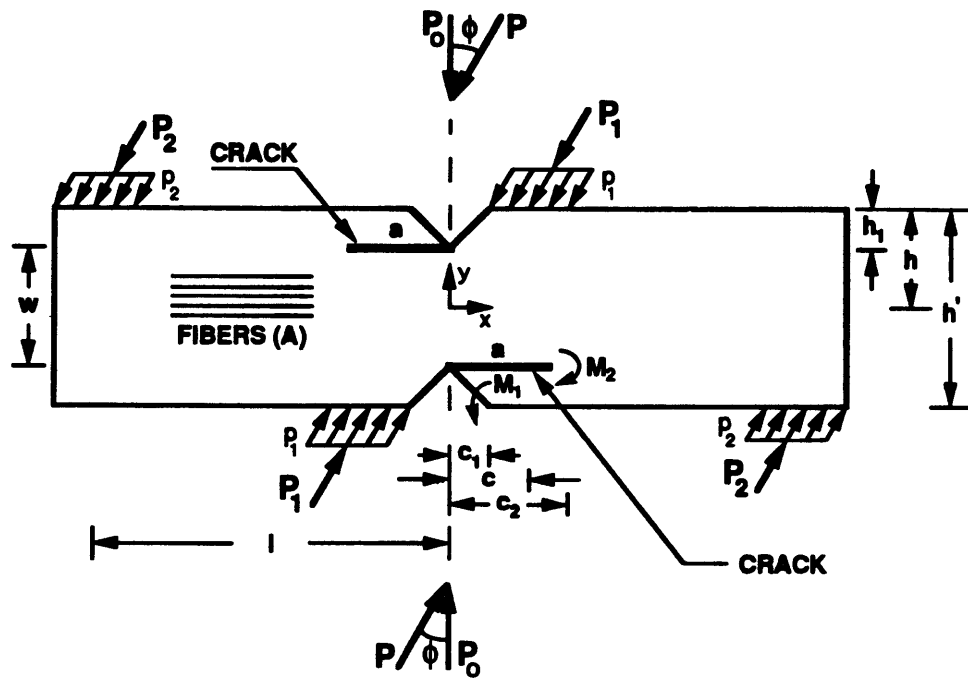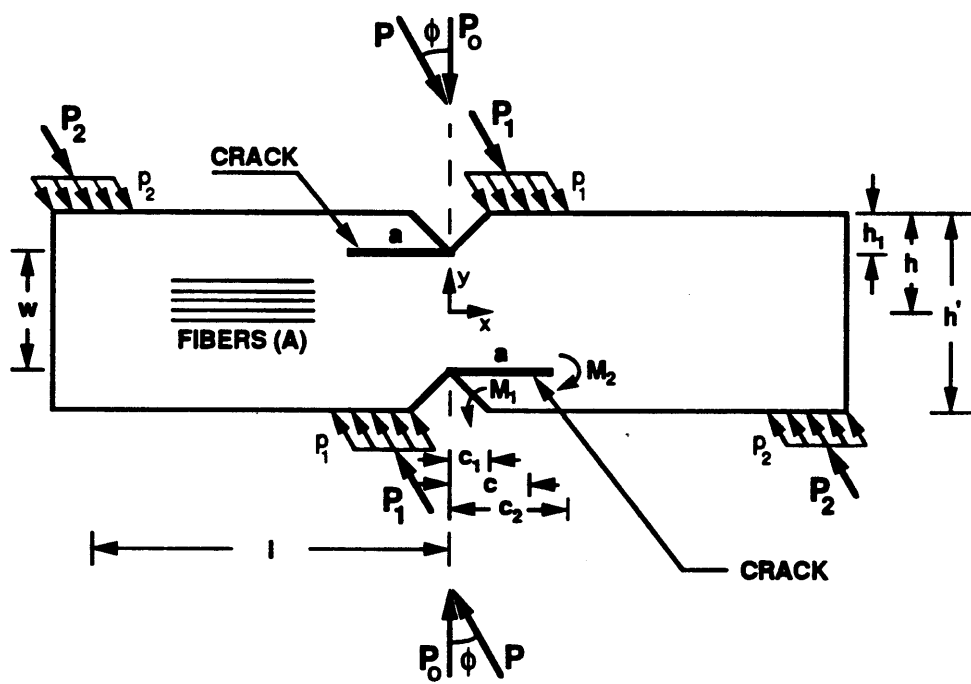
Figure C.1 Crack configuration in composite (A-type) Iosipescu specimen.
(a) anti-clockwise rotation ($+ \phi$); and (b) clockwise rotation ($- \phi$).

References

1. J. G. Williams, "Energy release rates for cracked laminates," *International Journal of Fracture*, vol. 36, pp. 101-119, 1988.

2. J. G. Williams, *Private communications with Dr. M. Kumosa, 1989.*

APPENDIX D

In this Appendix, the stress intensity factors in an orthotropic strip with a single edge-crack are numerically evaluated. The accuracy of the displacement method and VCC-schemes for orthotropic fracture analysis is evaluated by comparing the numerical values to the reference solution results provided by Kaya and Erdogan. [1]

D.1. Single Edge-Crack in an Orthotropic Strip under Tension

In Figure D.1, an orthotropic strip with an edge-crack under uniaxial tension is illustrated. The material properties[1] and specimen dimension are also indicated in Figure D.1. The finite element mesh (one-half) for $a/w = 0.4$ and $L = 0.1\,a$ is shown in Figure D.2. The finite element computations were carried out for $a/w = 0.1, 0.2, 0.3, \ldots, 0.8$.

The displacement method - equation (2.11), VCC-2C (two calculations), and the VCC-1C method (one calculation) were applied as outlined in Section 2.4.2. The analysis was carried out for three different crack-tip element sizes, namely, $L = 0.1\,mm$, $0.02\,mm$, and $0.01\,mm$, so as to evaluate the influence of the crack-tip element size on the stress intensity values. The results obtained for the aforementioned cases are presented in Tables D.1–D.3.

Table D.1. Stress intensity factors in an orthotropic strip with an edge crack under uniaxial tension $L = 0.1a$.

$\dfrac{a}{w}$	Ref. Soln.[†]	VCC-1C Method		VCC-2C Method		Displacement Method - Eqn. (2.11)	
	$\dfrac{K_I}{\sigma_0\sqrt{\pi a}}$	$\dfrac{K_I}{\sigma_0\sqrt{\pi a}}$	% Error	$\dfrac{K_I}{\sigma_0\sqrt{\pi a}}$	% Error	$\dfrac{K_I}{\sigma_0\sqrt{\pi a}}$	% Error
0.1	1.1284	1.1479	1.73	1.1534	2.22	1.1513	2.03
0.2	1.3172	1.3103	0.52	1.3166	0.05	1.3222	0.38
0.3	1.6069	1.5880	1.18	1.5959	0.68	1.6036	0.21
0.4	2.0421	2.0148	0.99	2.0250	0.84	2.0294	0.62
0.5	2.7199	2.6726	1.74	2.6865	1.23	2.6750	1.65
0.6	3.8590	3.7674	2.37	3.7879	1.84	3.7445	2.98
0.7	6.0350	5.8185	3.59	5.8508	3.05	5.6993	5.56
0.8	11.2740	10.5500	6.42	10.6120	5.87	10.1580	9.89

[†] A. C. Kaya and F. Erdogan [78]

Table D.2. Stress intensity factors in an orthotropic strip with an edge crack under uniaxial tension: L = 0.02 a.

$\dfrac{a}{w}$	Ref. Soln.[†] $\dfrac{K_I}{\sigma_0 \sqrt{\pi a}}$	VCC-1C Method $\dfrac{K_I}{\sigma_0 \sqrt{\pi a}}$	% Error	VCC-2C Method $\dfrac{K_I}{\sigma_0 \sqrt{\pi a}}$	% Error	Displacement Method - Eqn. (2.11) $\dfrac{K_I}{\sigma_0 \sqrt{\pi a}}$	% Error
0.1	1.1284	1.1083	1.78	1.1139	1.29	1.1160	1.10
0.2	1.3172	1.3090	0.62	1.3124	0.36	1.3140	0.24
0.3	1.6069	1.5972	0.60	1.6053	0.10	1.6029	0.25
0.4	2.0421	2.0285	0.67	2.0389	0.16	2.0345	0.37
0.5	2.7199	2.6999	0.74	2.7138	0.22	2.7007	0.71
0.6	3.8590	3.8212	0.98	3.8412	0.46	3.8194	1.03
0.7	6.0350	5.9565	1.30	5.9877	0.78	5.9329	1.69
0.8	11.2740	11.0290	2.17	11.0890	1.64	10.9070	3.26

[†] A. C. Kaya and F. Erdogan [78]

Table D.3. Stress intensity factors in an orthotropic strip with an edge crack
under uniaxial tension: $L = 0.01a$.

$\dfrac{a}{w}$	Ref. Soln.[†] $\dfrac{K_I}{\sigma_0\sqrt{\pi a}}$	VCC-1C Method $\dfrac{K_I}{\sigma_0\sqrt{\pi a}}$	% Error	VCC-2C Method $\dfrac{K_I}{\sigma_0\sqrt{\pi a}}$	% Error	Displacement Method - Eqn. (2.11) $\dfrac{K_I}{\sigma_0\sqrt{\pi a}}$	% Error
0.1	1.1284	1.1248	0.32	1.1277	0.06	1.1276	0.07
0.2	1.3172	1.3102	0.53	1.3135	0.28	1.3151	0.16
0.3	1.6069	1.5981	0.55	1.6022	0.29	1.6023	0.29
0.4	2.0421	2.0306	0.56	2.0410	0.05	2.0375	0.23
0.5	2.7199	2.7010	0.69	2.7149	0.18	2.7052	0.54
0.6	3.8590	3.8282	0.80	3.8479	0.29	3.8325	0.69
0.7	6.0350	5.9682	1.11	5.9991	0.60	5.9608	1.23
0.8	11.2740	11.0760	1.76	11.1350	1.23	11.0220	2.23

† A. C. Kaya and F. Erdogan [78]
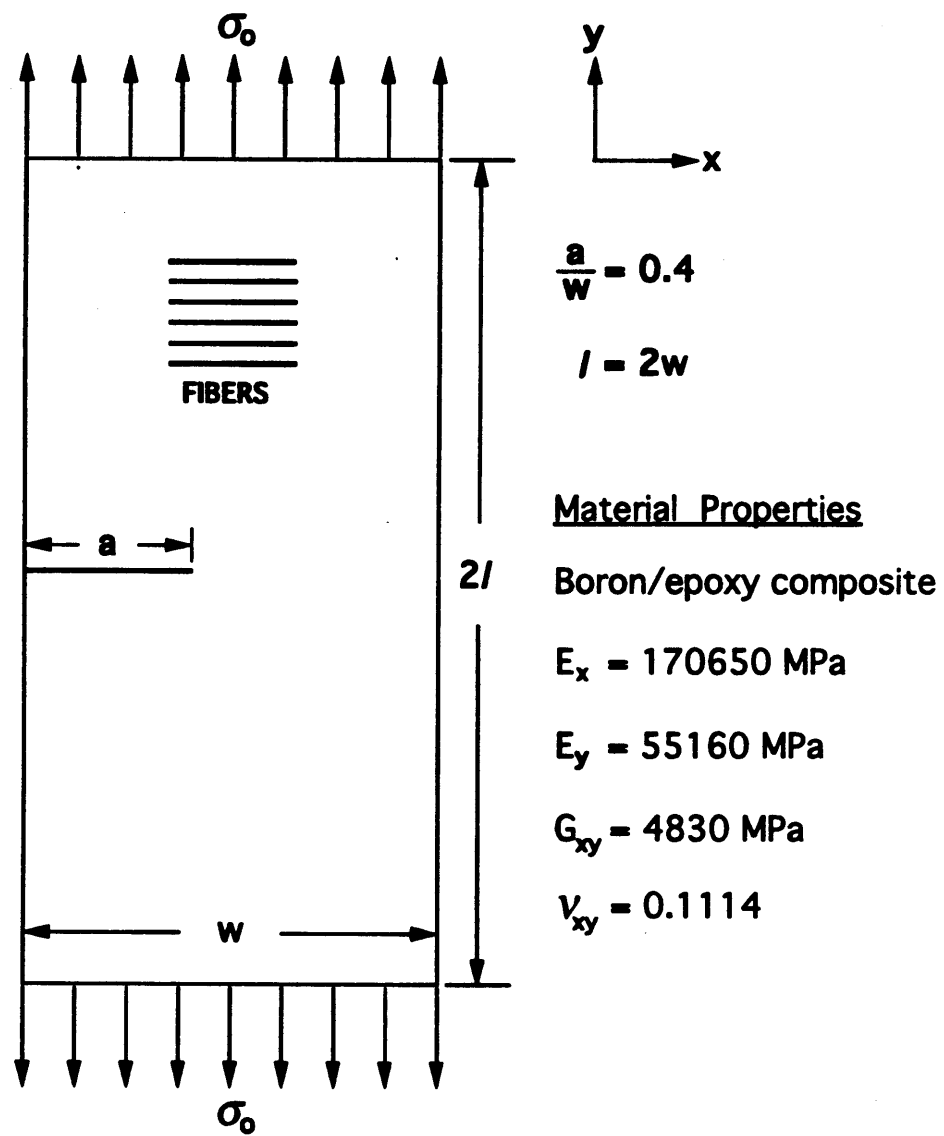
Figure D.1 Single edge-crack in an orthotropic strip under tension.
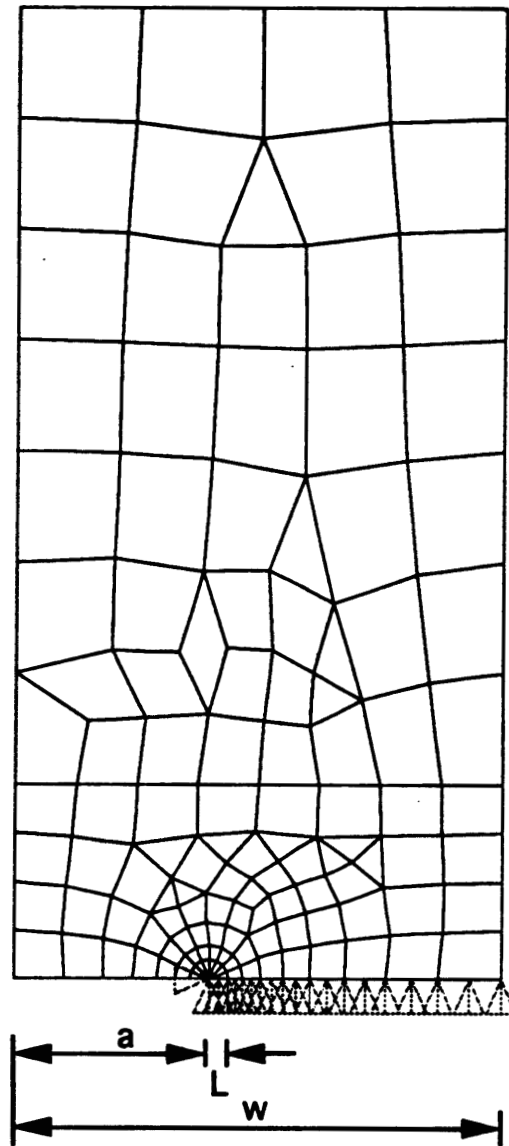
Figure D.2 Finite element mesh (one-half): a/w = 0.4, L = 0.1*a*.

References

1. A. C. Kaya and F. Erdogan, "Stress intensity factors and COD in an orthotropic strip," *International Journal of Fracture*, vol. 16, no. 2, pp. 171-190, April 1980.

APPENDIX E

Table E.1. Mode partitions G_I and G_{II} in isotropic Iosipescu specimens.

ϕ (deg.)	a (mm)	Displacement extrapolation		VCC-1C scheme		VCC-2C scheme		Beam solution	
		G_I (kJ/m^2)	G_{II} (kJ/m^2)	G_I (kJ/m^2)	G_{II} (kJ/m^2)	G_I (kJ/m^2)	G_{II} (kJ/m^2)	G_I (kJ/m^2)	G_{II} (kJ/m^2)
	0	0.000	0.000	0.000	0.000	0.000	0.000	0.113	3.462
	1	8.427	3.770	8.515	3.869	8.639	3.927	0.018	2.404
	4	13.035	8.560	13.170	8.792	13.346	8.960	0.013	0.385
-45	7	17.236	14.802	17.419	15.208	17.570	15.432	1.091	33.523
	10	16.039	16.858	16.212	17.325	16.203	17.457	3.986	122.461
	13	14.041	17.548	14.193	18.037	14.122	18.030	5.720	175.726
	0	0.000	0.000	0.000	0.000	0.000	0.000	0.056	1.731
	1	6.851	2.591	6.923	2.658	7.023	2.701	0.029	0.876
	4	9.875	6.518	9.977	6.695	10.104	6.824	0.001	0.041
-30	7	11.341	9.895	11.461	10.167	11.562	10.319	0.369	11.339
	10	10.263	10.857	10.373	11.157	10.387	11.256	1.075	33.019
	13	8.392	10.358	8.483	10.646	8.456	10.654	1.406	43.272
	0	0.000	0.000	0.000	0.000	0.000	0.000	0.015	0.464
	1	5.633	1.762	5.692	1.807	5.776	1.838	0.002	0.066
	4	7.877	4.955	7.960	5.088	8.055	5.189	0.033	1.027
-15	7	8.306	7.187	8.393	7.385	8.462	7.494	0.281	8.618
	10	7.204	7.648	7.281	7.860	7.290	7.929	0.562	17.278
	13	5.602	6.931	5.663	7.124	5.647	7.130	0.625	19.196

APPENDIX E

Table E.1. Mode partitions G_I and G_{II} in isotropic Iosipescu specimens.

ϕ (deg.)	a (mm)	Displacement extrapolation		VCC-1C scheme		VCC-2C scheme		Beam solution	
		G_I (kJ/m^2)	G_{II} (kJ/m^2)	G_I (kJ/m^2)	G_{II} (kJ/m^2)	G_I (kJ/m^2)	G_{II} (kJ/m^2)	G_I (kJ/m^2)	G_{II} (kJ/m^2)
	0	0.000	0.000	0.000	0.000	0.000	0.000	0.113	3.462
	1	8.427	3.770	8.515	3.869	8.639	3.927	0.018	2.404
	4	13.035	8.560	13.170	8.792	13.346	8.960	0.013	0.385
-45	7	17.236	14.802	17.419	15.208	17.570	15.432	1.091	33.523
	10	16.039	16.858	16.212	17.325	16.203	17.457	3.986	122.461
	13	14.041	17.548	14.193	18.037	14.122	18.030	5.720	175.726
	0	0.000	0.000	0.000	0.000	0.000	0.000	0.056	1.731
	1	6.851	2.591	6.923	2.658	7.023	2.701	0.029	0.876
	4	9.875	6.518	9.977	6.695	10.104	6.824	0.001	0.041
-30	7	11.341	9.895	11.461	10.167	11.562	10.319	0.369	11.339
	10	10.263	10.857	10.373	11.157	10.387	11.256	1.075	33.019
	13	8.392	10.358	8.483	10.646	8.456	10.654	1.406	43.272
	0	0.000	0.000	0.000	0.000	0.000	0.000	0.015	0.464
	1	5.633	1.762	5.692	1.807	5.776	1.838	0.002	0.066
	4	7.877	4.955	7.960	5.088	8.055	5.189	0.033	1.027
-15	7	8.306	7.187	8.393	7.385	8.462	7.494	0.281	8.618
	10	7.204	7.648	7.281	7.860	7.290	7.929	0.562	17.278
	13	5.602	6.931	5.663	7.124	5.647	7.130	0.625	19.196

	0	0.000	0.000	0.000	0.000	0.000	0.000	0.000	0.000
	1	4.078	0.985	4.120	1.009	4.183	1.028	0.006	0.192
	4	5.576	3.235	5.634	3.323	5.697	3.390	0.100	3.077
0	7	5.420	4.593	5.477	4.719	5.515	4.787	0.247	7.577
	10	4.436	4.727	4.484	4.858	4.484	4.897	0.316	9.714
	13	3.264	4.084	3.300	4.197	3.289	4.199	0.270	8.305
	0	0.000	0.000	0.000	0.000	0.000	0.000	0.015	0.464
	1	2.409	0.369	2.433	0.377	2.472	0.386	0.040	1.220
	4	3.216	1.621	3.250	1.664	3.282	1.700	0.184	5.642
15	7	2.810	2.283	2.840	2.346	2.853	2.378	0.217	6.658
	10	2.088	2.235	2.110	2.297	2.104	2.311	0.162	4.984
	13	1.408	1.809	1.423	1.859	1.417	1.858	0.086	2.645
	0	0.000	0.000	0.000	0.000	0.000	0.000	0.056	1.731
	1	0.990	0.037	0.999	0.038	1.017	0.039	0.094	2.874
	4	1.273	0.458	1.286	0.470	1.296	0.481	0.262	8.036
30	7	0.903	0.657	0.913	0.675	0.913	0.683	0.181	5.564
	10	0.526	0.570	0.532	0.585	0.525	0.586	0.067	2.049
	13	0.279	0.393	0.282	0.404	0.279	0.402	0.010	0.293

Table E.2. Mixed mode energy release rate G ($G_I + G_{II}$) in isotropic Iosipescu specimens.

ϕ (deg.)	a (mm)	Displacement extrapolation G (kJ/m^2)	J-integral J (kJ/m^2)	VCC-1C scheme G (kJ/m^2)	VCC-2C scheme G (kJ/m^2)	Beam solution G (kJ/m^2)
-45	0	0.000	0.000	0.000	0.000	3.575
	1	12.196	12.104	12.384	12.565	2.422
	4	21.595	21.609	21.962	22.306	0.398
	7	32.038	32.227	32.627	33.020	34.614
	10	32.897	33.216	33.536	33.660	126.447
	13	31.588	31.995	32.230	32.152	181.446
-30	0	0.000	0.000	0.000	0.000	1.787
	1	9.442	9.348	9.581	9.723	0.905
	4	16.393	16.406	16.671	16.928	0.042
	7	21.236	21.367	21.628	21.881	11.708
	10	21.120	21.327	21.530	21.644	34.094
	13	18.750	18.988	19.129	19.110	44.678
-15	0	0.000	0.000	0.000	0.000	0.479
	1	7.395	7.304	7.499	7.613	0.068
	4	12.832	12.930	13.048	13.244	1.060
	7	15.493	15.591	15.778	15.956	8.899
	10	14.852	14.999	15.141	15.219	17.840
	13	12.534	12.693	12.787	12.777	19.821

0	0	0.000	0.000	0.000	0.000	0.000
	1	5.063	4.987	5.129	5.211	0.198
	4	8.811	8.797	8.957	9.087	3.177
	7	10.012	10.079	10.196	10.302	7.824
	10	9.163	9.254	9.342	9.381	10.030
	13	7.348	7.443	7.497	7.488	8.575
	0	0.000	0.000	0.000	0.000	0.479
	1	2.777	2.725	2.810	2.858	1.262
	4	4.837	4.817	4.914	4.981	5.826
15	7	5.093	5.117	5.186	5.231	6.875
	10	4.323	4.366	4.407	4.415	5.146
	13	3.217	3.260	3.283	3.275	2.731
	0	0.000	0.000	0.000	0.000	1.787
	1	1.027	1.004	1.037	1.056	2.968
	4	1.731	1.715	1.757	1.777	8.298
30	7	1.561	1.565	1.588	1.596	5.745
	10	1.095	1.106	1.117	1.111	2.116
	13	0.672	0.682	0.686	0.681	0.303

Table E.3.   Energy release rates G_I, G_{II}, and G in orthotropic (A-type) Iosipescu specimens.

ϕ	a	VCC-1C scheme			VCC-2C scheme			Beam solution		
		G_I	G_{II}	G	G_I	G_{II}	G	G_I	G_{II}	G
(deg.)	(mm)	(kJ/m^2)	(kJ/m^2)	(kJ/m^2)	(kJ/m^2)	(kJ/m^2)	(kJ/m^2)	(kJ/m^2)	(kJ/m^2)	(kJ/m^2)
	0	0.000	0.000	0.000	0.000	0.000	0.000	0.003	0.090	0.093
	1	0.997	0.252	1.249	1.009	0.256	1.265	0.002	0.063	0.065
	4	0.770	0.318	1.088	0.772	0.324	1.096	0.000	0.010	0.010
-45	7	0.525	0.378	0.902	0.520	0.381	0.901	0.029	0.875	0.904
	10	0.232	0.301	0.533	0.224	0.301	0.524	0.104	3.197	3.301
	13	0.096	0.255	0.351	0.093	0.253	0.346	0.149	4.588	4.737
	0	0.000	0.000	0.000	0.000	0.000	0.000	0.002	0.045	0.047
	1	1.064	0.188	1.252	1.076	0.191	1.268	0.000	0.023	0.023
	4	0.885	0.322	1.207	0.889	0.329	1.218	0.000	0.001	0.001
-30	7	0.601	0.373	0.973	0.599	0.378	0.977	0.010	0.296	0.306
	10	0.331	0.315	0.646	0.325	0.318	0.643	0.028	0.862	0.890
	13	0.166	0.250	0.416	0.164	0.250	0.414	0.037	1.130	1.666
	0	0.000	0.000	0.000	0.000	0.000	0.000	0.000	0.012	0.012
	1	1.063	0.138	1.202	1.076	0.141	1.217	0.000	0.002	0.002
	4	0.886	0.284	1.170	0.890	0.290	1.180	0.001	0.027	0.028
-15	7	0.581	0.330	0.911	0.580	0.334	0.914	0.007	0.225	0.232
	10	0.325	0.281	0.606	0.321	0.284	0.605	0.015	0.451	0.466
	13	0.164	0.216	0.380	0.162	0.216	0.378	0.016	0.501	0.517

	0	0.000	0.000	0.000	0.000	0.000	0.000	0.000	0.000	0.000
	1	0.940	0.086	1.026	0.952	0.088	1.040	0.000	0.005	0.005
	4	0.771	0.213	0.984	0.774	0.218	0.993	0.003	0.080	0.083
0	7	0.483	0.251	0.734	0.482	0.255	0.736	0.006	0.198	0.204
	10	0.262	0.213	0.475	0.258	0.216	0.474	0.008	0.254	0.262
	13	0.127	0.159	0.286	0.125	0.159	0.284	0.007	0.217	0.224
	0	0.000	0.000	0.000	0.000	0.000	0.000	0.000	0.012	0.012
	1	0.716	0.040	0.755	0.725	0.041	0.765	0.001	0.032	0.033
	4	0.571	0.129	0.699	0.573	0.132	0.705	0.005	0.147	0.152
15	7	0.335	0.156	0.491	0.334	0.158	0.492	0.006	0.174	0.180
	10	0.169	0.130	0.299	0.166	0.132	0.298	0.004	0.130	0.134
	13	0.075	0.093	0.169	0.074	0.093	0.168	0.002	0.069	0.071
	0	0.000	0.000	0.000	0.000	0.000	0.000	0.002	0.045	0.047
	1	0.446	0.009	0.454	0.451	0.009	0.460	0.002	0.076	0.078
	4	0.338	0.054	0.392	0.339	0.055	0.394	0.007	0.210	0.217
30	7	0.179	0.069	0.247	0.177	0.070	0.247	0.005	0.145	0.150
	10	0.077	0.055	0.132	0.075	0.056	0.131	0.002	0.053	0.055
	13	0.028	0.037	0.065	0.027	0.037	0.064	0.000	0.008	0.008

Table E.4. Energy release rates (G_I, G_{II}, and G) in orthotropic (A-type) Iosipescu specimens by the displacement extrapolation method.

		Displacement extrapolation[†] − linear regression analysis								
ϕ	a	G_I^U	G_I^L	$G_I^{avg.}$	G_{II}^U	G_{II}^L	$G_{II}^{avg.}$	G^U	G^L	$G^{avg.}$
(deg.)	(mm)	(kJ/m^2)	(kJ/m^2)	(kJ/m^2)	(kJ/m^2)	(kJ/m^2)	(kJ/m^2)	(kJ/m^2)	(kJ/m^2)	(kJ/m^2)
	0	0.000	0.000	0.000	0.000	0.000	0.000	0.000	0.000	0.000
	1	1.207	0.644	0.926	0.254	0.178	0.216	1.461	0.822	1.152
	4	0.884	0.548	0.716	0.310	0.233	0.271	1.194	0.780	0.987
-45	7	0.565	0.403	0.484	0.369	0.275	0.322	0.933	0.679	0.806
	10	0.225	0.200	0.213	0.300	0.214	0.257	0.525	0.413	0.470
	13	0.076	0.100	0.088	0.256	0.179	0.217	0.332	0.279	0.305
	0	0.000	0.000	0.000	0.000	0.000	0.000	0.000	0.000	0.000
	1	1.242	0.720	0.981	0.190	0.139	0.164	1.432	0.859	1.145
	4	0.957	0.679	0.818	0.309	0.240	0.275	1.267	0.919	1.093
-30	7	0.609	0.495	0.552	0.358	0.277	0.318	0.967	0.772	0.870
	10	0.303	0.303	0.303	0.308	0.230	0.269	0.611	0.533	0.572
	13	0.131	0.175	0.153	0.246	0.180	0.213	0.377	0.356	0.366
	0	0.000	0.000	0.000	0.000	0.000	0.000	0.000	0.000	0.000
	1	1.253	0.710	0.981	0.135	0.106	0.121	1.388	0.816	1.103
	4	0.950	0.685	0.817	0.271	0.213	0.242	1.221	0.898	1.059
-15	7	0.582	0.485	0.533	0.316	0.246	0.281	0.897	0.732	0.814
	10	0.293	0.302	0.298	0.273	0.207	0.240	0.566	0.509	0.538
	13	0.127	0.175	0.151	0.211	0.158	0.185	0.338	0.333	0.336

	0	0.000	0.000	0.000	0.000	0.000	0.000	0.000	0.000	0.000
	1	1.130	0.610	0.871	0.083	0.069	0.076	1.213	0.679	0.947
	4	0.830	0.594	0.712	0.203	0.161	0.182	1.033	0.754	0.894
0	7	0.483	0.404	0.443	0.240	0.188	0.214	0.723	0.592	0.657
	10	0.234	0.245	0.240	0.207	0.157	0.182	0.441	0.402	0.422
	13	0.096	0.138	0.117	0.155	0.116	0.135	0.251	0.253	0.253
	0	0.000	0.000	0.000	0.000	0.000	0.000	0.000	0.000	0.000
	1	0.886	0.445	0.666	0.037	0.034	0.036	0.923	0.479	0.701
	4	0.621	0.433	0.527	0.122	0.098	0.110	0.743	0.531	0.637
15	7	0.337	0.279	0.308	0.142	0.117	0.129	0.479	0.396	0.437
	10	0.150	0.159	0.155	0.127	0.096	0.111	0.277	0.255	0.266
	13	0.018	0.084	0.051	0.091	0.068	0.079	0.109	0.152	0.130
	0	0.000	0.000	0.000	0.000	0.000	0.000	0.000	0.000	0.000
	1	0.578	0.258	0.418	0.007	0.010	0.008	0.585	0.268	0.426
	4	0.376	0.250	0.313	0.051	0.041	0.046	0.427	0.291	0.359
30	7	0.182	0.147	0.164	0.066	0.052	0.059	0.248	0.198	0.223
	10	0.011	0.073	0.042	0.054	0.040	0.047	0.065	0.114	0.089
	13	0.019	0.033	0.026	0.036	0.027	0.032	0.055	0.060	0.058

† Superscripts U and L refer to values computed from a linear regression along the upper and lower crack faces respectively (see Figure 3.35a).

APPENDIX F

F.1. Computational Platform and Execution Time

In this study, the numerical investigations were carried out on an IBM RISC System/6000 workstation (AIX 3.1.5 Operating System). The particular RISC/6000 system was a POWERstation/POWERserver 320 (model 7012), with a clock speed of 20.0 MHz, 29.5 MIPS, 8.5 MFL, and 24.6 SPC. The hardware configuration was: 640 MB of internal memory and 2.4 GB of external memory, with 16 MB of RAM.

The execution time (real-time) in single-user mode for the finite element analysis (solution phase) of Iosipescu specimens with notch angle $\alpha = 90^\circ$ was computed. The finite element analysis of an uncracked Iosipescu specimen (Figure 3.3) required 110 seconds for execution. The mesh illustrated in Figure 3.3 consists of 1964 isoparametric elements and 5281 node, with 10558 active degrees of freedom. The maximum wavefront was 160, while the R.M.S. wavefront was 116.5. In case of cracked specimens with two 10mm axial splits (Figure 3.33), the execution time was 115 seconds. The finite element mesh shown in Figure 3.33 consists of 1426 isoparametric elements and 1426 nodes, with 8674 active degrees of freedom. The maximum wavefront was 218, while the R.M.S. wavefront was 139.8.

In the evaluation of the dominant stress singularity at sharp notches by the Finite Element Iterative Method, the computation time was a function of the number of iterations for convergence, as well as on the type of loading. The average execution time per iteration for notch angle $\alpha = 90^\circ$ was computed. In case of mode I or mode II analysis, 82 seconds per iteration was needed for the mesh illustrated in Figure 3.25a. The mesh

presented in Figure 3.25a has 126 isoparametric elements and 407 nodes. The number of active degrees of freedom was 748, and the R.M.S. wavefront was 49.9. In a mixed mode analysis, 171 seconds per iteration was required for the mesh shown in Figure 3.35b; the mesh consists of 252 isoparametric elements and 785 nodes, with 79.0 active degrees of freedom. The R.M.S. wavefront in this case was 79.0.

BIOGRAPHICAL NOTE

The author was born on 17th November, 1965, in Madras, India. He received his Bachelor of Technology degree in Metallurgical Engineering from the Indian Institute of Technology, Bombay, India, in 1989. After completing his undergraduate studies, he worked for a year at Tata Steel, Jamshedpur, India, before deciding to pursue graduate studies in the U.S.

In September 1990, the author joined the graduate program at Oregon Graduate Institute (OGI). He completed all the requirements for a Master's degree at OGI in October 1992. During the course of his study at OGI, he has published the following technical papers:

[1] N. Sukumar, M. Kumosa, Application of the Finite Element Iterative Method to Cracks and Sharp Notches in Orthotropic Media, International Journal of Fracture, 1992, in press.

[2] N. Sukumar, M. Kumosa, Stress Singularities at Sharp Notches: Interpolation Formulas, International Journal of Fracture, August 1992, submitted.

[3] N. Sukumar, M. Kumosa, Finite Element Analysis of Axial Splits in Composite Iosipescu Specimens, International Journal of Fracture, September 1992, submitted.